Spatial and Temporal Multiscale Modelling Strategies for the Elastodynamic Response of Periodic Composites

İrem Yağmuroğlu

Department of Civil and Structural Engineering
The University of Sheffield

This thesis submitted in partial fulfilment for the degree of
Doctor of Philosophy

March 2023

"No man can visualize four dimensions, except mathematically. I think in four dimensions, but only abstractly."

Albert Einstein
The Saturday Evening Post, 1929

Declaration

All work presented within this thesis is my own work, except where specific reference has been made to the work of others.

İrem Yağmuroğlu
March 2023

Acknowledgements

I would like to begin by expressing my deepest gratitude to my supervisors, Professor Harm Askes and Dr. Zuhal Ozdemir, for their unwavering support, invaluable guidance, encouragement and inspiration they have provided throughout my PhD. Harm, I consider myself truly fortunate to have had the opportunity to work with someone as knowledgeable and passionate about our field as you, and to have grown under your mentorship. Your guidance and mentorship have not only honed my research skills, but have also been instrumental in shaping my teaching approach. Zuhal, your selflessness and willingness to assist me during the challenges and obstacles has been invaluable to me.

I am immensely grateful to the Ministry of Education in Turkey for providing me with the funding that made it possible for me to undertake this research.

I would also like to thank the MEE team! A big thank you to Dr. Matteo Di Benedetti whose guidance and support has been priceless in shaping my teaching philosophy, refining my approach to education, and instilling in me a deep passion for teaching. I would like to express my gratitude to all the friends I have made during my time at the MEE labs. I am truly grateful to have had the pleasure of meeting each and every one of you and for the endless laughter, fun moments, and positive energy you've brought into my life.

I would like to express my sincere appreciation to all the members of the UoS Department of Civil and Structural Engineering, who have been an essential part of my academic journey. Our fun moments, chit-chats, coffee breaks, and sport talks have truly has positively influenced my work. Not only have they provided much-needed breaks during busy days, but they have also brought so much joy and laughter into my life. Thanks to Dr. Ismail Abuzayed, I was fortunate to have had him as a companion during our PhD journey, sharing countless laughs, continuing our tradition of enjoying ice cream after our uphill battles in PhD meetings, and going on an eventful trip to Italy together.

I would also like to extend my gratitude to my friends in Türkiye and Ireland, who have shown me that distance is no barrier to true friendship. I am deeply grateful to my close friend, Sena Koçak, for being an amazing source of support and companionship for the past 13 years. Seda Kutlu and Elif İrem Mahmutoğlu have also been incredible friends who have shared beautiful memories and experiences with me. I am looking forward to many more adventures together. Thank you all for being a part of my life.

Lastly, but certainly not least, Mum and Dad, thank you for everything. Your love, guidance, and support have been the bedrock of my success, and I cannot thank you enough for being there for me through thick and thin. Your constant encouragement and belief in me have been the driving force behind my achievements, and I am proud to say that I owe all of my success to the two of you. Dad, thank you for helping me with my homesickness by creating fun moments that made me laugh every single time. Mum, thank you for being not only my mum, but also my friend, my confidante, and my inspiration. Once again, thank you for being the best parents anyone could ever ask for.

Abstract

The distinctive multiscale properties of composite materials render them increasingly popular in engineering applications for exploiting customizable characteristics to achieve superior material properties. This thesis aims to address challenges in modelling their microstructural features under dynamic excitations, using widely adopted multiscale methods to predict their mechanical behaviour. This thesis introduces novel techniques to address three prominent challenges: achieving accurate micro-macro averaging, attaining effective scale transitions, and selecting appropriate scale parameters in dynamics.

In order to improve the accuracy of micro-macro averaging, a method where the standard Hill-Mandel Principle is extended with time averaging is developed to obtain homogenised material properties from a transient dynamic numerical model when subjected to transient dynamic loads. Thus, in addition to a Representative Volume Element (RVE) to carry out the averaging in space, a sufficiently large time window is required to carry out the time averaging. The proposed space-time averaging approach is used to predict the dynamic RVE size by increasing static RVE sizes as well as time averaging windows, thereby capturing dynamic microstructural effects in the homogenized macroscopic response.

A further concern addressed in this thesis is to enhance the accuracy of dynamic scale transitions in computational homogenisation. By decoupling microstructures from its associated macrostructure in both space and time, a novel scale transition approach is presented to incorporate the simultaneous separation of length and time scales. This technique exploits the benefits of separations of length and time scales by increasing the RVE size as well as the time period on the microscale, ultimately leading to more accurate macroscopic response of a material.

The approach to increasing the RVE size for transient dynamic problems allows better understanding of material scale parameters in analytical homogenisation. The issue of quantifying length scale parameters in dynamics is addressed in this work in a gradient elasticity framework. A procedure is presented to select the dynamic length scale parameter linked to the dynamic RVE size through curve fitting optimisation. This provides a suitable value for the dynamic length scale parameter, which ensures an accurate material response without having deviations caused by the RVE size.

The efficacy and efficiency of the proposed methods in addressing the challenges are demonstrated through several numerical examples on a one-dimensional periodic laminate bar under various boundary conditions, material contrasts, and loading scenarios.

Table of contents

List of figures **x**

List of tables **xiii**

Nomenclature **xiv**

1 Introduction **1**
1.1 Background and Motivation 1
1.2 Scope and objectives of thesis 3
1.3 Thesis outline 4

2 Literature Review **6**
2.1 Introduction 6
2.2 Composite materials 6
2.3 Multiscale methods 9
2.4 Homogenisation methods 11
2.4.1 Analytical homogenisation 12
2.4.2 Numerical homogenisation 14
2.4.3 Computational homogenisation 15
2.5 Gradient elasticity theories 18
2.6 Commentary 21

3 Spatial and Temporal Averaging in Homogenisation **22**
3.1 Introduction 23
3.2 Space averaging 25
3.3 Time averaging 27
3.4 Numerical results 28
3.4.1 Effect of boundary conditions 30
3.4.2 Effect of time-averaging 30
3.4.3 Effect of number of unit cells and number of wave propagations 31
3.4.4 Material parameter studies 34

3.5 Discussion . . . 35

4 Spatial and Temporal Transitions in Computational Homogenisation 36
4.1 Introduction . . . 37
4.2 Dynamic computational homogenisation system . . . 38
4.3 Scale separation . . . 39
4.3.1 Separation of length scales . . . 40
4.3.2 Separation of time scales . . . 42
4.4 Macroscopic boundary value problem . . . 43
4.5 Microscopic boundary value problem . . . 45
4.6 Kinematics of the scale transitions . . . 45
4.6.1 Downscaling . . . 46
4.6.2 Upscaling . . . 46
4.7 Numerical model implementation . . . 47
4.7.1 Macroscopic equation of motion in linear problem . . . 47
4.7.2 Microscopic equation of motion in linear problem . . . 48
4.7.3 Computational homogenisation solution algorithm . . . 50
4.8 Numerical results . . . 51
4.8.1 The effect of N_{uc} . . . 53
4.8.2 The effect of N_{wp} . . . 55
4.8.3 The combination of N_{uc} and N_{wp} . . . 56
4.8.4 Different impedance contrasts . . . 56
4.8.5 Explicit time integration on micro level . . . 58
4.9 Discussion . . . 60

5 Dynamic Gradient Elasticity Length Scales 61
5.1 Introduction . . . 62
5.2 Gradient elasticity model in dynamics . . . 64
5.2.1 Formulation of the gradient elasticity model . . . 64
5.3 Wave dispersion . . . 67
5.4 Gradient length scale parameters . . . 68
5.5 Numerical model implementation . . . 72
5.6 Numerical results . . . 74
5.6.1 Effect of ℓ_d on dispersion behaviour . . . 74
5.6.2 Effect of various impedance contrasts on ℓ_{d} . . . 75
5.6.3 Comparison of $\ell_{\mathrm{d}}/\ell_{\mathrm{s}}$ with different methods . . . 77
5.7 Discussion . . . 78

6 Conclusions and future perspectives **80**
6.1 Conclusions 80
6.2 Future perspectives 82

References **84**

Appendix A Numerical Methods **92**

Appendix B Numerical and physical parameters **95**

Appendix C Convergence of numerical analyses **98**

Appendix D Relation between the RVE size and the static length scale **101**

List of figures

1.1 Examples of metamaterials with diverse periodic microstructures, generated with the assistance of artificial intelligence. 1

2.1 The classification of composite materials [1] 7
2.2 Particle-reinforced composite material 7
2.3 Fiber-reinforced composite material 8
2.4 Laminated composite material 9
2.5 Representative volume element 11
2.6 Algorithm of numerical homogenisation method 14
2.7 Algorithm of computational homogenisation method 16

3.1 Spatial length parameters for a laminate 24
3.2 A laminate bar 29
3.3 Space-time averaging results of normalised averaged Young's modulus E_M/E_{avr} (left) and normalised averaged mass density ρ_M/ρ_{avr} (right). Comparisons between Dirichlet condition (blue line) and periodic boundary condition (red line) for the bar with material impedance contrast $z_1/z_2 = 100$ and constant excitation. 30
3.4 Comparison of space and space-time averaging for normalised averaged Young's modulus $E_{/}E_{\text{avr}}$ (left) and normalised averaged mass density $\rho_{/}\rho_{\text{avr}}$ (right) where material impedance is $z_1/z_2 = 10$ subjected to harmonic excitation with periodic boundary conditions. 31
3.5 Normalised averaged Young's modulus $E_{\text{M}}/E_{\text{avr}}$ versus number of unit cells N_{uc} and number of wave propagations N_{wp} where material impedances are $z_1/z_2 = 10$ (top row), $z_1/z_2 = 100$ (middle row) and $z_1/z_2 = 1000$ (bottom row) subjected to constant (left column) and harmonic (right column) excitations with periodic boundary conditions. 32

3.6 Normalised averaged mass density $\rho_{\mathrm{M}}/\rho_{\mathrm{avr}}$ versus number of unit cells N_{uc} and number of wave propagations N_{wp} where material impedances are $z_1/z_2 = 10$ (top row), $z_1/z_2 = 100$ (middle row) and $z_1/z_2 = 1000$ (bottom row) subjected to constant (left column) and harmonic (right column) excitations with periodic boundary conditions. 33
3.7 Various volume fractions of components of periodic composites for normalised averaged Young's modulus $E_{\mathrm{M}}/E_{\mathrm{avr}}$ (left) and normalised averaged mass density $\rho_{\mathrm{M}}/\rho_{\mathrm{avr}}$ (right) where material impedance contrast is $z_1/z_2 = 1000$ subjected to harmonic excitation with periodic boundary conditions versus the same number of unit cells N_{uc} and wave propagations N_{wp}. 35

4.1 A schematic illustration of the dynamic computational homogenisation method 39
4.2 Homogenised macrostructure decoupled spatially with laminated microstructure through macroscopic integration point 41
4.3 Homogenised macrostructure linked temporally with laminated microstructure through macroscopic integration point 44
4.4 Homogenised macrostructure separated temporally by laminated microstructure 44
4.5 Computational flowchart of dynamic computational homogenisation scheme . 52
4.6 Effect of the number of unit cells on strain and kinetic energies against the reference solution obtained by the DNS. 54
4.7 Macroscopic displacement-time (left) and velocity-time (right) curves for $N_{\mathrm{wp}} = 8$ and various N_{uc} together with the reference solution obtained by the DNS. 54
4.8 Effect of the number of wave propagations on strain $\mathcal{U}$ and kinetic energies $\mathcal{K}$ against the reference solution obtained by the DNS. 55
4.9 Macroscopic displacement-time (left) and velocity-time (right) curves at the value of $N_{\mathrm{uc}} = 8$ for various N_{wp} values with the reference solution obtained by the DNS. 56
4.10 Comparison of different N_{uc} and N_{wp} combinations with regards to strain energy (left) and kinetic energy (right). 57
4.11 Influence of N_{uc} and N_{wp} on macroscopic displacements at the mid-point of the bar for various impedance contrast factors. Error estimations in macroscopic displacements are computed based on the DNS solutions. 57
4.12 Global influences of N_{uc} and N_{wp} on strain energy (left) and kinetic energy (right) for various impedance contrast factors. Error estimations in macroscopic displacements are computed based on the DNS solutions. 58
4.13 Influences of N_{uc} and N_{wp} on macroscopic displacements at the mid-point of the bar for various impedance contrast factors. Error estimations in macroscopic displacements are computed based on the DNS solutions. 59

4.14 Influence of N_{uc} and N_{wp} on strain energy (left) and kinetic energy (right) for various impedance contrast factors. Error estimations in macroscopic displacements are computed based on the DNS solutions. 59

5.1 One-dimensional periodic laminated bar (top) and its equivalent gradient elasticity model (bottom) 63
5.2 One-dimensional gradient elasticity bar (top) and its discrete model comprising of masses linked by springs (bottom) 64
5.3 Dispersion relations with the change of ℓ_{d} - normalised phase velocity versus normalised wave number for $\ell_{\text{s}} = 1\text{m}$ 68
5.4 Computational flowchart of selecting the dynamic length scale parameter ℓ_{d} . 71
5.5 Role of ℓ_{d} in dispersion behaviour simulated by the gradient elasticity theory - displacement curves for the periodic laminate bar at time $t = 280\text{s}$. 75
5.6 Displacement profiles of the periodic laminate bar with low contrast $z_1/z_2 = 10$ (top), intermediate contrast $z_1/z_2 = 100$ (middle) and high contrast $z_1/z_2 = 1000$ (bottom) at the time $t = 280$ s. The bar simulated is with homogeneous (dark grey line), heterogeneous (blue line), gradient model with ℓ_{d} derived analytically [2] (dotted orange line), gradient model with ℓ_{d} estimated numerically [3] (dotted green line) and gradient model with the improved ℓ_{d} presented in Figure (5.4) (red line). 76
5.7 The ratio $\ell_{\text{d}}/\ell_{\text{s}}$ versus a wide range of impedance contrast levels of the material in the periodic laminate bar, simulated by various gradient elasticity approximations. 77

C.1 Space-time averaging results of the bar presented in Figure 3.2 over microscopic time: (a) averaged momentum, (b) averaged velocity, (c) averaged mass density with Dirichlet conditions, (d) averaged mass density with periodic boundary conditions. 99
C.2 The ratio $\ell_{\text{d}}/\ell_{\text{s}}$ versus the length of the periodic laminate bar depicted in Figure 5.2 for low contrast $z_1/z_2 = 10$, intermediate contrast $z_1/z_2 = 100$ and high contrast $z_1/z_2 = 1000$, simulated by gradient model with ℓ_{d} derived analytically [2] and gradient model with the improved ℓ_{d} presented in Figure 5.4.100

List of tables

B.1 Geometric and material properties for the analysis of N_{uc} on the macro- and micro-scale 95
B.2 Geometric and material properties for the analysis of N_{wp} on the macro- and micro-scale 96
B.3 Geometric and material properties for the gradient analyses 97

Nomenclature

Roman Symbols

A	cross-sectional area
B	derivative of shape function matrix
b	body force
d	derivative
$\ddot{u}$	acceleration
$\dot{u}$	velocity
f	force
h	element length
i	imaginary number
z	impedance factor
K	structural stiffness matrix
k	wave number
L	macroscopic length
L_{m}	length of representative volume element
M	structural mass matrix
$\dot{p}$	momentum rate
N	shape function matrix
N	total number of intervals
N_{uc}	number of unit cells

N_{wp}	number of wave propagations
p	momentum
t	time
T	time period
u	displacement
V	volume
c	wave speed
x	spatial coordinate
y	spatial coordinate

Greek Symbols

α	volume fraction
α_{m}	mass penalty parameter
α_{s}	stiffness penalty parameter
Δ	increment
δ	virtual term
ε	strain
ε^*	eigenstrain
ϵ	error
γ	coefficient of length scale parameter
λ	wavelength
∂	partial derivative
ψ	general averaged term
ρ	mass density
σ	stress

Calligraphy

$\mathcal{O}$	truncation error
$\mathscr{C}$	continuous
ℓ	microscopic length
ℓ_{d}	dynamic length scale parameter
ℓ_{M}	macro-fluctuation length
ℓ_{μ}	micro-fluctuation length
ℓ_{s}	static length scale parameter
$\mathscr{K}$	kinetic energy
$\mathscr{U}$	potential energy

Superscripts

f	final
p	penalty
res	residual
T	transpose

Subscripts

0	initial
avr	averaged
c	continuum
d	dynamic
e	elastic
ext	external
f	free
g	gradient
$grad$	gradient
$hete$	heterogeneous

L	left
M	macroscopic
m	microscopic
p	prescribed
p	phase
R	right
s	static

Acronyms / Abbreviations

BVP	boundary value problem
CPU	central processing unit
DNS	direct numerical simulation
RVE	representative volume element

Chapter 1

Introduction

1.1 Background and Motivation

Composite materials have revolutionised engineering due to their unique multiscale characteristics, which exploit their easily tailored properties to achieve enhanced material properties. They have gained significant interest in meeting the rigorous engineering requirements of various industries, including civil engineering, aerospace, biomechanics, and many others. The most common reasons to use composite materials in engineering are low weight, strength and stiffness, design flexibility and cost-effectiveness. Particularly, metamaterials, which can be regarded as a subcategory of composites, have recently gained attention for their ability to facilitate the artificial design of materials. Namely, the advancements of additive manufacturing technologies enable controlling the shape, size and arrangement of microstructures to create a metamaterial with engineered properties for specific applications, as illustrated in Figure 1.1.

Various multiscale modelling approaches have been developed over the years due to an interest in predicting the mechanical behaviour of composite materials considering their

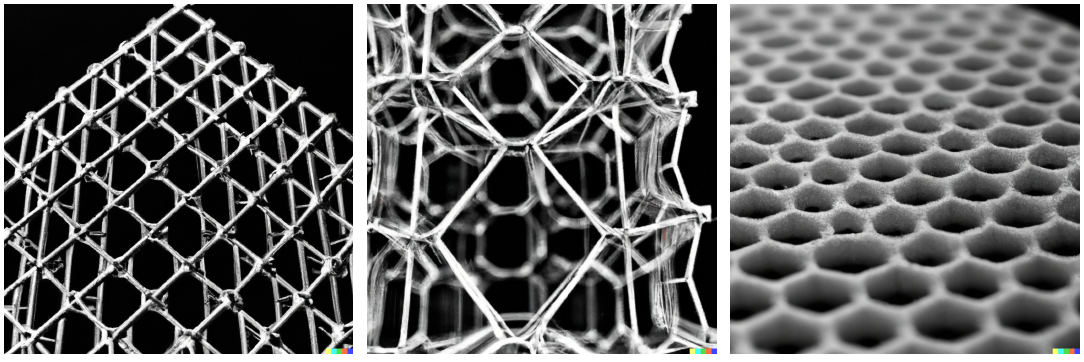

Fig. 1.1 Examples of metamaterials with diverse periodic microstructures, generated with the assistance of artificial intelligence.

multiscale behaviour for engineering practices. The direct simulation methods, where every microstructural detail of the composite materials is modelled separately and explicitly, requires enormous computational effort and cost. As an alternative, the principle of separation of length scales (given by $\ell \ll L$, where ℓ represents the length of microstructure, whereas L represents the length of macrostructure) can be employed to save cost by averaging microscopic problems for the overall behaviour of composite materials. For example, heterogeneous multiscale methods may combine molecular dynamics for microscales with continuum mechanics for macroscales to model advanced characteristics of composite materials. Thus, multiscale methods may be employed for predicting complex microstructural material behaviour and designing new composite materials.

Length scales express the characteristic size of structures that drives the mechanical behaviour. These length scales can range widely: atomic scale, nanoscale, microscale, mesoscale and macroscale. Understanding the different length scales is essential for developing appropriate multiscale models and accurately predicting the behaviour of composite materials. At each length scale, different physical phenomena may become dominant, leading to changes in material behaviour. For instance, at the microscale, the existence of defects (e.g. voids, cracks and dislocations) can have a significant impact on the mechanical behaviour such as reducing its overall strength and ductility. At the macroscale, the overall geometry and loading conditions of a macrostructure become important factors influencing its mechanical behaviour. On the other hand, dynamic excitation such as stress waves, vibrations or impact loads leads to changes in the material behaviour of the microstructure, which in turn noticeably affects its macroscopic behaviour. The influence of dynamic loading on the material behaviour may require reconsideration of the length scales involved in determining the overall mechanical response.

In the context of multiscale modeling, scale interactions act as a bridge between different length scales, allowing for effective communication and transfer of information between them. By enabling the exchange of data across multiple scales, these interactions have an essential significance in accurately predicting the behaviour of composite materials with their complex microstructures. In dynamics, scale interactions require additional transition to accurately capture the dynamic relation between the scales. Apart from length scales, time scales and their interactions between them has not received enough attention in the existing literature [4].

This thesis presents original research that explores and contributes to the improvement of predicting material behaviour of periodically microstructured elastic composites under dynamic excitation, with the aim of addressing dynamic problems in multiscale modeling. The main focus is on achieving improved averaging microscopic problems over length scales

and time scales in dynamics, as well as performing the separation of time scales in multiscale modelling.

1.2 Scope and objectives of thesis

The aim of this thesis is to overcome the difficulties involved in modelling composite materials with their microstructures under dynamic excitations to obtain enhanced material properties for use in engineering applications. To fulfil this aim, the thesis has three main objectives:

1. To establish spatial and temporal connections between macroscopic and microscopic scales that significantly influence the material behaviour of composites. The focus encompasses a wide range of microstructural material parameter sets for impedance contrasts and volume fractions, which are essential components in comprehending the mechanical behaviour of composites. The multiscale methods employed in this thesis facilitate the harmonious integration of the advancements between macroscopic and microscopic scales into existing research and engineering practices.

2. To investigate the appropriate size of a representative volume element (RVE) and time window for microscopic analyses that can help reduce computational effort and expenses while still achieving accurate results. When modelling the behaviour of composite materials, a significant challenge lies in not only estimating their material properties but also taking into account the computational costs involved. For the simplicity to distinguish between the individual spatial and temporal impacts, one-dimensional periodic laminates are employed under various boundary and loading conditions.

3. To identify and quantify microstructural length scales by comparing analytical and numerical connections between the length scales and the RVE. Multiscale methods are increasingly being considered for use in the field of composite material behaviour modelling as a cost-effective and time-efficient alternative to experimental studies. The process of selecting length scales is rigorous, resulting in small enough to emberace all microstructural properties, but in meanwhile large enough to maintain resolution. This careful determination is essential to ensure the most accurate predictions for composite materials with complex microstructural geometry.

1.3 Thesis outline

The thesis is further divided into the following chapters:

Chapter 2 - Literature Review

This chapter provides a literature review of previous research and methodologies regarding the study presented in this thesis. This covers the theories underlying multiscale modelling for composite materials and the principle of numerical methods used for implementing multiscale analyses.

Chapter 3 - Spatial and Temporal Averaging in Homogenisation

This chapter introduces a methodology for determining homogenised material properties of a representative volume element at the microscale by performing space-time averaging on a transient dynamic numerical model. Furthermore, this chapter contributes to the upscaling procedure within the homogenisation framework, which involves transferring information from the microscale to the macroscale. The effectiveness of the space-time averaging procedure is verified by analysing a periodic laminate bar under different boundary conditions, impedance contrasts, and loading conditions, and comparing the results with exact analytical solutions.

Chapter 4 - Spatial and Temporal Transitions in Computational Homogenisation

In this chapter, the methodology of the representative volume element from Chapter 3 is integrated into the dynamic computational homogenisation method to model the mechanical behaviour of periodic composites with engineered microstructures at the multiscales. A new approach is proposed that simultaneously separates length and time scales to improve accuracy in macroscopic response and validate the method against direct numerical solutions. This chapter contains upscaling and downscaling procedures within the computational homogenisation framework that establish scale interactions between the macro and microscales.

Chapter 5 - Dynamic Gradient Elasticity Length Scales

This chapter introduces a procedure for dynamic gradient elasticity theories to select dynamic length scale parameters connected to the size of representative volume element from Chapter 3. The procedure studies a one-dimensional periodically laminated bar with numerical examples to demonstrate the effect of dynamic length scales.

Chapter 6 - Conclusions and future perspectives

This chapter provides an overview of the research works conducted in the thesis, highlights the significant findings and insights, and makes suggestions for future studies to further broaden and enrich the knowledge gained in the subject area of the thesis.

Chapter 2

Literature Review

2.1 Introduction

This chapter describes the background of composite materials and their applications in engineering practices, and contains a review of multiscale methods in current literature relevant to modelling composite materials. The main focus of this chapter is to assess the effectiveness of multiscale methods on estimating the behaviour of composite materials with complex microstructures under dynamic loading conditions, particularly their microstructural effects. While the chapter expresses the challenges involved in modelling composite materials, the detailed theoretical background will be provided in subsequent chapters. The chapter identifies gaps in existing literature and highlights the key objectives of this thesis.

2.2 Composite materials

Heterogeneous materials can be defined as materials having different mechanical and physical properties from one domain to another domain. These differences in the material properties between domains may vary in the range of millimetres to micrometres. In engineering applications with technological developments, most commonly used of heterogeneous materials are composite materials classified as polymers, metals, glasses and ceramics [5]. Besides, multiphase materials can be also defined as a special case of composite materials since their properties are dependent on the components and their microstructures. Composite materials can be categorized based on their constituent phases, namely inclusions, matrix, and interfacial transition zone, as illustrated in Figure 2.1. The interfacial transition zone is a region situated between the inclusions and the matrix, where material properties may gradually change.

Figure 2.2 depicts particle-reinforced composites, which involve embedding one material within the matrix of a second material to enhance its strength. Particles can vary in size and shape, with common shapes being spherical, ellipsoidal, polyhedral, or irregular [1].

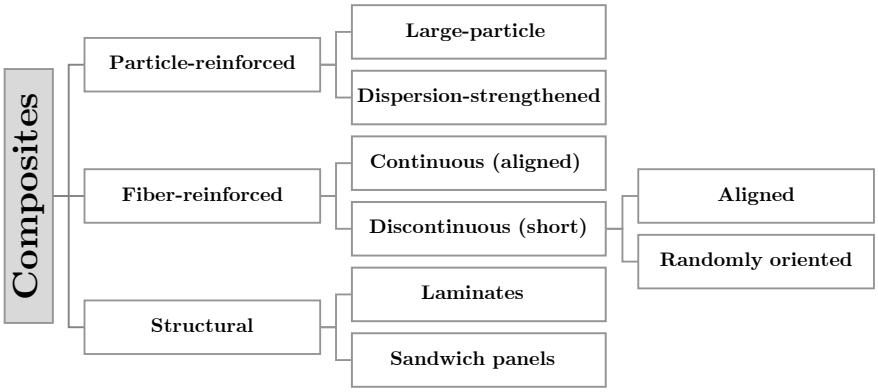

Fig. 2.1 The classification of composite materials [1]

At the microscale, the mechanical behavior of particles is significant, as particle properties such as size, distribution, orientation, and interface can impact the macroscopic response of composite materials [6–8]. Recent advancements in composite manufacturing at various scales have enabled the design of particles and their structures at the microscale to take advantage of their mechanical properties, such as filtering vibrations [9] and suppressing impact/blast effects [10]. Therefore, comprehending the mechanical behaviour of particles at the microscale is essential for controlling their properties in practical engineering applications.

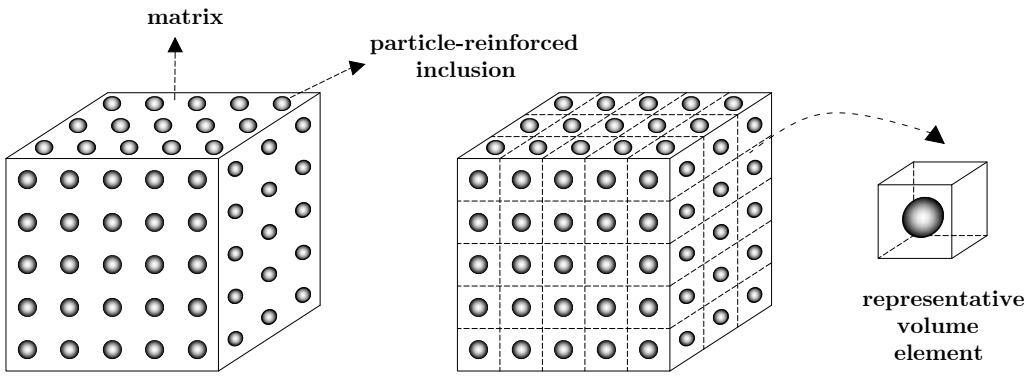

Fig. 2.2 Particle-reinforced composite material

Fiber-reinforced composites consist of high specific strength and elastic modulus fibers embedded within a material matrix. The mechanical properties of these composites depend on several factors, including the type and quantity of fibers, as well as the isotropy or anisotropy of the fibers. As shown in Figure 2.3, fiber-reinforced composites can be classified based on the arrangement of fibers, such as random, aligned, or woven. Among these types, the continuous (i.e. aligned) fiber composite is the most effective for strengthening, as the length of continuous fibers exceeds the critical length. The critical length is the minimum fiber

length required to transfer the entire load from the matrix to the fibers [1]. Similar to particle-reinforced composites, the microscale properties of fiber-reinforced composites, such as geometry, bonding, and clustering, are significant in forming the macroscopic behavior of the composite material [11]. This enables the tailoring of fiber-reinforced composites to obtain high-strength arrangements [12] and cost-effective solutions for engineering problems [13].

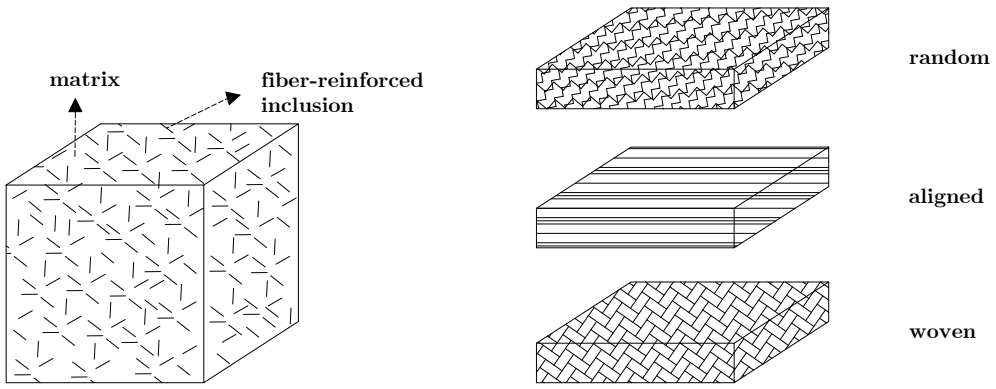

Fig. 2.3 Fiber-reinforced composite material

Lastly, structural composites are required in engineering applications primarily in civil engineering to satisfy the need for high strength and stiffness in materials. Structural composites generally consist of homogeneous and composite materials together and are essentially divided into two groups: laminates and sandwich panels based on constituents and geometrical designs. Firstly, laminate composites presented in Figure 2.4 are composed of different layers providing one structural element so as to meet stiffness, strength and other engineering requirements. Secondly, sandwich panels consist of two outer panels with one thicker core. The outer panels are generally made from stiff and rigid materials, while foams, wood and honeycombs are used for the core layer [1].

One of the elastic dynamic engineering applications for computational composite materials is to generate band and pass gaps in order to control wave and vibration in the materials by arranging frequencies for structural modes. Krushynska *et al.* [14] have recently implemented a design to avoid the effect of impacts, vibration and noise by a combination of band and pass gaps. Moreover, Song *et al.* [15] have investigated the importance of changes in the mechanical and geometrical properties of heterogeneous materials on band gaps and stop bands. As a result, randomness in the mechanical properties was shown to have a minimal effect on the design band-gaps, whereas randomness in the geometrical properties was shown

to be significant in order to reduce wave transmission.

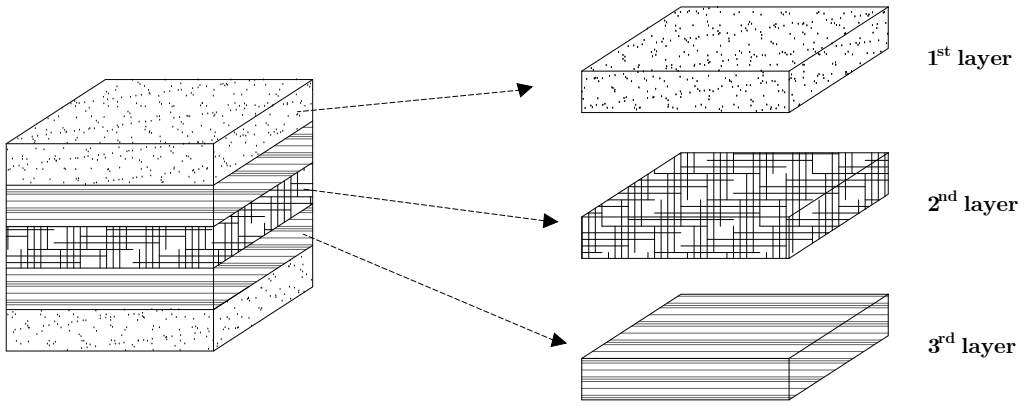

Fig. 2.4 Laminated composite material

It is important to understand and determine the mechanics and physics of composite materials in order to model them effectively. Computational tools of material simulation have been improving to reduce the cost of experiments in composite manufacturing and predict the behaviour of composites. From the point of material modelling in engineering, the composite material can be identified as a homogeneous material with its effective properties. The mechanical characteristics of heterogeneous materials depend not only on size, shape, distribution, but also on their microscopic properties [16]. Consequently, when a relation between macroscopic and microscopic behaviours is linked, this allows designing mechanical properties of a microstructure for a required industrial purpose.

2.3 Multiscale methods

Multiscale modelling has been developed over the years due to an interest in predicting the mechanical behaviour of composite materials considering their multiscale behaviour for engineering practice [17–20]. Multiscale methods have been initially investigated for problems of heat conduction in composite materials and mechanical properties and deformations of composites [21]. Heterogeneous multiscale methods may combine molecular dynamics for microscales with continuum mechanics for macroscales to model advanced characteristics of composite materials [17]. Therefore, multiscale methods are employed for predicting complex microstructural material behaviour and designing new composite materials.

Traditional multiscale methods such as multigrid are aimed at resolving the details of the microscale model, resulting in a significant computational cost [22]. In order to achieve a cost-effective multiscale analysis, the focus should be on the special features of the microscale problem instead of all microstructural details. Heterogeneous multiscale methods aim to approximate the macroscopic behaviour and estimate the required information for the macroscale model from the microscale model [19]. The main challenge is to identify and utilize these features to capture the macroscopic behaviour effectively.

Multiscale methods can be categorised into three different ways to use the special features of the microstructure to represent the overall material response. First, the microscopic model is only required for localisation such as cracks, dislocation, and contact lines. In contrast, the macroscopic model is used for unaffacted parts. Therefore, the macro-micro coupling is limited to a localisation area. On the other hand, macroscopic models may be obtained from the homogenised solution of associated microscopic models with the principle of scale separation. The last category is constituted from the mixture of those two approaches, where certain sections of the structure are completely solved at the microscale, while other parts are examined with the effective macroscopic response [4, 23].

Multiscale methods establish connections between different scale models for composite materials, which can range from atomic to macroscopic or intermediate micro and meso scales, depending on the specific application. A representative volume element (RVE) is one such scale model that is particularly useful for addressing complex microstructural problems [24, 25]. In the case of periodic composites, the macroscopic solution is obtained from the approximation of a unit cell [26]. However, for complex geometries, statistical homogeneity must be ensured by the RVE as demonstrated in Figure 2.5. When the RVE size is too small, the macroscopic response may not capture the essential features and behaviours of the material, leading to inaccurate results. In contrast, when the RVE size is too large, the numerical analysis may become computationally expensive and time-consuming. Large RVE sizes may also smooth out local variations and heterogeneities, leading to a loss of accuracy and resolution.

Numerous studies have focused on determining the appropriate size of the representative volume element (RVE) for various scenarios. Kanit *et al.* [27] investigated the effects of material contrast and volume fractions on RVE size, and this study has shown that RVE size generally increases with higher contrast in material properties. In the case of fiber-reinforced composites subjected to transient dynamics, Liu *et al.* [28] showed that a larger RVE size is necessary to achieve convergence of macroscopic material properties. Stroeven *et al.* [7] conducted a study on granular materials and found that a lower particle density distribution tends to lead to larger RVE sizes. Apart from the influence of material properties, defor-

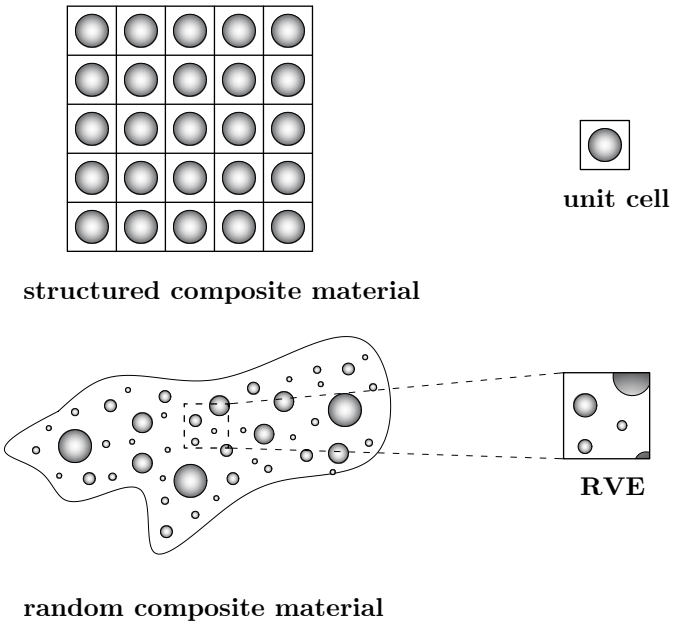

Fig. 2.5 Representative volume element

mation and failure phenomena such as localisation can also affect the RVE size. Nguyen *et al.* [29] reported that the RVE size increases at the point of localisation to obtain material response that is independent of the RVE size. Gitman *et al.* [30] conducted detailed studies on the existence and determination methodologies of RVE, highlighting the significant effect of RVE size on the accuracy and reliability of results obtained from numerical simulations.

In multiscale modelling, several studies have been conducted to establish the connection between material parameters in gradient elasticity theories and numerical parameters in homogenisation methods [31–33]. As the concept of the RVE is widely used in the multiscale modelling, it becomes important to identify and quantify the RVE to obtain an accurate overall material response. While the static RVE size has been extensively investigated, there is currently no study that achieves quantifying the dynamic RVE size, despite its known larger size in comparison to the static RVE. Thus, the question is raised as to "What the appropriate size should be for the dynamic RVE in comparison to the static RVE?". This thesis will investigate the dynamic RVE size in homogenisation methods and its relationship to material length parameters in gradient elasticity theories.

2.4 Homogenisation methods

Determining the overall characteristics of composite material is challenging due to size, shape and spatial distribution of heterogeneity in the material. Experimental studies can

be carried out to characterise the behaviour of these materials, but these are costly and time-consuming. Moreover, the significant difference in length scales between macroscopic and microscopic scales of composite materials causes enormous computational effort when the finite element method is employed. Instead of modelling all microscopic properties in composites, the effective properties can be calculated to obtain a constitutive model. This procedure is so-called "homogenisation" by Suquet [34]. Several homogenisation methods have been effectively used to model the mechanical characteristics of composite materials.

2.4.1 Analytical homogenisation

The simplest technique of homogenisation is the rule of mixture approach has been developed by Voigt [35] and Reuss [36] for composites. This approach enables the calculation of the averaged material properties from their composite components. For instance, the averaged macroscopic mass density ρ_{M} reads

$$\rho_{\mathrm{M}} = \sum_{k=1}^{K} \alpha_{\mathrm{k}} \rho_{\mathrm{k}} \tag{2.1}$$

where ρ_{k} and α_{k} are the kth microscopic mass density and its kth volume fraction. Eshelby [37], who was pioneer of analytical homogenisation technique, investigated the effect of an inclusion embedded in a matrix on the stress distribution of particle reinforced heterogeneous materials. He proposed the equivalent inclusion method by using Eshelby's tensor S to simulate the behaviour of an inhomogeneous inclusion that of a homogeneous inclusion with initial and associated equivalent eigenstrains. S is used to find the actual strain ε for a matrix with an inclusion based on the eigenstrain ε^*

$$\varepsilon = S\,\varepsilon^* \tag{2.2}$$

The eigenstrain ε^* describes the strain fields inside an inclusion in an elastic material. The eigenstrain ε^* represents a change in the elastic properties of the inclusion due to the presence of the surrounding material. The term "eigen" comes from the German word meaning "inherent"; hence, the eigenstrain refers to the internal strain that arises from the inherent properties of an inclusion, rather than external factors. S is defined as a function of material and geometrical properties, but not a function of size. Eshelby's transformation strain is constant for an ellipsodial inclusion embedded in a matrix. Eshelby's method has been developed by a series of studies to obtain a good estimates for effective material properties [38, 39]. However, Hill [40] considered Eshelby's effective medium approximation as untrustworthy prediction for highly divergent material properties in a material owing to that Eshelby's Eq (2.2) is insufficient to perceive dissimilarity of phases.

Eshelby's method has been modified using different mathematical approaches over the years. Firstly, Nemat-Nasser and Taya [41] formulated Eshelby's transformation strain using the Fourier series for periodic heterogeneous materials with inclusions or voids. This method has been also applied to various static/dynamic periodic composite material problems for different type of inclusions and voids. This method is applicable for periodic composite materials whose transformation strains varies with space. Nevertheless, a simplification in the use of Fourier series assumed by Nemat-Nasser and Taya [41] caused discrepancies from the true solution. Moreover, the limitations of Eshelby's method with Fourier reformation were eliminated by Chen and Schuh [42]. In this technique, the equations were derived in a different way to reduce the number of assumptions for spherical and cubic inclusions embedded in a periodic structure. Despite the results were found to be close to the exact solution and seem computationally achievable, the applicability of this method is limited to the composite materials with periodic microstructures only.

Another common analytical homogenisation method is asymptotic homogenisation, also known as mathematical or periodic homogenisation. In this method, the differential equations are used to generate a function with asymptotic expansions in order to implement the behaviour of heterogeneous materials in two scales. A significant benefit of this method compared to other analytical homogenisation methods is that stress and strain distributions arising from the microstructure of heterogeneous materials can be determined. Chen and Fish [43] have performed asymptotic expansions for a bi-laminate heterogeneous material to investigate wave propagation through such periodic structure. The fast temporal scale was shown to cause an unbounded growth in displacements, so the dispersion effect [1] could not be captured. They have demonstrated that once fast spatial and slow temporal scales are combined, dispersion effects were captured. Even though a relationship between macrostructure and microstructure is formulated to show effective properties, the asymptotic homogenisation method is inadequate to expand the method for more general microstructural geometries.

Carta and Brun [3] developed another asymptotic homogenisation from Brillouin's lattice model to investigate the dispersion effects of laminate structures. The method is effective for a moderate difference between material properties of matrix and inclusion, but Chen and Fish [43] shows better results on the condition that there is a high impedance [2] difference between the material components. It has been recommended that a homogenisation analysis

[1] Wave dispersion is a phenomenon in which waves of different frequencies ot wavelengths travel at different speeds, leading to the separation or spreading out the wave components. The dispersion can result from the reflection and refraction of waves.

[2] Mechanical impedance is how material resist mechanical waves, such as vibrations, seismic waves or any oscillations. The impedance depends on the material properties and can be characterised by mass, stiffness, and damping properties.

needs to be preceded by a dispersion analysis to determine the microstructural properties of bi-laminate composites.

2.4.2 Numerical homogenisation

Numerical homogenisation is an alternative technique to analytical homogenisation used to predict the behavior of heterogeneous materials by replacing them with equivalent RVEs, as shown in Figure 2.6. The main advantage of the numerical homogenisation is that it does not require assumptions on the micro-level, except for geometry and constitutive behavior, making its implementation more straightforward. However, the primary limitation of this method is that a format for the macroscopic constitutive model must be established a priori.

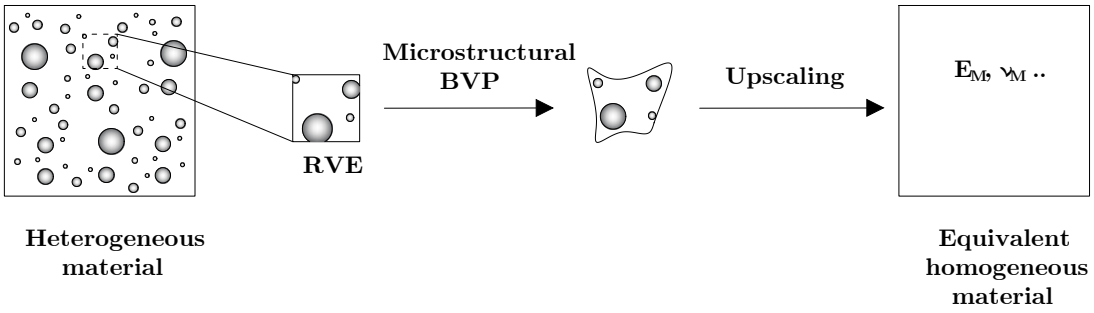

Fig. 2.6 Algorithm of numerical homogenisation method

Van der Sluis *et al.* [44] employed the numerical homogenisation method to elastoplastic solids by averaging Cauchy stresses. In the modelling of the behaviour of elastoviscoplastic solids, the plastic work rate on the macro-level is equal to an average of the plastic work rate of the RVE on the micro-level. The researchers compared the results of the developed numerical homogenisation for a polycarbonate plate as a homogenised model with those implemented by the finite element model as a discretized model. The force-displacement graph depicted a good correlation between homogenised and heterogeneous models, except for the softening regime where a clear deviation was observed.

The numerical homogenisation was also implemented based on a strain energy averaging, meaning that the mechanical behaviour of a representative volume element is presented the same behaviour with its associated macroscopic model based on the strain energy equivalence [45]. The equivalence of a generic value is given by

$$\psi_{\mathrm{M}} = \frac{1}{V} \int_{V} \psi_{\mathrm{m}}(x, y)\, \mathrm{d}V \tag{2.3}$$

where ψ_{M} and ψ_{m} are the averaged macroscopic quantity and its microscopic quantity of the volume domain V. This numerical homogenisation method was performed on hyper-

elastic solid foams to investigate the material behaviour under finite strain and infinite strain. The deformation behaviour of the material was evaluated to vary with infinitesimal strain from the equivalence behaviour. Additionally, the developed numerical homogenisation method was found to be applicable to three-dimensional microscopic solids with heterogeneity.

A Matlab code of numerical homogenisation of periodic composites was developed by Andreassen and Andreasen [46] for various unit cells geometries, including a square, rectangle, and parallelogram. The use of Matlab for numerical homogenisation is efficient and cost-effective, even for 2D and 3D unit cells, compared to modelling continuous materials. Therefore, numerical homogenisation can be considered an effective approach to model the static behaviour of heterogeneous materials in terms of time and cost savings.

2.4.3 Computational homogenisation

The computational homogenisation method, introduced by Suquet [47], builds on the concepts of analytical and numerical homogenisation methods to establish macrostructural and microstructural relationships. In contrast to other homogenisation, the macroscopic material behaviour is predicted by the link between homogeneous macrostructure and heterogeneous microstructure. The computational homogenisation method is a more recent and comprehensive approach than its analytical and numerical counterparts. Even though the numerical homogenisation method required less microstructural information, leading to more computationally efficiency, the computational homogenisation method provides more accurate results and captures microstructural effects. The computational homogenisation method enables solving boundary value problems (BVPs) both at the macro and microscales in order to achieve capturing complexity of microstructures. Moreover, the ability to generate detailed microstructure makes computational homogenisation method applicable to non-linear and time-dependent problems [48].

The computational homogenisation method has not replaced other homogenisation methods yet, but it is clearly a fundamental tool for mechanics of complex materials. Namely, the computational homogenisation method gives direct solutions compared to other homogenisation methods, so there is no need to evaluate solutions of material at the macroscale [49]. As long as materials at the microscale are well-defined to estimate the behaviour of heterogeneous materials, results by the computational homogenisation method are close to the exact solution. Geers *et al.* [50] have addressed the challenges encountered in computational homogenisation method. These include developing effective boundary value problems at both micro and macro scales, addressing dynamic cases that incorporate micro-inertia effects and wave propagation, and developing upscaling features that take into account spatial-temporal

and kinematic factors.

Compared to analytical and numerical homogenisation, the computational homogenisation method involves solving a boundary value problem at both the macro and microscales. The macroscopic solutions are used as inputs for the microscopic boundary value problem, while the microscopic solutions are used as inputs for the macroscopic boundary problem through macroscopic integration point. This generates the cycle illustrated in Figure 2.7 for the computational homogenisation method. The microscopic boundary value problem is assigned to each macroscopic integration point obtained using a finite element discretisation [51]. Even though the form of nested boundary value problems causes an increase in computational effort, the computational homogenisation method accelerated by parallel computations is still faster than the direct numerical simulation method [52, 53].

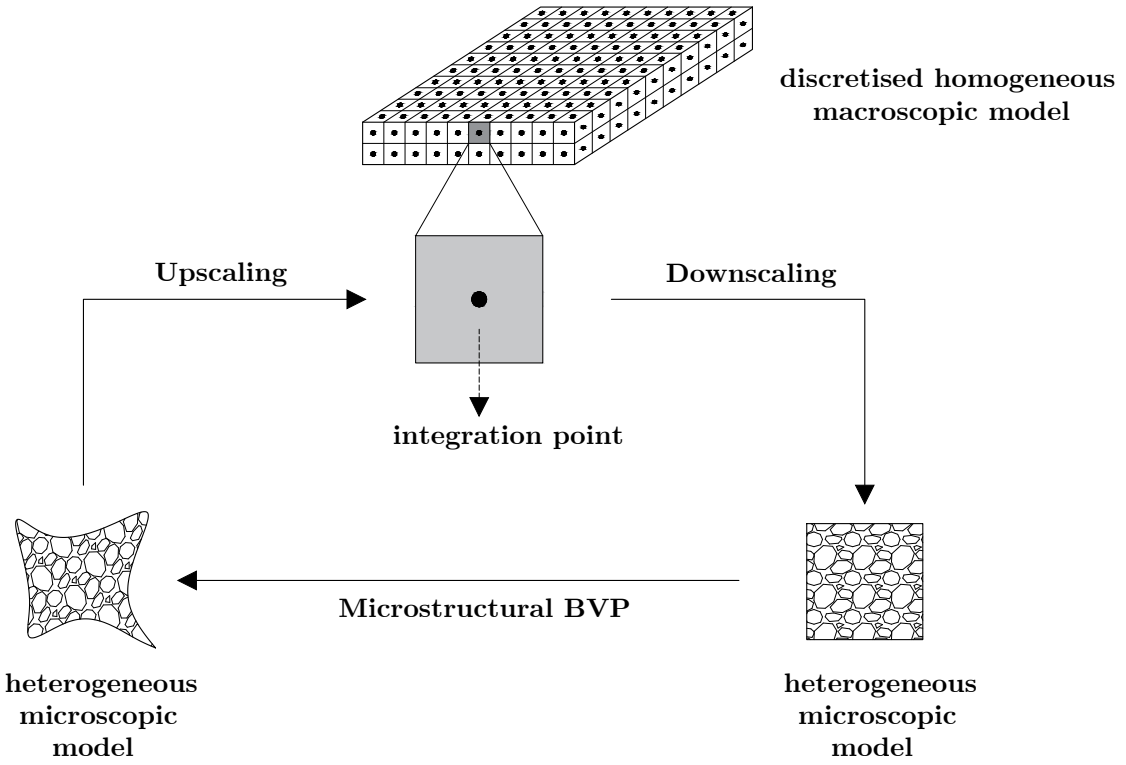

Fig. 2.7 Algorithm of computational homogenisation method

Several studies has been conducted to integrate the computational homogenisation method into the finite element framework to facilitate industrial use of this method [54–56]. Initially, Abdulle and Nonnenmacher [54] have developed a standard finite element code for computational homogenisation, which can be applied to elliptic and parabolic time-dependent problems. From the perspective of a simultaneous coupling, a material at the macroscale

is discretized, and then each RVE is solved on the micro-level with unknown macroscopic data, following that a macroscopic result is gained from the microscopic solution. There is no need to implement iterations for linear problems, whereas iterations must be implemented at the macroscale for nonlinear problems. Numerical results of the analysis were obtained for periodic, irregularly periodic and random tensors [54].

In statics, for any type of boundary conditions (e.g. linear displacement, periodic, uniform traction), Hill-Mandel condition establishes a energy consistency in the computational homogenisation framework, that holds [25]

$$\langle \sigma_{\mathrm{m}}\, \varepsilon_{\mathrm{m}} \rangle_{\mathrm{x}} = \langle \sigma_{\mathrm{m}} \rangle_{\mathrm{x}}\, \langle \varepsilon_{\mathrm{m}} \rangle_{\mathrm{x}} \tag{2.4}$$

where σ_{m} and ε_{m} are microscopic stress and strain, respectively, and $\langle \cdot \rangle_{\mathrm{x}}$ denotes the spatial averaging operator as defined in Eq. (2.3). This discretized averaging technique enables bridging a link between the macro and microscales [57]. Replacing the first term from Eq. (2.4) with macroscopic stress σ_{M} and strain ε_{M}, the coupling between the macro and microcales gives

$$\sigma_{\mathrm{M}}\, \varepsilon_{\mathrm{M}} = \langle \sigma_{\mathrm{m}} \rangle_{\mathrm{x}}\, \langle \varepsilon_{\mathrm{m}} \rangle_{\mathrm{x}} \tag{2.5}$$

The computational homogenisation method has been extensively applied on quasi-static problems in various material types, including periodic composites [58, 59], polycrystalline materials [60], porous materials [61] and cellular materials [62]. Notably, the use of this method in materials with complex microstructures has led to emerging extensions of the computational homogenisation technique. These extensions have facilitated a more comprehensive understanding of the mechanical behaviour of materials, particularly microstructural features. For instance, one extension is the second-order computational homogenisation introduced by Kouznetsova *et al.* [63]. This approach incorporates a higher-order gradient macroscopic model and a standard microscopic model, enabling the consideration of the effect of microstructural size on the macroscopic material behaviour. The study revealed that the second-order homogenisation provides a more accurate estimation of the microstructural effects on the mechanical behaviour of the material, even when using fine mesh discretization.

In addition to the extensions for quasi-static problems, Pham *et al.* [64] presented the dynamic computational homogenisation algorithm to analyse metamaterials under dynamic excitation. Similar to static computational homogenisation, the dynamic algorithm simultaneously solves the boundary value problems at both macro and microscales. To accommodate dynamic counterpart, Pham *et al.* [64] extended the Hill-Mandel principle to include macroscopic stress from a static part, as well as macroscopic linear momentum from a kinematic part. In addition to the work of strain, the algorithm integrates the work of acceleration

into the variation of work performed on both scales, leading to the Hill-Mandel condition in dynamics. Thus, Eq. (2.5) becomes

$$\sigma_{\mathrm{M}}\,\varepsilon_{\mathrm{M}} + \frac{d}{dt}p_{\mathrm{M}}\,u_{\mathrm{M}} = \langle\sigma_{\mathrm{m}}\rangle_{\mathrm{x}}\,\langle\varepsilon_{\mathrm{m}}\rangle_{\mathrm{x}} + \langle\frac{d}{dt}p_{\mathrm{m}}\rangle_{\mathrm{x}}\,\langle u_{\mathrm{m}}\rangle_{\mathrm{x}} \tag{2.6}$$

where p_{m} and u_{m} are microscopic momentum and displacement, respectively. This homogenisation framework has been applied to analyse a particle-reinforced heterogeneous material in dynamics. In comparison with the results of direct numerical simulation (DNS), the results of this framework presents good correlations at both the macro and microscales [64].

Van Nuland *et al.* [65] have been performed the dynamic computational homogenisation on a nonlinear resonant acoustic metamaterial by transferring macroscopic constitutive tangents obtained from the Newton-Raphson method. The dynamic computational homogenisation method extended with the Newton-Raphson method was applied on the nonlinear metamaterial with rubber-coated inclusions, resulting in good estimation of band gap characteristics [65]. Furthermore, the boundary value problems have been analysed within frequency domain to investigate the behaviour of heterogeneous materials under dynamic loading at different frequencies [66].

2.5 Gradient elasticity theories

Classical continuum theories consider only stress at a given point meaning that the effect of the neighbourhood is not taken into account. Namely, kinematic equations are based only on displacements, not on strains and higher-derivatives. Thereby, in statics, classical continuum theories remain incapable of overcoming singularity problems. Also, it is crucial to compare the characteristic length of an RVE with the wavelength of excitation. The main reason for this is that if these values are close to each other, dispersion happens, and this dispersion effect cannot be captured by classical continuum mechanics. Consequently, a lack of internal length in classical continuum causes various problems such as dislocation analysis, localisation problems, wave propagation and singularities so that classical continuum theory should be improved by the gradient elasticity theory in order to eliminate those disadvantages. There are various formats of gradient elasticity to capture microstructure effects by internal length.

Various versions of gradient elasticity theories can be explored by varying number of gradient terms incorporated into the energy functions, including both potential and kinetic energies. Mindlin's pioneering work in 1964 presented a comprehensive formula for the potential and kinetic energies with high-order terms. In Mindlin's theory, the one-dimensional potential $\mathscr{U}_{\mathrm{g}}$ and kinetic $\mathscr{K}_{\mathrm{g}}$ energies may be written as

$$\mathscr{U}_{\mathrm{g}} = \frac{1}{2}\, E\, \varepsilon^2 + \mathscr{U}_{\mathrm{m}}\left(\frac{\partial \varepsilon}{\partial x}\,; \frac{\partial^2 \varepsilon}{\partial x^2};\, \cdots\right) \tag{2.7}$$

and

$$\mathscr{K}_{\mathrm{g}} = \frac{1}{2}\, \rho \dot{u}^2 + \mathscr{K}_{\mathrm{m}}\left(\frac{\partial \dot{u}}{\partial x}\,; \frac{\partial^2 \dot{u}}{\partial x^2};\, \cdots\right) \tag{2.8}$$

where u and ε displacements and strains, receptively. Material parameters E and ρ are Young's modulus and mass density, respectively. Thus, Mindlin's 1964 theory on linear elasticity with microstructures laid the foundation for further research in gradient elasticity theories. However, Mindlin made excessive assumptions to simplify a complex relation between macroscale and microscale equations, and therefore, these simplifications are a potential limitation of the theory. Further research has explored alternative approaches to address this issue. Two popular theories of gradient elasticity in statics are the Aifantis [67] method, which uses gradients of displacements to account for microstructural effects, and the Eringen method [68], which uses gradients of stresses instead [69]. These constitutive relations are given by

$$\text{Aifantis' theory:} \quad \sigma = E\left(\varepsilon - \ell^2 \frac{\partial^2 \varepsilon}{\partial x^2}\right) \tag{2.9}$$

$$\text{Eringen's theory} \quad \sigma_{\mathrm{g}} - \ell^2 \sigma_{\mathrm{g}} = E\, \varepsilon \tag{2.10}$$

where σ is stress, ℓ is the internal length of a microstructure, and the superscript g represents gradient dependence. In gradient elasticity theories, the constitutive equation is given by

$$E\left(\frac{\partial^2 u}{\partial x^2} - \ell^2 \frac{\partial^4 u}{\partial x^4}\right) + b = 0 \tag{2.11}$$

where b is the body force. Solving the fourth-order equation can be challenging, and to address this issue, Ru and Aifantis [70] improved an operator split method. This method involves dividing Eq. (2.11) into two sets of second-order equations, enabling a practical solution to the complex Eq. (2.11), as follows

$$E \frac{\partial^2 u_{\mathrm{c}}}{\partial x^2} + b = 0 \tag{2.12}$$

with

$$u_{\mathrm{g}} - \ell^2 \frac{\partial^2 u_{\mathrm{g}}}{\partial x^2} = u_{\mathrm{c}} \tag{2.13}$$

where subscripts c and g denote the classical elasticity component and the gradient elasticity component. In a work by Metrikine and Askes [71], the influence of the sign of higher-order gradients in Aifantis' theory was examined. The research found that the positive sign of higher-order gradients leads to the creation of heterogeneity, while a negative sign results in

the smoothing of heterogeneity in Aifantis' constitutive equation, namely

$$\sigma = E\left(\varepsilon \pm \ell^2 \frac{\partial^2 \varepsilon}{\partial x^2}\right) \tag{2.14}$$

These findings provide insights into how materials respond to different conditions.

Gradient elasticity theories have been extended to dynamics in order to study the influence of microstructural effects on the macrostructural dynamic response. A dynamic consistent gradient model was introduced by Metrikine and Askes [71], showing that the negative sign of strain gradients remains stable, but the positive sign of strain gradients is unstable. For this reason, these unstable strain gradients have been replaced by stable acceleration gradients [72]. Even though realistic and consistent dispersive results have been obtained by this method, the method requires positive definiteness of two energy densities so that the inertia length scale should be higher than the stiffness length scale [71]. The application of the gradient elasticity theories in dynamics on composite laminates, concrete and alimunium and bismuth with nanostructured crystals has been conducted by De Domenico and Askes [73] to investigate their behaviour. The research has revealed that incorporating higher-order gradient terms significantly enhances the ability to capture dispersive characteristics in the material response.

While gradient elasticity is a useful tool for incorporating microstructural effects, it is important to consider the computational cost and CPU time required for numerical implementation. Bennett and Askes [74] addressed this issue by implementing an operator split and time discretization method for dynamic consistent gradient elasticity. However, the numerical implementation of the constitutive equation requires $\mathscr{C}^1$-continuous interpolation functions, which can be a major disadvantage of this method. To address this issue, the Ru-Aifantis theorem for gradient elasticity was derived for the equation of dynamic consistent gradient elasticity [72]. De Domenico and Askes [75] evaluated the numerical performance of the dynamically consistent gradient model in terms of various discretisation methods in time. Firstly, their study revealed that the use of explicit time integration in gradient elasticity did not provide any advantage since the lumped mass matrix cancelled out all higher-order gradient terms. Therefore, implicit time integration is more favourable for gradient elasticity theories due to its accuracy and stability advantages.

The accuracy of the gradient elasticity model is influenced by the identification and quantification of length scale parameters associated with gradients. Several studies have attempted to establish a link between the length scale parameters and the size of the Representative Volume Element (RVE) in multiscale methods [73, 76, 77]. While the choice of length scale parameter in statics has been achieved through analytical derivations of the

RVE size [77], the determination of the length scale parameter in dynamics has not been established yet [69].

2.6 Commentary

Multiscale methods have been extensively used to model the mechanical behaviour of composite materials with complex microstructures under dynamic excitation. To meet the modelling requirements of advanced composite materials (e.g. metamaterials) for engineering practice, computational homogenisation methods and gradient elasticity theories have been developed in the literature. Designing the RVE is crucial in achieving an accurate prediction of material response in multiscale modelling, as microstructural effects influence macrostructural material behaviour. In computational homogenisation methods, the microstructural boundary value problem is applied over the RVE, while in gradient elasticity theories, length scale parameters are linked to the RVE size. The importance of identifying and quantifying the RVE has been highlighted in existing literature. Briefly, the RVE in statics size can be determined, leading to satisfactory prediction of material behaviour for composites and connection to the static length scale parameter. However, the RVE size in dynamics is not well defined, and its relation to the dynamic length scale parameter has not yet been established adequately.

In Chapter 3, the question of how to determine a dynamic RVE size will be addressed, together with the associated question of what constitutes an appropriate time window for time averaging using *numerical homogenisation*. In Chapter 4, dynamic RVE sizes will be employed in a dynamic *computational homogenisation* framework. Finally, Chapter 5 will make the transition from numerical and computational homogenisation towards *analytical homogenisation* using a gradient elasticity framework.

Chapter 3

Spatial and Temporal Averaging in Homogenisation

This chapter presents a new approach for estimating the homogenized material properties of a representative volume element at the microscale. This is accomplished through the use of space-time averaging on a transient dynamic numerical model. Additionally, this chapter enhances the upscaling process within the homogenisation framework, which involves transferring information from the microscale to the macroscale. The material detailed in this chapter was initially prepared for a journal article[1].

[1]Yağmuroğlu İ., Ozdemir Z. and Askes H. "Spatial and temporal averaging in the homogenisation of the elastodynamic response of periodic laminates", *European Journal of Mechanics / A Solids*, vol. 100, p. 104973, 2023.

3.1 Introduction

In multiscale methods, consistency between micro and macroscales is achieved by the averaging theorems and homogenisation methods. The pioneering micro-macro averaging method, the Hill-Mandel Principle of Macrohomogeneity, is only valid when separation of scales can be assumed [25, 78]. The theory of micro-macro averaging is set up by the spatial volume average of microscopic virtual work with respect to the virtual work of a macroscopic material point. As such, heterogeneities in a microstructure are averaged to reflect effective overall properties in a macrostructure. Classical micro-macro averaging methods have been implemented to predict the material behaviour of composites, when micro-inertia and non-local effects are negligible [79–81]. In statics, the micro-macro averaging method enables the stress and strain averaging of the microscale to represent constitutive behaviour on the macroscale. In other words, macroscopic effective material quantities are extracted from the result of associated microscopic boundary value problems. These averaged macroscopic quantities rely exclusively on the quality of an associated microscopic model. Accordingly, the microstructure boundary value problem must be solved, e.g. by using a finite element model.

In the classical work of multiscale modelling, a microstructural model can be described as the representation of microheterogeneity of the material. The concept of representative volume element (RVE) is applied to predict the material behaviour of a heterogeneous microstructure [31, 51]. An RVE is a microstructural model of the material that has finite dimensions. The RVE size, denoted as L_{m}, should be large enough to encapsulate all microscopic features as a representation of a macroscopic model and, at the same time, as small as possible to save computational cost. The identification and quantification of the RVE are important issues in multiscale modelling problems. Several analytical, numerical and experimental studies have been performed to identify and quantify RVEs in statics and dynamics [24, 26, 27]. In statics, even though the RVE size can be defined statistically for linear-elastic and hardening material behaviour, the RVE was demonstrated not to exist when the material is in the softening regime, because strain localisation implies separation of scales is no longer applicable [30]. The RVE is determined by geometric and material properties of the microstructure so that the periodicity of both material and boundary conditions should be considered. In the context of the periodicity of material, the RVE size of periodic microstructures certainly is equal to the size of a microstructural unit cell ℓ. However, it is more challenging to determine a RVE for random microstructures [82]. On the other hand, the RVE size with periodic boundary conditions was demonstrated to be smaller than the RVE size with non-periodic boundary conditions. In addition, the influence of periodicity in material and boundary conditions on the RVE size varies depending on the loading conditions [30].

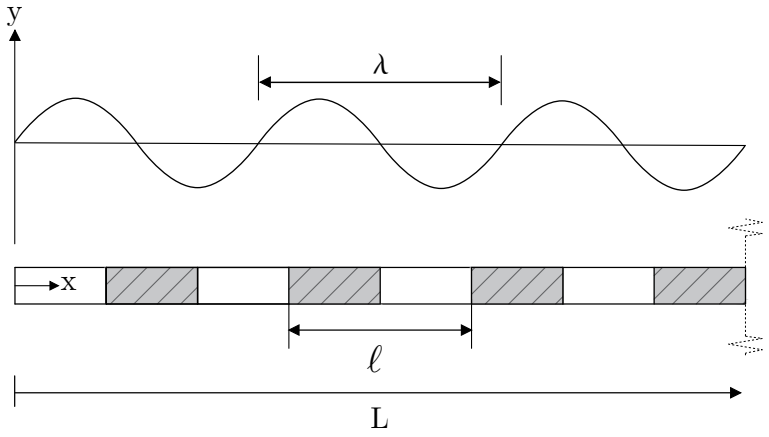

Fig. 3.1 Spatial length parameters for a laminate

In dynamics, the increasing interest in advanced engineering applications such as band gaps and acoustic metamaterials has highlighted the importance of wave propagation phenomena in composite materials [66, 83]. In the context of multiscale modelling, averaging and homogenisation methods have been developed to incorporate inertia effects and body forces in order to model wave behaviour of composite materials subjected to dynamic excitations [43, 84–87]. Averaging and homogenisation methods formulated in the frequency domain have become popular due to the increase in the use of acoustic metamaterials and phononic crystals, yet the frequency domain can be only applicable for linear elastic materials and periodic microstructures [88–90]. Accordingly, multiscale methods based on the time domain are more comprehensive for general cases (e.g. complex time-dependent boundary conditions) [64]. The modelling of transient interactions and micro-inertia effects in space and time implies that the wavelength of applied excitations needs to be considered in addition to the size of microstructure and macrostructure. Therefore, for dynamic problems, three physical length parameters are involved in total, as shown in Figure 3.1. When the shortest wavelength in the initial disturbance λ is much larger than the size of the microstructure ℓ and the size of the structure L is much larger than its microstructure ℓ, the response can be assumed as a homogeneous material behaviour on the macro level. As a result, the RVE-based multiscale problem can be solved by the classical quasi-static homogenisation formulations. Conversely, when the wavelength approaches the size of microstructure, wave dispersion becomes significant and must be modelled by averaging theorems with effective constitutive relations that account for the dynamic response of the material. Similar to statics, RVE-based multiscale modelling has been widely implemented in dynamics for the contribution of micro-inertia and body forces [91]. However, the size of RVE in statics is not necessarily equal to the size of RVE in dynamics due to the dispersive behaviour resulting from the reflection and refraction of the wave. Therefore, the RVE size in dynamics should be determined separately to obtain accurate averaging between micro and macrostructure.

For a periodic laminate, the size of RVE in dynamic was argued to be larger than the unit cell size and dependent on the component properties [2]. Moreover, a higher contrast in the component properties, thus exhibiting more dispersive behaviour, was shown to lead to increase in the RVE size [92].

The classical Hill-Mandel Principle of Macrohomogeneity as used in statics concerns only micro-macro averaging in space. However, in dynamics macro and microscale variables are affected by temporal fluctuations as well as spatial fluctuations. Several extensions of the Hill-Mandel Principle theorems have been recently proposed for the micro-macro averaging in dynamics, including micro-inertia and body forces [57, 64, 91, 93]. In particular, Reina Romo [93] discusses homogenisation in dynamics with the option to apply averaging in time as well as in space. As explained by Reina Romo [93], time averaging is equivalent to assuming the principle of separation of time scales, in addition to the principle of separation of length scales. When time averaging is considered in addition to space averaging, a relevant question arises: what is the time window over which time averaging should be carried out?

As a matter of principle, in RVE-based multiscale problems, taking microstructural sample sizes larger than the RVE size should not have an impact on the response of the macrostructure. Extending this principle to the time dimension, a time window for averaging should be selected such that taking a larger window would not affect the homogenised macroscopic response. This section presents how to select this time window for time averaging, and how it relates to the RVE size that is used for the averaging in space.

An extended version of the Hill-Mandel Principle of macro-homogeneity is implemented with the finite element method to investigate the influence of the RVE size and time averaging window in dynamics. The micro-to-macro transition is carried out by averaging in space and time. With this setup, the influence of RVE size and time averaging window can be investigated to obtain the most accurate predictions for the macrostructural properties. In particular, by focussing on a laminated bar with one spatial dimension, it will be possible to assess whether it is possible to trade off RVE size against length of the time averaging interval, and vice versa. The analysis is repeated for various boundary conditions, a number of material parameter sets and different loading regimes to test the sensitivity of the findings.

3.2 Space averaging

The static averaging approach enables a macroscopic integration point to replace its microscopic counterpart obtained by integrating over the size of the RVE. The volume average of the RVE stress field subjected to the local macroscopic strain tensor defined as prescribed displacement or traction is established for energy consistency between micro and macrostruc-

tures. First, the microscopic boundary value problem is defined. In the absence of body forces, the RVE dynamic equilibrium at any point is expressed as:

$$\frac{\partial}{\partial x}\,\sigma_{\mathrm{m}} - \dot{p}_{\mathrm{m}} = 0 \tag{3.1}$$

where σ_{m} is the microscale stress and p_{m} is the microscale linear momentum which are given by the following equations

$$p_{\mathrm{m}} = \rho_{\mathrm{m}}\,\dot{u}_{\mathrm{m}} \tag{3.2}$$

$$\sigma_{\mathrm{m}} = E_{\mathrm{m}}\,\varepsilon_{\mathrm{m}} \tag{3.3}$$

where ρ_{m} and E_{m} are the microstructural mass density and Young's modulus, respectively. The microstructural boundary value problem is solved for each RVE. The material behaviour is determined by the obtained kinematic quantities, the microscopic velocity $\dot{u}_{\mathrm{m}}$, a dot indicates the derivative of displacement u_{m} with respect to time, and the microscopic strain ε_{m}. In statics, for the micro-macro relations, the total variation of work on the macro-level is equal to the volume average of the variation of work on the micro-level, which is given by [25]

$$\sigma_{\mathrm{M}}\,\varepsilon_{\mathrm{M}} = \frac{1}{V_{\mathrm{m}}}\int\limits_{V_{\mathrm{m}}} \sigma_{\mathrm{m}}\,\varepsilon_{\mathrm{m}}\,\mathrm{d}V_{\mathrm{m}} \tag{3.4}$$

where σ_{M} and ε_{M} are macroscopic stress and strain, respectively, and V_{m} is the volume of the microstructure. The macro deformation tensor ε_{M} can be linked in the associated RVE to the position $x_{\mathrm{i}} = \varepsilon_{\mathrm{M}} x_{\,0\mathrm{i}}$. Here, i and $x_{0\mathrm{i}}$ represents any point and initial position in the RVE, respectively. This shows how the macroscale quantities can be obtained by the integration of micro kinematic quantities in the RVE. Consequently, the macro stress σ_{M} and the macro strain ε_{M} can be obtained by decomposing Eq. (3.4), presented as the volume-averages of the microscale quantities

$$\langle \sigma_{\mathrm{m}} \rangle_x = \frac{1}{V_{\mathrm{m}}}\int\limits_{V_{\mathrm{m}}} \sigma_{\mathrm{m}}\,\mathrm{d}V_{\mathrm{m}} \tag{3.5}$$

$$\langle \varepsilon_{\mathrm{m}} \rangle_x = \frac{1}{V_{\mathrm{m}}}\int\limits_{V_{\mathrm{m}}} \varepsilon_{\mathrm{m}}\,\mathrm{d}V_{\mathrm{m}} \tag{3.6}$$

where $\langle\cdot\rangle_x$ denotes the spatial averaging operator implied by the previous two expressions. Upscaling, a transition from micro to macroscale, is implemented based on the Hill-Mandel Principle in order to transfer both static and dynamic features of heterogeneity to a macro-level. Namely, inertia effects on the micro-level are transferred alongside the stresses to the macro-level through upscaling, so dynamic effects on macro-level are generated depending on the microstructure. In addition to the work of strain, the work of acceleration is added into the variation of work performed on both scales so that the Hill-Mandel condition in

dynamics is written as [25]

$$\sigma_{\mathrm{M}}\,\delta\varepsilon_{\mathrm{M}} + \frac{d}{dt}p_{\mathrm{M}}\,\delta u_{\mathrm{M}} = \frac{1}{V_{\mathrm{m}}}\int\limits_{V_{\mathrm{m}}} \sigma_{\mathrm{m}}\,\delta\varepsilon_{\mathrm{m}}\,\mathrm{d}V_{\mathrm{m}} + \frac{1}{V_{\mathrm{m}}}\int\limits_{V_{\mathrm{m}}} \frac{d}{dt}p_{\mathrm{m}}\,\delta u_{\mathrm{m}}\,\mathrm{d}V_{\mathrm{m}} \tag{3.7}$$

where p_{m} and p_{M} are microscopic and macroscopic momentum, respectively. Upscaling relations can be obtained from Eq.(3.7). The averaged momentum and velocity by microscopic quantities can be written as

$$\langle p_{\mathrm{m}}\rangle_x = \frac{1}{V_{\mathrm{m}}}\int\limits_{V_{\mathrm{m}}} p_{\mathrm{m}}\,\mathrm{d}V_{\mathrm{m}} \tag{3.8}$$

$$\langle v_{\mathrm{m}}\rangle_x = \frac{1}{V_{\mathrm{m}}}\int\limits_{V_{\mathrm{m}}} v_{\mathrm{m}}\,\mathrm{d}V_{\mathrm{m}} \tag{3.9}$$

3.3 Time averaging

In this section, the time averaging will be added to develop the dynamic energy averaging relation. The space averaging in micro-to-macro transition is extended to account for the time averaging. This transition requires the application of an additional time-dependent averaging, which can be considered as an extended version of the Hill-Mandel Principle. Apart from the effect of spatial variability in the microstructure, the time averaging comprises the time history of the wave propagation through the microstructure. Thus, time and history-dependent stress-strain and momentum-velocity relationships are both transferred to the macro-level to improve the accuracy and reliability of the homogenised material behaviour. The suggested procedure is to extend the coupling between micro and macro scales by integrating the Hill-Mandel Principle in time, that is

$$\sigma_{\mathrm{M}}\delta\varepsilon_{\mathrm{M}} + \frac{d}{dt}p_{\mathrm{M}}\delta u_{\mathrm{M}} = \frac{1}{T_{\mathrm{m}}}\frac{1}{V_{\mathrm{m}}}\int\limits_{t_0}^{t_f}\int\limits_{V_{\mathrm{m}}} \sigma_{\mathrm{m}}\delta\varepsilon_{\mathrm{m}}\,\mathrm{d}V_{\mathrm{m}}\mathrm{d}t_{\mathrm{m}} + \frac{1}{T_{\mathrm{m}}}\frac{1}{V_{\mathrm{m}}}\int\limits_{t_0}^{t_f}\int\limits_{V_{\mathrm{m}}} \frac{d}{dt}p_{\mathrm{m}}\delta u_{\mathrm{m}}\,\mathrm{d}V_{\mathrm{m}}\mathrm{d}t_{\mathrm{m}} \tag{3.10}$$

where $T_{\mathrm{m}} \equiv t_f - t_0$ is the time period of total propagation of a wave on the micro level and t_0 is the initial time, t_f is the final time. Analogous to space averaging, the time averaged quantities can be obtained from Eq. (3.10) as

$$\langle\langle\sigma_{\mathrm{m}}\rangle_x\rangle_t = \frac{1}{T_{\mathrm{m}}}\frac{1}{V_{\mathrm{m}}}\int\limits_{t_0}^{t_f}\int\limits_{V_{\mathrm{m}}} \sigma_{\mathrm{m}}\,\mathrm{d}V_{\mathrm{m}}\,\mathrm{d}t_{\mathrm{m}} \tag{3.11}$$

$$\langle\langle\varepsilon_{\mathrm{m}}\rangle_x\rangle_t = \frac{1}{T_{\mathrm{m}}}\frac{1}{V_{\mathrm{m}}}\int\limits_{t_0}^{t_f}\int\limits_{V_{\mathrm{m}}} \varepsilon_m\,\mathrm{d}V_{\mathrm{m}}\,\mathrm{d}t_{\mathrm{m}} \tag{3.12}$$

$$\langle\langle p_{\mathrm{m}}\rangle_x\rangle_t = \frac{1}{T_{\mathrm{m}}}\frac{1}{V_{\mathrm{m}}}\int_{t_0}^{t_f}\int_{V_{\mathrm{m}}} p_{\mathrm{m}}\,\mathrm{d}V_{\mathrm{m}}\,\mathrm{d}t_{\mathrm{m}} \tag{3.13}$$

$$\langle\langle v_{\mathrm{m}}\rangle_x\rangle_t = \frac{1}{T_{\mathrm{m}}}\frac{1}{V_{\mathrm{m}}}\int_{t_0}^{t_f}\int_{V_{\mathrm{m}}} v_{\mathrm{m}}\,\mathrm{d}V_{\mathrm{m}}\,\mathrm{d}t_{\mathrm{m}} \tag{3.14}$$

where $\langle\cdot\rangle_t$ denotes the temporal averaging operator and $\langle\langle\sigma_{\mathrm{m}}\rangle_x\rangle_t$, $\langle\langle\varepsilon_{\mathrm{m}}\rangle_x\rangle_t$, $\langle\langle p_{\mathrm{m}}\rangle_x\rangle_t$, and $\langle\langle v_{\mathrm{m}}\rangle_x\rangle_t$ are the space and time averaged stress, strain, momentum and velocity, respectively. As a result of the space-time averaged stress-strain and momentum-velocity relationships, the transition material parameters for the macro-level are given by

$$E_{\mathrm{M}} = \langle\langle\sigma_{\mathrm{m}}\rangle_x\rangle_t / \langle\langle\varepsilon_{\mathrm{m}}\rangle_x\rangle_t \tag{3.15}$$

$$\rho_{\mathrm{M}} = \langle\langle p_{\mathrm{m}}\rangle_x\rangle_t / \langle\langle v_{\mathrm{m}}\rangle_x\rangle_t \tag{3.16}$$

where E_{M} and ρ_{M} are the time-space averaged Young's modulus and mass density on the macro level, respectively. The micro-macro averaging model is employed for each macroscopic integration point to describe the homogenised macroscopic behaviour underlying microscopic heterogeneous behaviour.

The micro-macro averaging model has been verified not to be affected by the order of averaging since all processes implemented in the method are linear. Although not shown in this thesis, the macroscale parameters obtained using first the space averaging and then the time averaging were found to be the same as the parameters obtained in the opposite order of averaging operations. In this thesis, the former order is employed in the numerical examples.

3.4 Numerical results

Several numerical examples are presented to assess the convergence of the microstructure size in which spatial and temporal fluctuations do not appear and the macroscopic response can be approximated by the averaged microscopic response. The macroscopic response of a one-dimensional laminate bar shown in Figure 3.2 is investigated under various loading and boundary conditions. The bar is restrained at the left end and subjected to several loading conditions at the other end (e.g. constant and harmonic loads). The finite element model consists of periodic unit cells, each discretized with four linear elements with length h. The bar length varies based on the number of unit cells, which each have length of 1 m and cross-sectional area of 1 m^2. The central difference method for time integration is used with a time step size of 0.1 s. As for the time window T_m, each simulation time varies depending on the number of wave propagations as well as the time required a wave reach to the end of a bar.

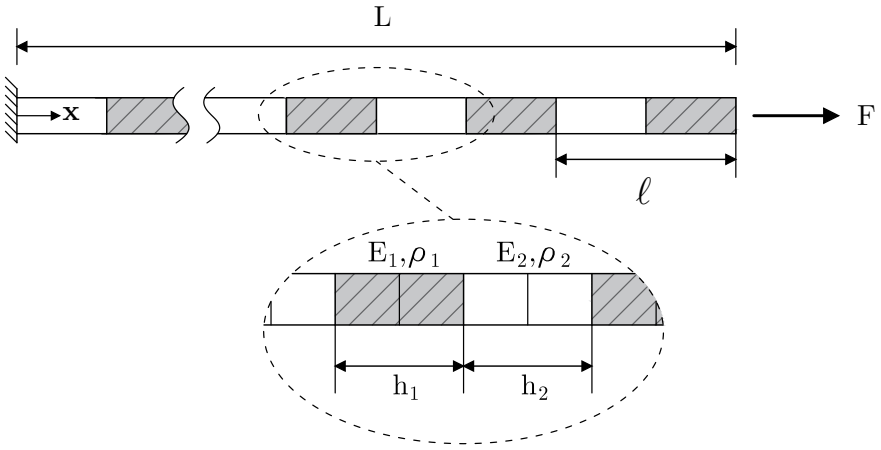

Fig. 3.2 A laminate bar

A unit cell consist of two layers, the constitutive parameters of which are Young's modulus E_1 and E_2, mass densities ρ_1 and ρ_2, elastic impedances $z_1 = \sqrt{E_1\rho_1}$ and $z_2 = \sqrt{E_2\rho_2}$, and wave speeds $c_1 = \sqrt{E_1/\rho_1}$ and $c_2 = \sqrt{E_2/\rho_2}$. For simplicity, equal volume fractions of the two materials are chosen is $\alpha = 0.5$, so that $h_1 = h_2 = \frac{1}{2}\ell$. While the material properties of two laminate elements are chosen for three levels of the impedance contrast $z_1/z_2 = 10$, $z_1/z_2 = 100$ and $z_1/z_2 = 1000$, the wave speeds are kept the same between the components of laminate $c_1 = c_2 = 1$ m/s.

In the numerical examples, the RVE is determined by user defined parameters, which are the number of unit cells N_{uc} and the number of wave propagations N_{wp}. For the laminate bar, the RVE size is equivalent to the bar length selected as N_{uc} times ℓ. Moreover, the laminate bar is loaded for duration t_f, where t_f is found by dividing the bar length by the wave speed, times a factor N_{wp}. At time $t = t_f$, the stresses, strains, velocities and momentum values are sampled and averaged in space and time. Then, E_{M} is obtained by dividing stresses over strains, while ρ_{M} is obtained by dividing momentums over velocities. The macroscopic material properties are validated against the analytical exact solutions of the effective Young's modulus E_{avr} and the effective mass density ρ_{avr} obtained for periodic composites [94, 95] as follows

$$E_{\text{avr}} = \frac{E_1 E_2}{(1-\alpha)E_1 + \alpha E_2} \tag{3.17}$$

$$\rho_{\text{avr}} = \alpha\rho_1 + (1-\alpha)\rho_2 \tag{3.18}$$

where $0 \leq \alpha \leq 1$.

3.4.1 Effect of boundary conditions

In order to establish appropriate boundary requirements for the space-time averaging model, we firstly adopt Dirichlet conditions via the direct imposition method. Alternatively, and following earlier findings in statics [30, 59, 96], periodic boundary conditions are studied, which are here imposed using the so-called bipenalty method (see the Appendix for details). In Figure 3.3, the results obtained with the two sets of boundary conditions are compared. It can be verified that the use of periodic boundary conditions has particular advantages in the determination of the averaged mass density. Therefore, in the remainder of the paper periodic boundary conditions will be used.

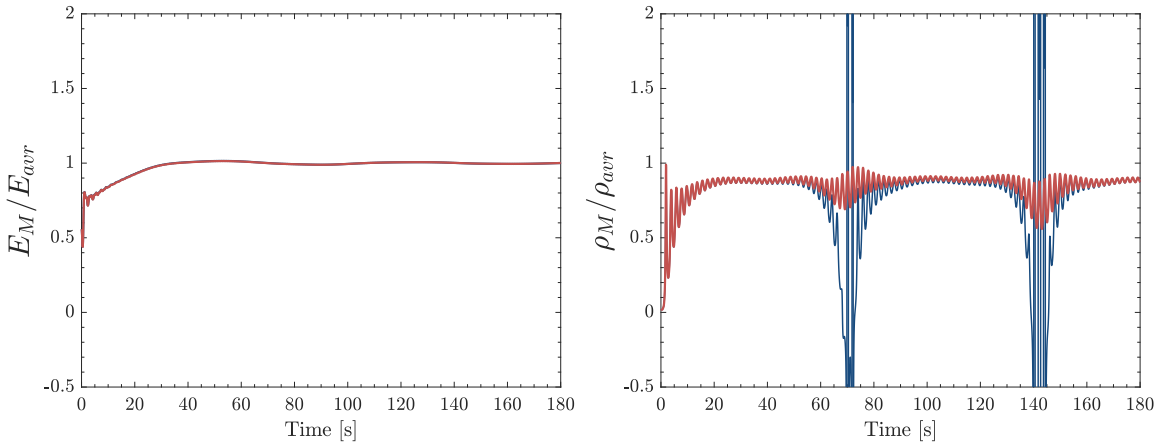

Fig. 3.3 Space-time averaging results of normalised averaged Young's modulus E_M/E_{avr} (left) and normalised averaged mass density ρ_M/ρ_{avr} (right). Comparisons between Dirichlet condition (blue line) and periodic boundary condition (red line) for the bar with material impedance contrast $z_1/z_2 = 100$ and constant excitation.

3.4.2 Effect of time-averaging

The present study evaluates the effectiveness of the space-time averaging method. To achieve this objective, we compare the averaged results of Young's modulus and mass density obtained by both space-time averaging and space averaging. To obtain the averaged material properties, a one-dimensional periodic laminated bar shown in Figure 3.2, which enables comparisons with exact analytical solutions, is investigated under harmonic excitation with periodic boundary conditions, for the material contrast of $z_1/z_2 = 10$. The results of averaged Young's modulus and mass density, are normalized by the analytical values given in Eqs. (3.17) and (3.18), respectively.

As shown in Figure 3.4, the results of the space-time averaged material properties (i.e. $\langle\langle E_m\rangle_x\rangle_t$ and $\langle\langle \rho_m\rangle_x\rangle_t$) converge to those obtained by the analytical equivalents (i.e. E_{avr} and ρ_{avr}). Although the normalised macroscopic Young's modulus results obtained by the

space averaging approach are reasonably accurate, those obtained by the space-time averaging approach converge considerably quicker and are fully consistent with the analytically averaged Young's modulus. On the other hand, the space averaging approach provides a poor estimation of the macroscopic mass density over time. Therefore, for dynamic multiscale problems, the use of space averaging may not be adequate. The space-time averaging approach generates reliable results for the macroscopic mass density as well as the macroscopic Young's modulus.

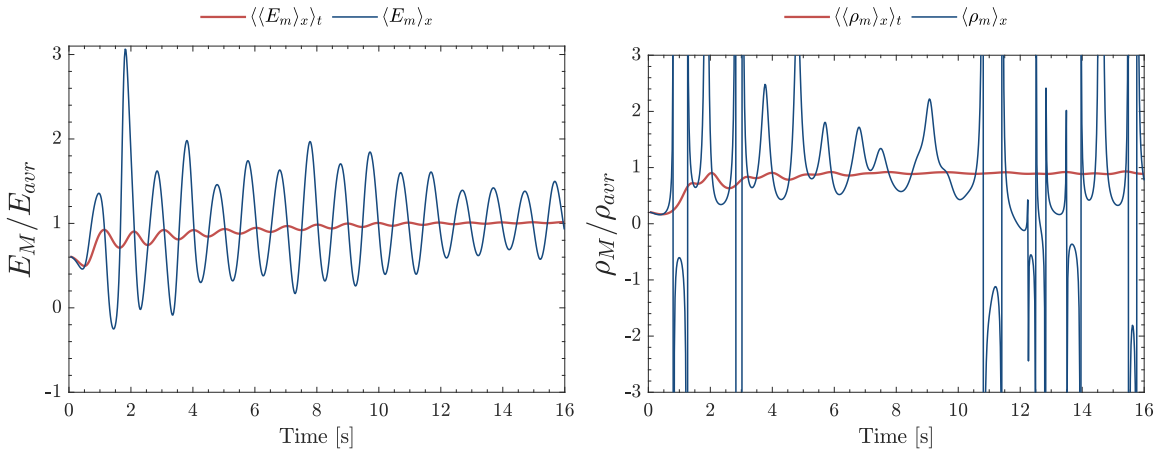

Fig. 3.4 Comparison of space and space-time averaging for normalised averaged Young's modulus E/E_{avr} (left) and normalised averaged mass density ρ/ρ_{avr} (right) where material impedance is $z_1/z_2 = 10$ subjected to harmonic excitation with periodic boundary conditions.

3.4.3 Effect of number of unit cells and number of wave propagations

With the superiority of periodic boundary conditions and space-time averaging established, the influence of number of unit cells N_{uc} and wave propagations N_{wp} along the bar on the averaged Young's modulus and averaged mass density can be investigated next. Most of the results converge progressively with increase in the number of unit cells and an ongoing propagation of the wave. While Figure 3.5 shows the convergence of averaged Young's modulus, Figure 3.6 shows mass density parameters in space and time, respectively. This analysis allows to find the best combination of those parameters since the computational effort required for doubling the number of unit cells is the same order of magnitude as for doubling the number of wave propagations.

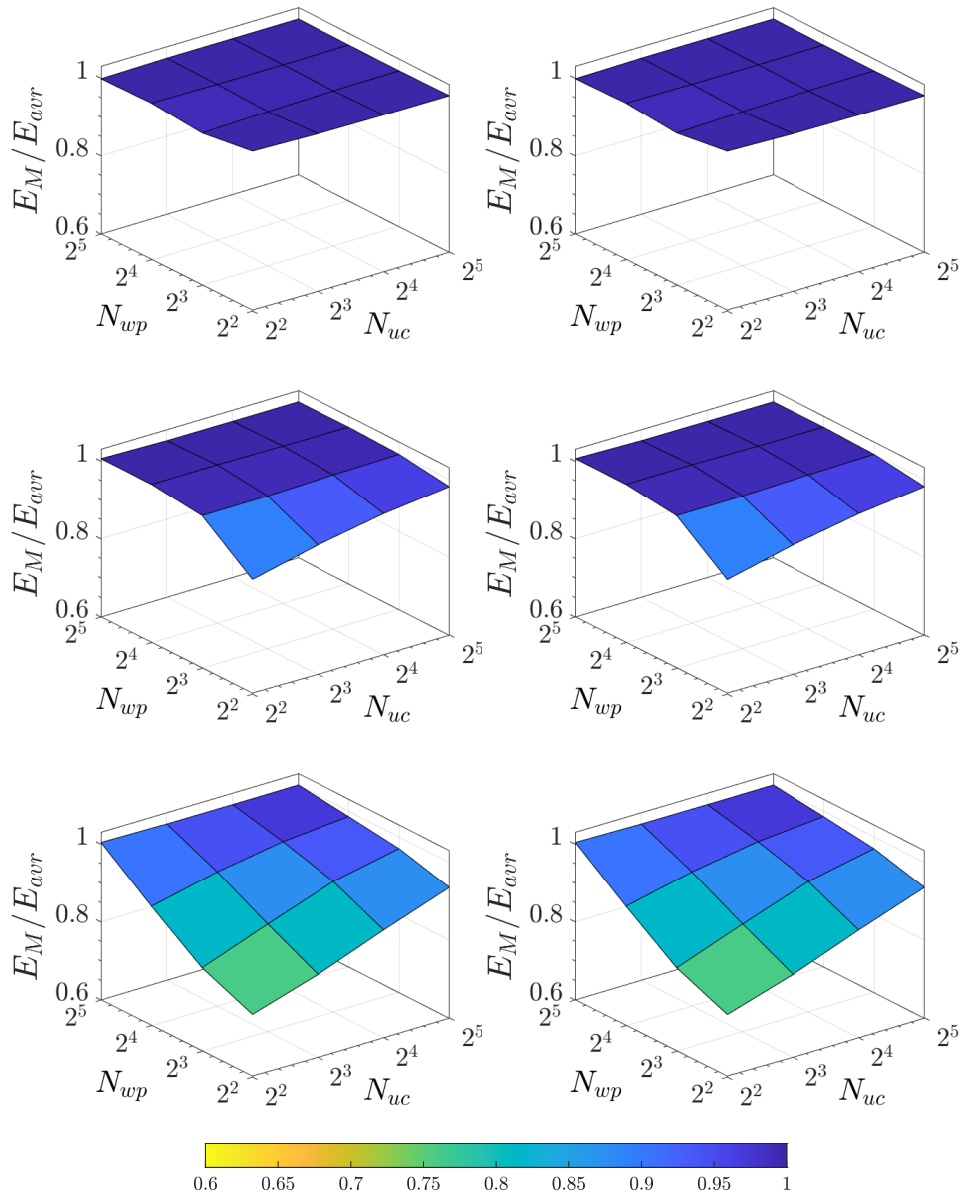

Fig. 3.5 Normalised averaged Young's modulus $E_{\mathrm{M}}/E_{\mathrm{avr}}$ versus number of unit cells N_{uc} and number of wave propagations N_{wp} where material impedances are $z_1/z_2 = 10$ (top row), $z_1/z_2 = 100$ (middle row) and $z_1/z_2 = 1000$ (bottom row) subjected to constant (left column) and harmonic (right column) excitations with periodic boundary conditions.

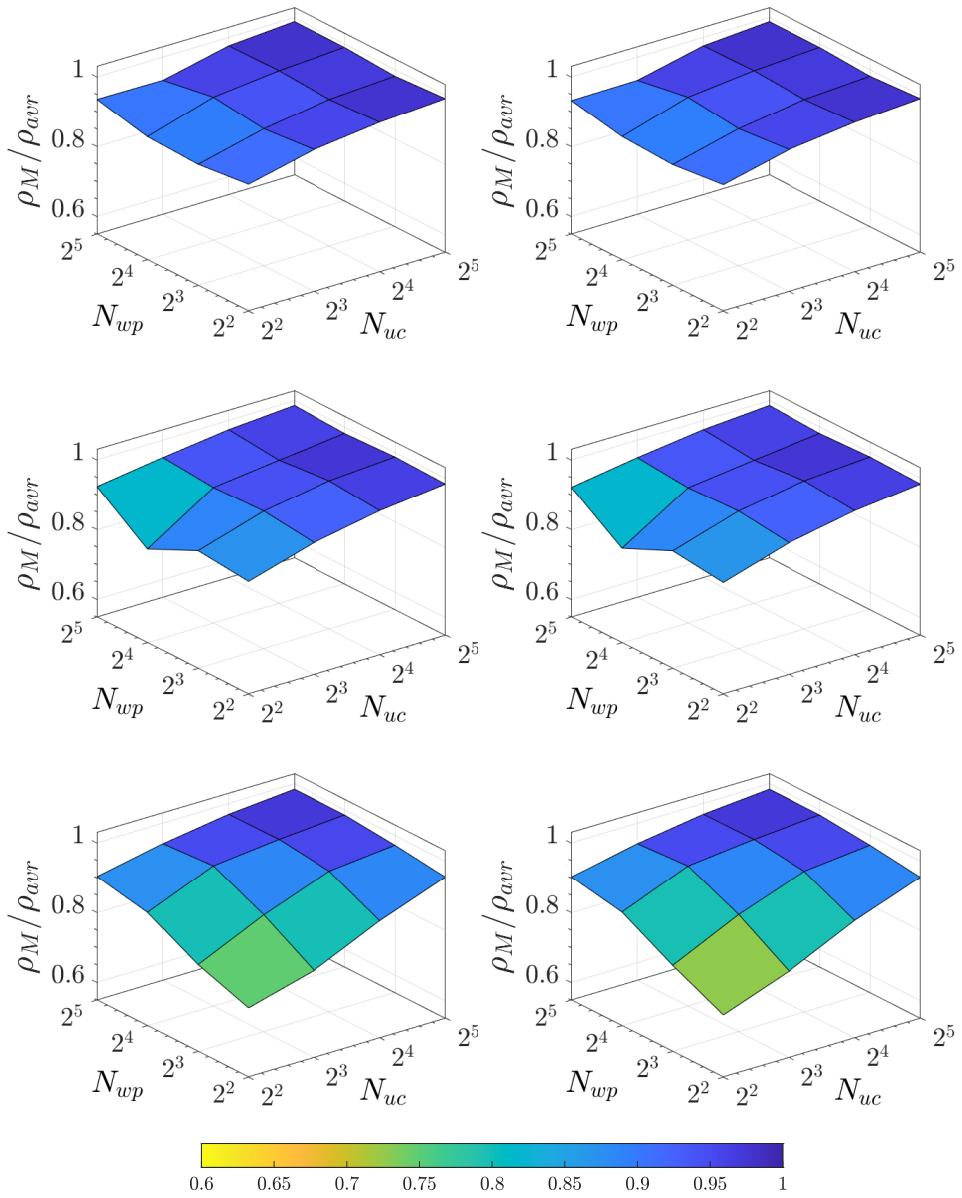

Fig. 3.6 Normalised averaged mass density $\rho_{\mathrm{M}}/\rho_{\mathrm{avr}}$ versus number of unit cells N_{uc} and number of wave propagations N_{wp} where material impedances are $z_1/z_2 = 10$ (top row), $z_1/z_2 = 100$ (middle row) and $z_1/z_2 = 1000$ (bottom row) subjected to constant (left column) and harmonic (right column) excitations with periodic boundary conditions.

The normalised results of Young's modulus shown in Figure 3.5 converge with increasing N_{uc} and N_{wp}. The overriding observation is that a sufficient number of unit cells *as well as* a sufficient number of wave propagations is required to obtain accurate estimates for the macroscale material parameters.

Furthermore, the obtained space-time averaging results of Young's modulus and mass density do not appear to depend on the particular loading conditions, e.g. constant and harmonic loading conditions. As can be seen in Figure 3.6, at the higher level impedance contrast, the results under constant load converge slightly quicker compared to harmonic load, but the overriding observation is that the influence of loading condition is relatively minor.

3.4.4 Material parameter studies

Next, the numerical examples assess the influence of variations in impedance contrasts between laminate components to ensure the robustness of the space-time averaging method. As can be seen in Figures 3.5 and 3.6, accurate estimates of the macroscale material properties can still be obtained for increased impedance contrasts. Particularly, but not surprisingly, the averaged Young's modulus and mass density at the low-levels of impedance contrasts converge quicker than those at the medium and/or high-level impedance contrasts. Especially at higher levels of impedance contrasts, the most efficient approach is to aim simultaneously for a higher number of unit cells as well as a higher number of wave propagations to obtain accurate estimates for the macroscale parameters.

The influence of different volume fractions on the number of unit cells and wave propagations required to obtain converged macroscopic Young's modulus and mass density is investigated next. The bar is subjected to harmonic excitation with periodic boundary conditions, and the highest-level of impedance contrasts $z_1/z_2 = 1000$ in the material is considered. The volume fraction of the first component of the microscopic unit cell α is varied from 10% to 90%, while the macroscopic material parameters are estimated by simultaneously increasing the number of unit cells and wave propagations. For the wide range of volume fractions in the material, the macroscopic Young's modulus E_{M} and mass density ρ_{M} demonstrate good convergence with those obtained analytically at $N_{\mathrm{uc}} = N_{\mathrm{wp}} = 2^4$. The convergence performance of the macroscopic Young's modulus for the higher volume fractions of the first laminate is slower than that for the lower volume fractions, whereas the convergence performance of the macroscopic mass density for the higher volume fractions of the first laminate is faster than for lower volume fractions.

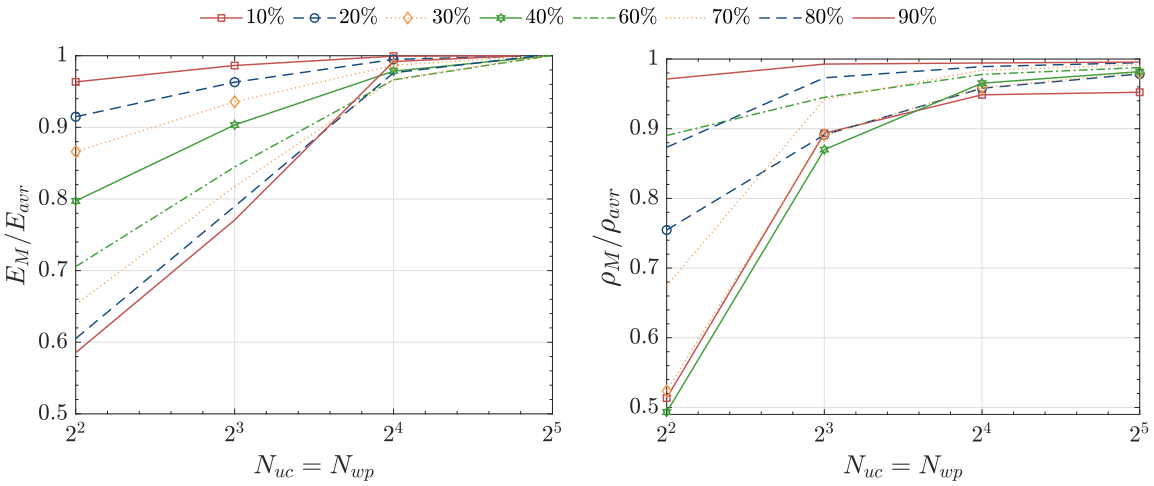

Fig. 3.7 Various volume fractions of components of periodic composites for normalised averaged Young's modulus $E_{\mathrm{M}}/E_{\mathrm{avr}}$ (left) and normalised averaged mass density $\rho_{\mathrm{M}}/\rho_{\mathrm{avr}}$ (right) where material impedance contrast is $z_1/z_2 = 1000$ subjected to harmonic excitation with periodic boundary conditions versus the same number of unit cells N_{uc} and wave propagations N_{wp}.

3.5 Discussion

In this work, a new space-time averaging model between micro and macrostructure has been developed to obtain accurate estimates of macroscopic material properties for elastodynamic multiscale problems. In this context, the Hill-Mandel Principle is extended to include the effect of the time history on microstructure in addition to spatial heterogeneity. Therefore, in addition to the standard format of volume averaging, the time averaging leads to enhanced averaging relations between micro- and macrostructure.

To evaluate the validity of this averaging model, the response of the one-dimensional laminated bar with low, medium and high level impedance contrasts is investigated when subjected to several loading/boundary conditions. In particular, the averaged material parameters are analysed with the size of the microstructure and the time period of propagation of a longitudinal wave. Accordingly, this present model can be used to determine suitable RVE sizes in dynamic for averaging problems. Whereas the results in the high level of impedance contrast is found to require larger RVE sizes and longer runtimes, the results for a low level of impedance contrast converge much quicker - implying smaller RVE sizes and shorter runtimes. The numerical examples illustrate that a larger RVE size with shorter runtime can compensate for smaller RVE sizes with a longer runtime, and vice versa.

Chapter 4

Spatial and Temporal Transitions in Computational Homogenisation

Building upon the progress in the accuracy of the homogenised material properties in Chapter 3, the methodology of the representative volume element (RVE) for multiscale dynamic problems from Chapter 3 is integrated into the dynamic computational homogenisation method to improve scale transitions between the macro and microscales. This chapter presents a newly proposed approach which separates length and time scales simultaneously for the dynamic RVE, thereby enhancing the accuracy of the macroscopic response.

4.1 Introduction

Modelling the mechanical behaviour of periodic composites with engineered microstructure has gained importance due to their use in advanced engineering applications. The requirement of modelling complex microstructural properties in materials can robustly be solved by the direct numerical simulation (DNS), yet this method causes extensive computational effort due to the high demand for numerical calculations. Homogenisation methods enable the modelling of the microstructural mechanical and physical behaviour for composites to be more computationally efficient. Homogenisation methods cannot capture the modelling of many nonlinear problems such as localisation and discontinuities (e.g. the diverse geometrical and physical configurations of microstructures) since the conventional homogenisation methods have been developed for elastic materials and their extension towards problems that violate basic assumptions of elasticity is not straightforward.

Computational homogenisation has become prominent as an effective tool within multi-scale methods to overcome these problems by modelling the complex mechanical behaviour of materials at different scales [52, 97]. The classic computational homogenisation method contains two (or possibly more) coupled and nested boundary value problems in which the macroscopic analysis cooperates with the microscopic analysis in defining the constitutive behaviour [98]. Namely, the macroscopic constitutive behaviour is adopted by the solution of the associated microstructural problem implemented over typically a representative volume element (RVE) through successive transitions between macro and microscales. Scale transitions enable exchanging information, which includes the macroscopic kinematic relations establishing the microstructural problem and averaging relations in accordance with energy conservation between the scales. The transition of kinematic relations from macroscopic to microscopic scales is defined as downscaling. Conversely, in the opposite direction, the transition of averaging relations is defined as upscaling.

Scale transitions are performed based on the principle of separation of scales on which the computational homogenisation method is based. In cases where the separation of scales cannot be clearly identified, the characteristics of a microscopic wave become significant due to consecutive wave reflections and fractions (i.e. dispersion), leading to the transient behaviour of microstructures in dynamics. The dynamic response of the microstructure (i.e. micro-inertia effects) require the consideration of the scale of microstructure fluctuations. In this case, the classic computational homogenisation method is incapable of capturing the transient response on the microscale. Accordingly, an extension of the computational homogenisation method is used for periodic composites with dynamic kinematic and averaging relations to account for these micro-inertia effects [64, 99, 100]. Even though the development of dynamic transition relations achieves the problems emerging from the size

of microstructures, the concept of separation of scales in computational homogenisation methods is not addressed for the transient problems [4].

A computational homogenisation method is developed using finite element discretisation in space and time integration in time where the separation of both length and time scales is adopted. A macrostructure is spatially and temporally coupled with the RVE for scale transition relations between the two scales. The separation of scales principle enables decoupling scale transitions across the scales. As a purpose of this Chapter, a decoupling is presented to overcome the deficiencies in scale transitions emerging from the microstructure in dynamics. The findings in Chapter 3 clarify that accurate estimation of macroscopic material properties in dynamics requires a larger RVE size with a longer time period on the microscale. Furthermore, the improvement in the convergence of the macroscopic material properties with the time averaging presented in Chapter 3 leads to adopting the separation of time scales in the dynamic computational homogenisation method.

In this Chapter, the scale transitions strategy is reformulated by the simultaneous separation of length and time scales. Consequently, the microstructure is decoupled from the associated macrostructure in regard to space and time discretisation on the microscale. The proposed work exploits the benefits of separations of length and scales by increasing the RVE size as well as the time period on the microscale to obtain satisfactory accuracy in the macroscopic response of a material. Notably, the effects of separation of length and time scales in a dynamic computational homogenisation framework are studied for various material properties and validated against the direct numerical solution results.

4.2 Dynamic computational homogenisation system

The computational homogenisation method establishes stress-strain $\sigma_{\mathrm{M}} - \varepsilon_{\mathrm{M}}$ and momentum-velocity $p_{\mathrm{M}} - \dot{u}_{\mathrm{M}}$ relations between the two scales by averaging the response of the RVEs according to the Hill-Mandel principle through macroscopic integration points to estimate the macroscopic response of periodic composites. This leads to involving a boundary value problem on the macroscale and microscale. The solution of these nested boundary value problems is coupled by scale transition relations as regards energy consistency between the two scales. The macroscopic constitutive behaviour is provided by the solution of the microscopic analysis instead of an analytical constitutive model so that there is no need to make any constitutive assumption on the macroscale. Briefly, the computational homogenisation method schematised in Figure 4.1 consist of three main steps:

- Solution of a macroscopic boundary value problem

- Transfer of solutions between macro and microstructure models
- Solution of a microscopic boundary value problem.

At the macroscale, the bar is subjected to a constant load F at its right end and constrained at its left end. At the microscale, the bar consists of periodic unit cells of length ℓ. The macroscopic material properties are homogenised by the response of the RVE. At the microscale, the material of first laminate component is defined by Young's modulus E_1 and mass density ρ_1, while for the second laminate component, the material properties are denoted as E_2 and ρ_2. The size of laminate components are determined depending on volume fractions, which are h_1 and h_2 for the first and second laminate components, respectively.

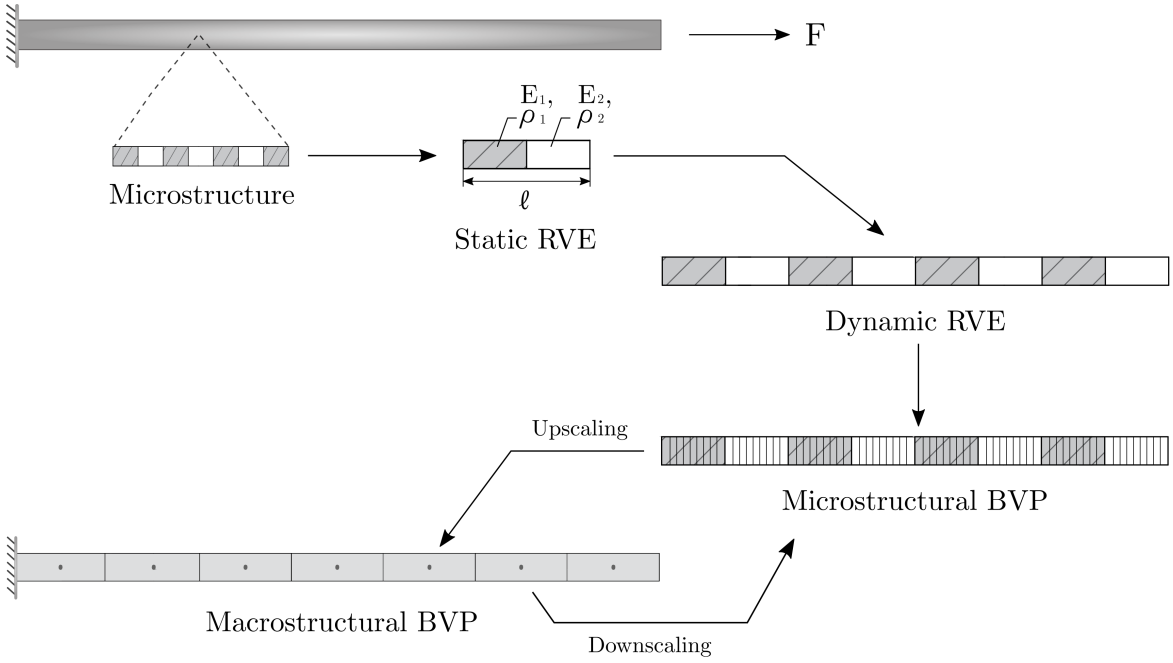

Fig. 4.1 A schematic illustration of the dynamic computational homogenisation method

4.3 Scale separation

In the extended computational homogenisation methods, the scale transitions described in Section 4.6 contain spatial and temporal relations between the macro and microscales. In accordance with this strategy, an extended separation of scales principle is presented in this section by comprising not only the separation of length scales but also the separation of time scales. This section aims to obtain a better estimation of the macroscopic constitutive behaviour of the underlying microstructure response with the improvement of the separation of scales. Accordingly, the macro and microscales are decoupled for the scale transitions,

and the separation of length and time scales presented below is formulated for a dynamic homogenisation method.

4.3.1 Separation of length scales

In homogenisation methods, the principle of separation of length scales assumes that the size of the microstructure ℓ is much smaller than the size of the macrostructure L and the shortest wavelength of the macroscopic response for a given applied load λ_{M} [50]:

$$\ell \ll L \tag{4.1}$$

$$\ell \ll \lambda_{\mathrm{M}} \tag{4.2}$$

In the case of transient problems, the size of the macrostructure L is no longer the sole, dominant macrostructural length scale. Its significance is reduced by the size of the macro-fluctuations ℓ_{M} tending to be considerably small compared to the size of the microstructure ℓ. To tackle these additional length scales, the long wavelength approximation is assumed for the scale separations in homogenisation methods. According to the long wavelength approximation, the size of the microstructure ℓ should be much smaller than the shortest wavelength of the microscopic response for a given applied load λ_{m}. In addition, the size of micro-fluctuations ℓ_{μ} due to the micro-inertia effects must be taken into account and must be smaller than the size of the microstructure ℓ as follows

$$\ell_{\mu} < \ell \ll \ell_{\mathrm{M}} \tag{4.3}$$

$$\ell \ll \lambda_{\mathrm{m}} \tag{4.4}$$

Satisfaction of Expressions (4.1), (4.2), (4.3) and (4.4) ensures that the macroscopic response is independent of the size of the microstructure ℓ. In other words, the macroscopic strain ε_{M} and macroscopic velocity $\dot{u}_{\mathrm{M}}$ are constant over the RVE so that these downscaling parameters can be applied as uniform loads on the boundary of the RVE. Expressions (4.3) and (4.4) become invalid when the scales are inseparable (e.g. larger micro-fluctuations ℓ_{μ}, smaller macro-fluctuations ℓ_{M} and the wavelength of the microscopic response λ_{m}) owing to the design requirements of periodic composites with tailored microstructures, which are

$$\ell_{\mu} \leq \ell \leq \ell_{\mathrm{M}} \tag{4.5}$$

$$\ell \leq \lambda_{\mathrm{m}} \tag{4.6}$$

To obtain a convergent macroscopic response by dealing with inseparable scale inequalities, the spatial coupling between macro and microstructures is resolved by increasing the RVE size L_{m}. The spatial decoupling scheme between the two scales is presented in Figure 4.2 for a one-dimensional periodically laminated bar. The size of the microstructure ℓ is decoupled from the size of the macrostructure L by increasing the number of unit cells N_{uc} at the microscale until obtaining the convergent macroscopic response. Therefore, at the microscale, the size of the RVE L_{m} is directly linked with the size of the microstructure ℓ and the number of unit cells N_{uc}.

As can be seen in Figure 4.2, the size of microscopic unit cell ℓ is kept the same and the length of the bar at the microscale increases with an increase in N_{uc} until the macroscopic response becomes independent of the RVE size L_{m} is given by

$$L_{\mathrm{m}} = N_{\mathrm{uc}}\,\ell \tag{4.7}$$

where L_{m} and ℓ are the size of the dynamic RVE and the size of microscopic unit cell, respectively.

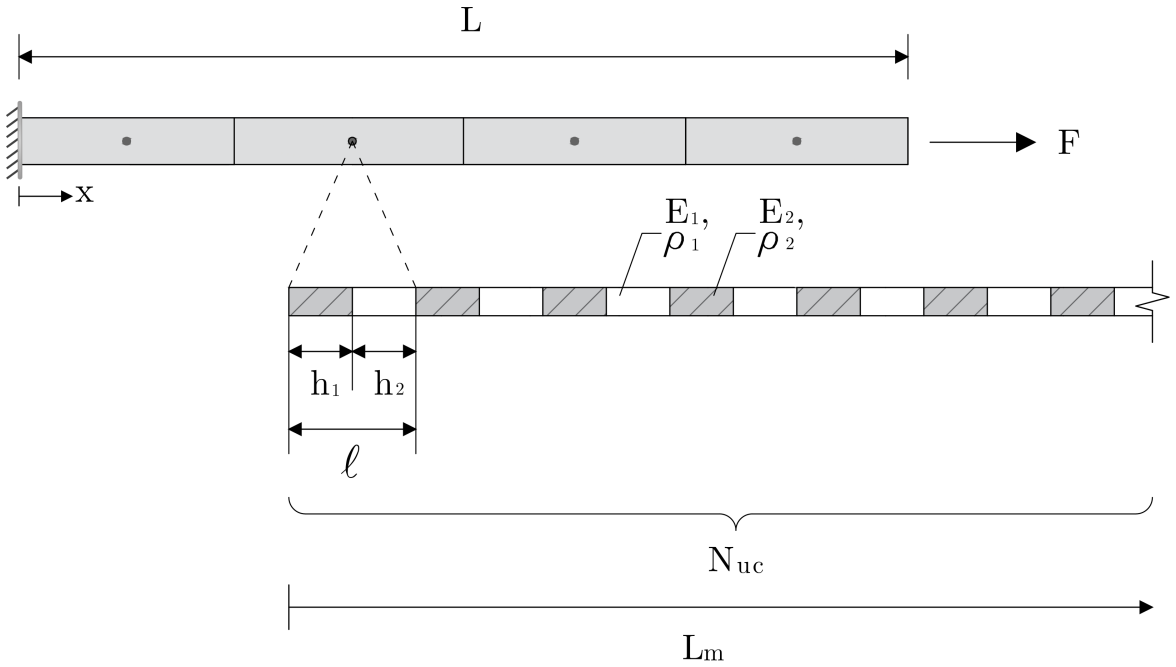

Fig. 4.2 Homogenised macrostructure decoupled spatially with laminated microstructure through macroscopic integration point

4.3.2 Separation of time scales

The modelling of transient problems in the computational homogenisation method requires dynamic transition relations (i.e. momentum-velocity $p_{\mathrm{M}} - \dot{u}_{\mathrm{M}}$ coupling in addition to stress-strain $\sigma_{\mathrm{M}} - \varepsilon_{\mathrm{M}}$ coupling). Thus, the shortest wavelength of the microscopic response λ_{m}, the size of the macro-fluctuations ℓ_{M} and the size of the micro-fluctuations ℓ_{μ} become significant according to the long wavelength approximation. The importance of the principle of length scales is that the convergent macroscopic response for transient problems can be obtained by increasing the RVE sizes. In accordance with this, the principle of separation of time scales assumes that a convergent macroscopic response can also be obtained by longer time periods of the microscopic analysis so that a microscopic wave propagates during a large enough time window over the RVE to average the variations of the microscopic response (e.g. micro-fluctuations and micro-inertia effects). Thus, the temporal coupling between the macro and microscales is controlled by increasing the microstructure time window T_{m}.

In the extended computational homogenisation method, dynamic kinematic and averaging relations are not only coupled between the macro and microscales, but time integration parameters such as the microscopic simulation time $t_{\mathrm{m}}^{\mathrm{f}}$ and the macroscopic time step Δt_{M} are also coupled to build a temporal relation between the two scales as shown in Figure 4.3. The microscopic simulation time $t_{\mathrm{m}}^{\mathrm{f}}$ equals the macroscopic time step Δt_{M} on the account of the temporal coupling between the microscopic and the associated macroscopic time integrations. To illustrate, downscaling parameters are transferred from the macroscale at the current macroscopic time $t_{\mathrm{M}}^{\mathrm{n}}$ with the macroscopic time step Δt_{M} used as the microscopic simulation time $t_{\mathrm{m}}^{\mathrm{f}}$. After performing the microscopic analysis, upscaling parameters are transferred back to the macroscale at the next macroscopic time $t_{\mathrm{M}}^{\mathrm{n+1}}$.

As an alternative, similar to the separation of length scales, the microscopic time integration can also be performed *independently* from the macroscopic time integration to allow a large enough microscopic time window to include the variations of the microscopic response. The principle of the separation of time scales enables the macroscopic time step Δt_{M} to be decoupled from the microscopic simulation time $t_{\mathrm{m}}^{\mathrm{f}}$. The temporal decoupling is presented in Figure 4.4 between the two scales in order to ensure the macroscopic response not to be affected by the the microscopic simulation time $t_{\mathrm{m}}^{\mathrm{f}}$. A more relaxed relation is built depending on the time requiring the microscopic wave to propagate across the RVE t_{m}^{λ}. Therefore, the microstructure time window T_{m} is directly linked with the microscopic time interval t_{m}^{λ} to ensure the microscopic wave experience the variations in the RVE. Thus, the time window of the microscopic analysis T_{m} is determined by the number of wave propagations N_{wp} over the RVE as follows

$$T_{\mathrm{m}} = N_{\mathrm{wp}}\, t_{\mathrm{m}}^{\lambda} \tag{4.8}$$

where t_{m}^{λ} is the microscopic time interval. The number of wave propagations N_{wp} increases to extend the microstructure time window T_{m} until the macroscopic response is not affected by the variations of the microscopic response.

4.4 Macroscopic boundary value problem

To model the dynamic response of one-dimensional linear elastic laminated bar using computational homogenisation, the macroscopic boundary value problem is formulated by the linear balance of momentum with the body forces as follows

$$\frac{\partial}{\partial x}\,\sigma_{\mathrm{M}} - \dot{p}_{\mathrm{M}} = f_{\mathrm{ext}} \tag{4.9}$$

where σ_{M} and $\dot{p}_{\mathrm{M}}$ are the macroscopic stress and the macroscopic momentum, respectively.

The macroscopic relations linking $\dot{u}_{\mathrm{M}}$ and ε_{M} with p_{M} and σ_{M}, respectively, are required at the macroscale to solve the macroscopic boundary problem defined by Eq. (4.9). In the computational homogenisation method, there is no need to assume a constitutive model at the macroscale since the macroscopic constitutive relations are determined by averaging the results of a microscale boundary value problem. The averaged microscopic quantities are transferred to the macroscale through associated macroscopic integration points. The averaged microscopic stress and momentum are embedded as residual forces in the macroscopic boundary value problem through the upscaling procedure. Consequently, the effects of heterogeneity explicitly defined at the microscale are introduced to the constitutive behaviour adopted as a homogeneous at the macroscale.

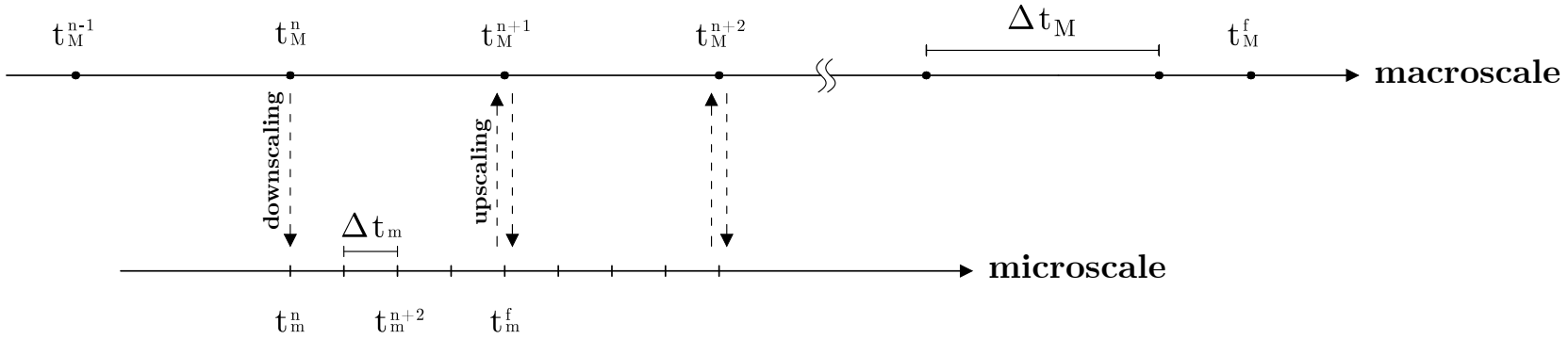

Fig. 4.3 Homogenised macrostructure linked temporally with laminated microstructure through macroscopic integration point

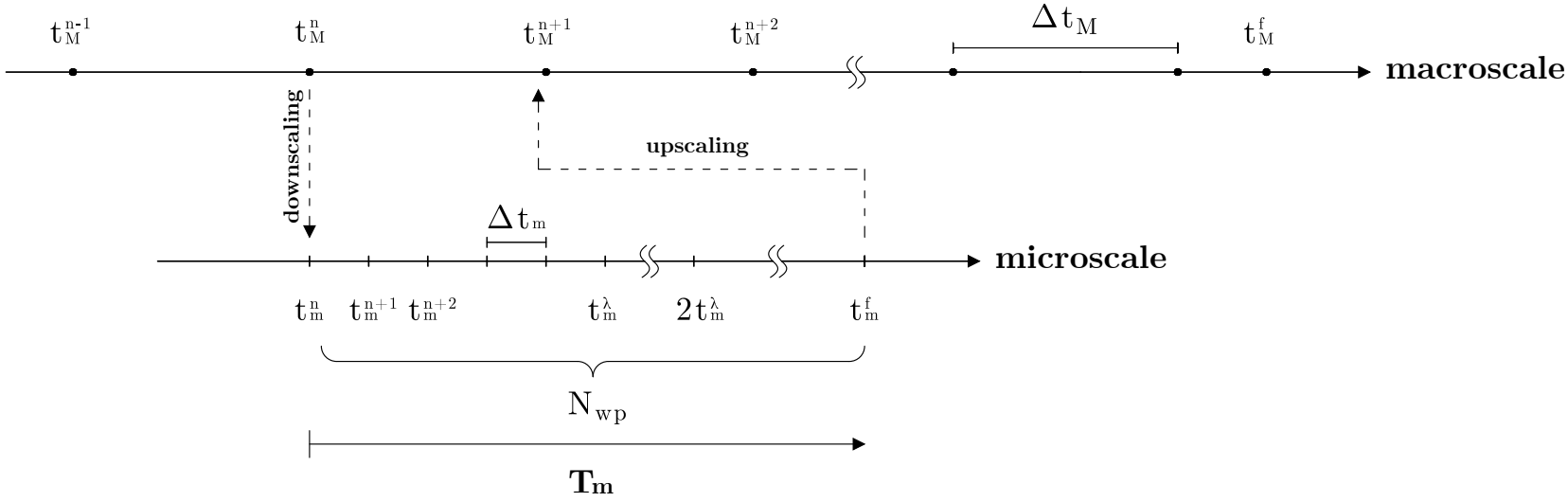

Fig. 4.4 Homogenised macrostructure separated temporally by laminated microstructure

4.5 Microscopic boundary value problem

As representative model of the macrostructure, a one-dimensional periodically laminated microstructural boundary value problem over an RVE is considered for a microstructure assigned to each macroscopic integration point shown in Figure 4.2. The constitutive behaviour of the macrostructure is obtained from the results of the microstructural boundary value problems. The RVE size and the microstructure time window for the microstructural boundary value problem should be taken large enough not to affect the macroscopic response significantly. For transient problems, the RVE size in dynamics is typically larger than one unit cell of periodic composites and the microstructure time window is longer than the macroscopic time step Δt_{M}, see Chapter 3. Accordingly, the separation of length and time scales procedures explained in Sections 4.3.1 and 4.3.2 are performed to determine the RVE size L_{m} and the microstructure time window T_{m} for the microscopic boundary value problem. At the microscale, the selected RVE is solved by the balance of linear momentum with the absence of body forces

$$\frac{\partial}{\partial x}\,\sigma_{\mathrm{m}} - \dot{p}_{\mathrm{m}} = 0 \tag{4.10}$$

where σ_{m} is the microscopic stress and p_{m} is the microscopic linear momentum. In order to solve the microstructural boundary value problems, the constitutive relations at the microscale are defined by constitutive laws, which accounts for heterogeneity in the RVE. Initial and boundary conditions are applied to the RVE through the dynamic kinematic relations via the downscaling procedure described in Section 4.6.1. The macroscopic kinematic quantities (the macroscopic strain ε_{M} and velocity $\dot{u}_{\mathrm{M}}$) are transferred through the macroscopic integration point to the microscale as a prescribed boundary condition.

4.6 Kinematics of the scale transitions

In the computational homogenisation method, the dynamic scale transitions (downscaling - upscaling) construct spatial and temporal relations between the macro and microscales based on conservation of mass, momentum and energy [25, 64]. The downscaling and upscaling procedures are linked with the separation of length and time scales. Namely, the dynamic scale transitions occur at the microstructure time window T_{m} determined by the principle of the separation of time scales. In addition, dynamic scale transitions are performed over the RVE following the principle of the separation of length scales. This section aims the principle of the separation of length and time scales to the downscaling and upscaling procedures.

4.6.1 Downscaling

The solution of the macroscopic boundary value problem provides the macroscopic strain ε_{M} and velocity $\dot{u}_{\mathrm{M}}$ as downscaling parameters for the RVE. The downscaling parameters are formulated as essential boundary conditions for the RVE. The downscaling parameters are used to obtain microscopic momentum from the macroscopic velocity $\dot{u}_{\mathrm{M}}$ as well as microscopic stress from the macroscopic strain ε_{M}. For these purposes, the prescribed boundary condition of the RVE is formulated using Taylor series so that microscopic displacement u_{m} and velocity $\dot{u}_{\mathrm{m}}$ can be related to the macroscopic strain ε_{M} and the macroscopic velocity $\dot{u}_{\mathrm{M}}$ as

$$u_{\mathrm{m}}(x,t) = u_{\mathrm{M}} + \frac{\partial u_{\mathrm{M}}}{\partial x}\,\Delta x_{\mathrm{M}} + \frac{\partial u_{\mathrm{M}}}{\partial t}\,\Delta t_{\mathrm{M}} \tag{4.11}$$

where Δx_{M} is the size of a macroscopic unit cell and Δt_{m} is the macroscopic time step when the dynamic kinematic relations are coupled at the macro and microscales. Rewriting Eq. (4.11) based on the principle of separation of length and time scales explained in Sections (4.3.1) and (4.3.2) gives

$$u_{\mathrm{m}} = u_{\mathrm{M}} + \frac{\partial u_{\mathrm{M}}}{\partial x}\,L_{\mathrm{m}} + \frac{\partial u_{\mathrm{M}}}{\partial t}\,T_{\mathrm{m}} \tag{4.12}$$

where L_{m} and T_{m} is the size of the RVE and the microscopic time window of the microscopic analysis, respectively.

4.6.2 Upscaling

After solving the microscopic boundary value problem, the averaged microscopic stress $\langle\sigma_{\mathrm{m}}\rangle_{\mathrm{x}}$ and the averaged microscopic momentum $\langle p_{\mathrm{m}}\rangle_{\mathrm{x}}$ parameters are transferred to the macro level as upscaling parameters. According to the Hill-Mandel averaging, the microscopic stress and the microscopic momentum are averaged as follows

$$\langle\sigma_{\mathrm{m}}\rangle_{\mathrm{x}} = \frac{1}{L_{\mathrm{m}}}\int_{0}^{L_{\mathrm{m}}} \sigma_{\mathrm{m}}\,\mathrm{d}L_{\mathrm{m}} \tag{4.13}$$

$$\langle p_{\mathrm{m}}\rangle_{\mathrm{x}} = \frac{1}{L_{\mathrm{m}}}\int_{0}^{L_{\mathrm{m}}} p_{\mathrm{m}}\,\mathrm{d}L_{\mathrm{m}} \tag{4.14}$$

where σ_{m} and p_{m} are microscopic stress and momentum, and L_{m} is the RVE size. For each micro time step, the averaged stress $\langle\sigma_{\mathrm{m}}\rangle_{\mathrm{x}}$ and the averaged momentum $\langle p_{\mathrm{m}}\rangle_{\mathrm{x}}$ values are calculated. Once the microscopic time window T_{m} selected based on the separation of time scales procedure is completed at the microscale, the values at the end of the simulation t_{m}^{f} are transferred as residual forces to the macroscale.

$$\sigma_{\mathrm{M}} = \langle\sigma_{\mathrm{m}}(t_{\mathrm{m}}^{f})\rangle_{\mathrm{x}} \tag{4.15}$$

$$p_{\mathrm{M}} = \langle p_{\mathrm{m}}(t_{\mathrm{m}}^{f}) \rangle_{\mathrm{x}} \tag{4.16}$$

4.7 Numerical model implementation

4.7.1 Macroscopic equation of motion in linear problem

In order to solve the macroscopic boundary value problem, Eq. (4.9) is implemented in the finite element method with the implicit time integration scheme. The constant average acceleration is adopted as a variant of Newmark time integration methods, which enables the average of the microscopic stress $\langle \sigma_{\mathrm{m}} \rangle_{\mathrm{x}}$ and momentum $\langle p_{\mathrm{m}} \rangle_{\mathrm{x}}$ to be embedded into the macroscopic boundary value problem as residual forces. Hence, the weak form of Eq. (4.9) is expressed as

$$\int N^{\mathrm{T}} \rho N \,\mathrm{d}x\, \ddot{u}_{\mathrm{M}}^{t+\Delta t} = \int N^{\mathrm{T}} t_{\mathrm{M}} \,\mathrm{d}x\, u_{\mathrm{M}}^{t+\Delta t} - \int B^{\mathrm{T}} E B \,\mathrm{d}x\, u_{\mathrm{M}}^{t+\Delta t} \tag{4.17}$$

where N and B contain interpolation functions and their derivatives, respectively. The macroscopic displacement $u_{\mathrm{M}}^{t+\Delta t}$ and acceleration $\ddot{u}_{\mathrm{M}}^{t+\Delta t}$ can be computed as $u_{\mathrm{M}}^{t} + \Delta u_{\mathrm{M}}$ and $\ddot{u}_{\mathrm{M}}^{t} + \Delta \ddot{u}_{\mathrm{M}}$ to place the average of the microscopic stress and momentum in Eq (4.17). Incorporating the macroscopic displacement Δu_{M} and acceleration $\Delta \ddot{u}_{\mathrm{M}}$ increments into in Eq (4.17) leads to

$$\int N^{\mathrm{T}} \rho N \,\mathrm{d}x\, (\ddot{u}_{\mathrm{M}}^{t} + \Delta \ddot{u}_{\mathrm{M}}) = \int N^{\mathrm{T}} t_{\mathrm{M}} \,\mathrm{d}x\, u_{\mathrm{M}}^{t+\Delta t} - \int B^{\mathrm{T}} E B \,\mathrm{d}x \,\mathrm{d}x\, (u_{\mathrm{M}}^{t} + \Delta u_{\mathrm{M}}) \tag{4.18}$$

The macroscopic acceleration increment $\Delta \ddot{u}_{\mathrm{M}}$ is replaced by the discretised structural Eq. (A.9) using the constant average acceleration method; hence, Eq. (4.18) is rewritten as

$$\begin{aligned} \int N^{\mathrm{T}} \rho N \,\mathrm{d}x\, \ddot{u}_{\mathrm{M}}^{t} + \int N^{\mathrm{T}} \rho N \,\mathrm{d}x \Big[\frac{4}{\Delta t^2} \Big(\Delta u_{\mathrm{M}} - \dot{u}_{\mathrm{M}}^{t} \Delta t - \frac{1}{4} \ddot{u}_{\mathrm{M}}^{t} \Delta t^2 \Big) \Big] = \\ \int N^{\mathrm{T}} t_{\mathrm{M}} \,\mathrm{d}x\, u_{\mathrm{M}}^{t+\Delta t} - \int B^{\mathrm{T}} E B \,\mathrm{d}x\, (u_{\mathrm{M}}^{t} + \Delta u_{\mathrm{M}}) \end{aligned} \tag{4.19}$$

Reorganising Eq. (4.19) for the solution of the macroscopic displacement increment Δu_{M} results in

$$\begin{aligned} \Big[\frac{4}{\Delta t^2} \int N^{\mathrm{T}} \rho N \,\mathrm{d}x + \int B^{\mathrm{T}} E B \,\mathrm{d}x \Big] \Delta u_{\mathrm{M}} = \int N^{\mathrm{T}} t_{\mathrm{M}} \,\mathrm{d}x\, u_{\mathrm{M}}^{t+\Delta t} - \int B^{\mathrm{T}} E B \,\mathrm{d}x\, u_{\mathrm{M}}^{t} \\ + \frac{4}{\Delta t} \int N^{\mathrm{T}} \rho N \,\mathrm{d}x\, \dot{u}_{\mathrm{M}}^{t} + \int N^{\mathrm{T}} \rho N \,\mathrm{d}x\, \ddot{u}_{\mathrm{M}}^{t} \end{aligned} \tag{4.20}$$

The right hand side of Eq. (4.20) is assigned as a residual force $f_{\mathrm{M}}^{\mathrm{res}}$ at the macroscale. The macroscopic residual force is updated by the average of the microscopic stress $\langle\sigma_{\mathrm{m}}\rangle_{\mathrm{x}}$ and momentum $\langle p_{\mathrm{m}}\rangle_{\mathrm{x}}$ for each current macroscopic time $t_{\mathrm{M}}^{\mathrm{n}}$, given by

$$f_{\mathrm{M}}^{\mathrm{res}} = f_{\mathrm{ext}} - f_{\mathrm{M}}^{t}(\sigma) + f_{\mathrm{M}}^{t}(p) + f_{\mathrm{M}}^{t}(\dot{p}) \tag{4.21}$$

where $f_{\mathrm{M}}^{t}(\sigma)$, $f_{\mathrm{M}}^{t}(p)$ and $f_{\mathrm{M}}^{t}(\dot{p})$ are the static, momentum and momentum rate residual forces, respectively. Replacing $f_{\mathrm{M}}^{t}(\sigma)$, $f_{\mathrm{M}}^{t}(p)$ and $f_{\mathrm{M}}^{t}(\dot{p})$ in Eq. (4.21) with the average of the microscopic stress $\langle\sigma_{\mathrm{m}}\rangle_{\mathrm{x}}$ and momentum $\langle p_{\mathrm{m}}\rangle_{\mathrm{x}}$ then leads to the following equations

$$f_{\mathrm{M}}^{t}(\sigma) = \int B^{\mathrm{T}} \langle\sigma_{\mathrm{m}}\rangle_{\mathrm{x}}^{t} = \int B^{\mathrm{T}} \sigma_{\mathrm{M}}^{t} \,\mathrm{d}x \tag{4.22}$$

$$f_{\mathrm{M}}^{t}(p) = \int N^{\mathrm{T}} \langle p_{\mathrm{m}}\rangle_{\mathrm{x}}^{t} = \int N^{\mathrm{T}} p_{\mathrm{M}}^{t} \,\mathrm{d}x \tag{4.23}$$

$$f_{\mathrm{M}}^{t}(\dot{p}) = \int N^{\mathrm{T}} \langle \dot{p}_{\mathrm{m}}\rangle_{\mathrm{x}}^{t} = \int N^{\mathrm{T}} \dot{p}_{\mathrm{M}}^{t} \,\mathrm{d}x \tag{4.24}$$

where $\langle \dot{p}_{\mathrm{m}}\rangle_{\mathrm{x}}^{t}$ is the average of the microscopic momentum rate. As the microscopic stress σ_{m} gives better accuracy than the microscopic momentum rate $\dot{p}_{\mathrm{m}}$, the average of the microscopic momentum rate is replaced by the average of the microscopic stress depending on Eq. (4.10), i.e.

$$f_{\mathrm{M}}^{t}(\dot{p}) = f_{\mathrm{M}}^{t}(\sigma) \tag{4.25}$$

When a standard finite element discretisation is employed for the macrostructural boundary value problem, it is important to use implicit time integration methods due to transferring the heterogeneity of microstructure to the macroscale. In other words, in explicit time integration methods, although the average of the microscopic stress $\langle\sigma_{\mathrm{m}}\rangle_{\mathrm{x}}$ can be transferred and placed as a residual force the average of the microscopic momentum $\langle p_{\mathrm{m}}\rangle_{\mathrm{x}}$ and momentum rate $\langle \dot{p}_{\mathrm{m}}\rangle_{\mathrm{x}}^{t}$ cannot be placed in the discretised structural equation of motion Eq. (A.12). Therefore, for transient problems, explicit time integration methods are not preferable due to the importance of transferring micro-inertia effects via the average of the microscopic momentum $\langle p_{\mathrm{m}}\rangle_{\mathrm{x}}$ and momentum rate $\langle \dot{p}_{\mathrm{m}}\rangle_{\mathrm{x}}^{t}$.

4.7.2 Microscopic equation of motion in linear problem

In order to solve the microscopic boundary value problem, Eq. (4.10) is implemented in a finite element method with implicit and explicit time integration schemes. The constant average acceleration is adopted for the implicit time integration, whereas the central difference scheme is adopted for the explicit time integration. The left and right edge of the RVE are constrained by he downscaling parameters applied as prescribed boundary conditions.

Free and prescribed nodes are denoted by subscripts f and p, respectively. The microscopic displacement u_{m}^{t} and velocity $\dot{u}_{\mathrm{m}}^{t}$ at the current microscopic time step $t_{\mathrm{m}}^{\mathrm{n}}$ are imposed on the prescribed nodes of the RVE as follows

$$u_{\mathrm{p}}^{t} = u_{\mathrm{M}} + \varepsilon_{\mathrm{M}}\, L_{\mathrm{m}} + \dot{u}_{\mathrm{M}} t_{\mathrm{m}}^{\mathrm{n}} \tag{4.26}$$

where the nth microscopic time step $t_{\mathrm{m}}^{\mathrm{n}}$ is given by $t_{\mathrm{m}}^{\mathrm{n}} = n\Delta t_{\mathrm{m}}$. The microscopic time window is given by $T_{\mathrm{m}} = N\Delta t_{\mathrm{m}}$, where N is the total number of microscopic steps. Eq. (4.10) is derived for the time integration schemes in the next Sections to obtain the residual forces with respect to the microscopic displacement u_{m}^{t} and velocity $\dot{u}_{\mathrm{m}}^{t}$.

The constant average acceleration scheme

The strong form of Eq. (4.10) in the constant average acceleration scheme is given by

$$\int N^{\mathrm{T}} \rho N \,\mathrm{d}x\, \ddot{u}_{\mathrm{m}}^{t+\Delta t} + \int B^{\mathrm{T}} E B \,\mathrm{d}x\, u_{\mathrm{m}}^{t+\Delta t} = 0 \tag{4.27}$$

The microscopic displacement $u_{\mathrm{m}}^{t+\Delta t}$ and acceleration $\ddot{u}_{\mathrm{m}}^{t+\Delta t}$ can be written as $u_{\mathrm{m}}^{t} + \Delta u_{\mathrm{m}}$ and $\ddot{u}_{\mathrm{m}}^{t} + \Delta \ddot{u}_{\mathrm{m}}$ to replace the microscopic displacement u_{p}^{t} and velocity $\dot{u}_{\mathrm{p}}^{t}$ of the prescribed nodes. Incorporating the microscopic displacement Δu_{m} and acceleration $\Delta \ddot{u}_{\mathrm{m}}$ increments into in Eq. (4.27) leads to

$$\int N^{\mathrm{T}} \rho N \,\mathrm{d}x\, (\ddot{u}_{\mathrm{m}}^{t} + \Delta \ddot{u}_{\mathrm{m}}) + \int B^{\mathrm{T}} E B \,\mathrm{d}x\, (u_{\mathrm{m}}^{t} + \Delta u_{\mathrm{m}}) = 0 \tag{4.28}$$

The microscopic acceleration increment $\Delta \ddot{u}_{\mathrm{m}}$ is replaced by Eq. (A.9) based on an displacement expansion in the constant average acceleration scheme; hence, Eq. (4.28) is rewritten as

$$\begin{aligned} &\int B^{\mathrm{T}} E B \,\mathrm{d}x\, (u_{\mathrm{m}}^{t} + \Delta u_{\mathrm{m}}) + \int N^{\mathrm{T}} \rho N \,\mathrm{d}x\, \ddot{u}_{\mathrm{m}}^{t} \\ &+ \int N^{\mathrm{T}} \rho N \,\mathrm{d}x \Big[\frac{4}{\Delta t^{2}} \Big(\Delta u_{\mathrm{m}} - \dot{u}_{\mathrm{m}}^{t} \Delta t - \frac{1}{4} \ddot{u}_{\mathrm{m}}^{t} \Delta t^{2} \Big) \Big] = 0 \end{aligned} \tag{4.29}$$

Reorganising Eq. (4.29) for the solution of the microscopic displacement increment Δu_{m} results in

$$\begin{aligned} \Big[\int B^{\mathrm{T}} E B \,\mathrm{d}x + \frac{4}{\Delta t^{2}} \int N^{\mathrm{T}} \rho N \,\mathrm{d}x \Big] \Delta u_{\mathrm{m}} = &- \int B^{\mathrm{T}} E B \,\mathrm{d}x\, u_{\mathrm{m}}^{t} \\ &+ \frac{4}{\Delta t} \int N^{\mathrm{T}} \rho N \,\mathrm{d}x\, \dot{u}_{\mathrm{m}}^{t} + \int N^{\mathrm{T}} \rho N \,\mathrm{d}x\, \ddot{u}_{\mathrm{m}}^{t} \end{aligned} \tag{4.30}$$

The right hand side of Eq. (4.30) is assigned as a residual force $f_{\mathrm{m}}^{\mathrm{res}}$ at the microscale. The microscopic residual force is imposed by the microscopic displacement u_{p}^{t} and velocity $\dot{u}_{\mathrm{p}}^{t}$ of the prescribed nodes for each current microscopic time $t_{\mathrm{m}}^{\mathrm{n}}$, given by

$$f_{\mathrm{m}}^{\mathrm{res}} = -f_{\mathrm{m}}^{t}(u_{\mathrm{m}}) + f_{\mathrm{m}}^{t}(\dot{u}_{\mathrm{m}}) + f_{\mathrm{m}}^{t}(\ddot{u}_{\mathrm{m}}) = 0 \tag{4.31}$$

The central difference scheme

The strong form of Eq. (4.10) in the the central difference scheme is given by

$$\int N^{\mathrm{T}} \rho N \,\mathrm{d}x\, \ddot{u}_{\mathrm{m}}^{t} + \int B^{\mathrm{T}} E B \,\mathrm{d}x\, u_{\mathrm{m}}^{t} = 0 \tag{4.32}$$

The left hand side of Eq. (4.32) is assigned as a residual force $f_{\mathrm{m}}^{\mathrm{res}}$ for the central difference scheme at the microscale. The microscopic residual force is imposed by the microscopic displacement u_{p}^{t} of the prescribed nodes for each current microscopic time $t_{\mathrm{m}}^{\mathrm{n}}$, given by

$$f_{\mathrm{m}}^{\mathrm{res}} = -f_{\mathrm{m}}^{t}(u_{\mathrm{m}}) - f_{\mathrm{m}}^{t}(\ddot{u}_{\mathrm{m}}) = 0 \tag{4.33}$$

Comparing implicit and explicit time integrations, the microscopic residual force in the constant average acceleration scheme can be expressed in terms of the prescribed displacement u_{p}^{t} and velocity $\dot{u}_{\mathrm{p}}^{t}$, while the microscopic residual force in the central difference method is only defined by the prescribed displacement u_{p}^{t}. Examples of using time integration methods are discussed in Section 4.8.5

4.7.3 Computational homogenisation solution algorithm

The procedure of dynamic computational homogenisation method is schematised in Figure 4.5 which can be concisely described by the following steps.

The macrostructural boundary value problem is defined at the macroscale by using a finite element scheme. The macrostructure is discretised in space and time. The boundary condition is imposed on the macrostructure, together with the external load in compliance with spatial and temporal discretisations. A microstructural boundary value problem (BVP) over the RVE is assigned to each macroscopic integration point. At the microscale, the RVE is determined according to the separation of length and time scales explained in Sections 4.3.1 and 4.3.2.

In order to obtain the *inital* constitutive material model, an artificial initial macroscopic strain $\varepsilon_{0\mathrm{M}} = 1$ is applied as the prescribed boundary condition of the RVE at the initial macro time step $t_{0\mathrm{M}}$. This forms the static microstructural BVP at the microscale. The solution of the microstructural BVP provides the average of the microscopic stress $\langle \sigma_{\mathrm{m}} \rangle_{\mathrm{x}}$ to

calculate the macrosopic Young's modulus E_{M}. The macroscopic mass density ρ_{M} is simply obtained by the rule of mixture in Eq. (2.1). The initial macroscopic material properties are transferred back to the macroscale.

At the macroscale, the global stiffness and mass matrices are assembled using the initial macroscopic material properties. The macroscopic time integration is carried out to solve the macrostructural BVP for each macroscopic time increment Δt_{M}. The solution of the macrostructural BVP provides the macroscopic acceleration $\ddot{u}_{\mathrm{M}}$, velocity $\dot{u}_{\mathrm{M}}$ and displacement u_{M}. For each macroscopic integration point, the macroscopic strain ε_{M} and velocity $\dot{u}_{\mathrm{M}}$ are imposed as the prescribed boundary condition of its associated RVE through the downscaling procedure explained in Section 4.6.1.

The microscopic time integration is carried out to solve the microstructural BVP for each microscopic time increment Δt_{m}. When the microstructural analysis is completed, the solution of the microstructural BVP provides the microscopic acceleration $\ddot{u}^{f}_{\mathrm{m}}$, velocity $\dot{u}^{f}_{\mathrm{m}}$ and displacement u^{f}_{m} at the end of the microscopic analysis $t^{\mathrm{f}}_{\mathrm{m}}$. As per the upscaling procedure explained in Section 4.6.2, the macroscopic velocity $\dot{u}^{f}_{\mathrm{m}}$ and displacement u^{f}_{m} are spatially integrated to obtain the microscopic averaged stress $\langle \sigma_{\mathrm{m}} \rangle_{\mathrm{x}}$ and momentum $\langle p_{\mathrm{m}} \rangle_{\mathrm{x}}$ (i.e. the macroscopic stress σ_{M} and momentum p_{M}). The microscopic averaged stress $\langle \sigma_{\mathrm{m}} \rangle_{\mathrm{x}}$ and momentum $\langle p_{\mathrm{m}} \rangle_{\mathrm{x}}$ are embedded as the residual force into the macroscopic BVP for the next macroscopic time step t^{n+1}_{M}, thereby one loop of the dynamic computational homogenisation is completed.

When the macroscopic time integration is completed, the macroscopic response of the periodic composite for the given applied load is obtained for each macroscopic time increment Δt_{M}. In case better accuracy in the macroscopic response is required, the choice of the RVE, examples of which are given in the next Section, can be updated depending on the separation of length and time scales.

4.8 Numerical results

In this section, a one-dimensional linear elastic laminate bar is modelled using the dynamic computational homogenisation procedure explained in Sections 4.7.3 to assess the effects of N_{uc} and N_{wp} at the microscale. The bar is clamped on the left end and a constant load $F = 10$ N is applied at the right end throughout the simulation. For the macroscopic boundary value problem, linear finite elements are used with the Newmark time discretisation. On the other hand, for microscopic boundary value problems, both the constant average acceleration scheme and the central difference method are implemented. The critical time step size $t_{\mathrm{crit}} = 0.0625$ s is used in the central difference method for reasons of stability

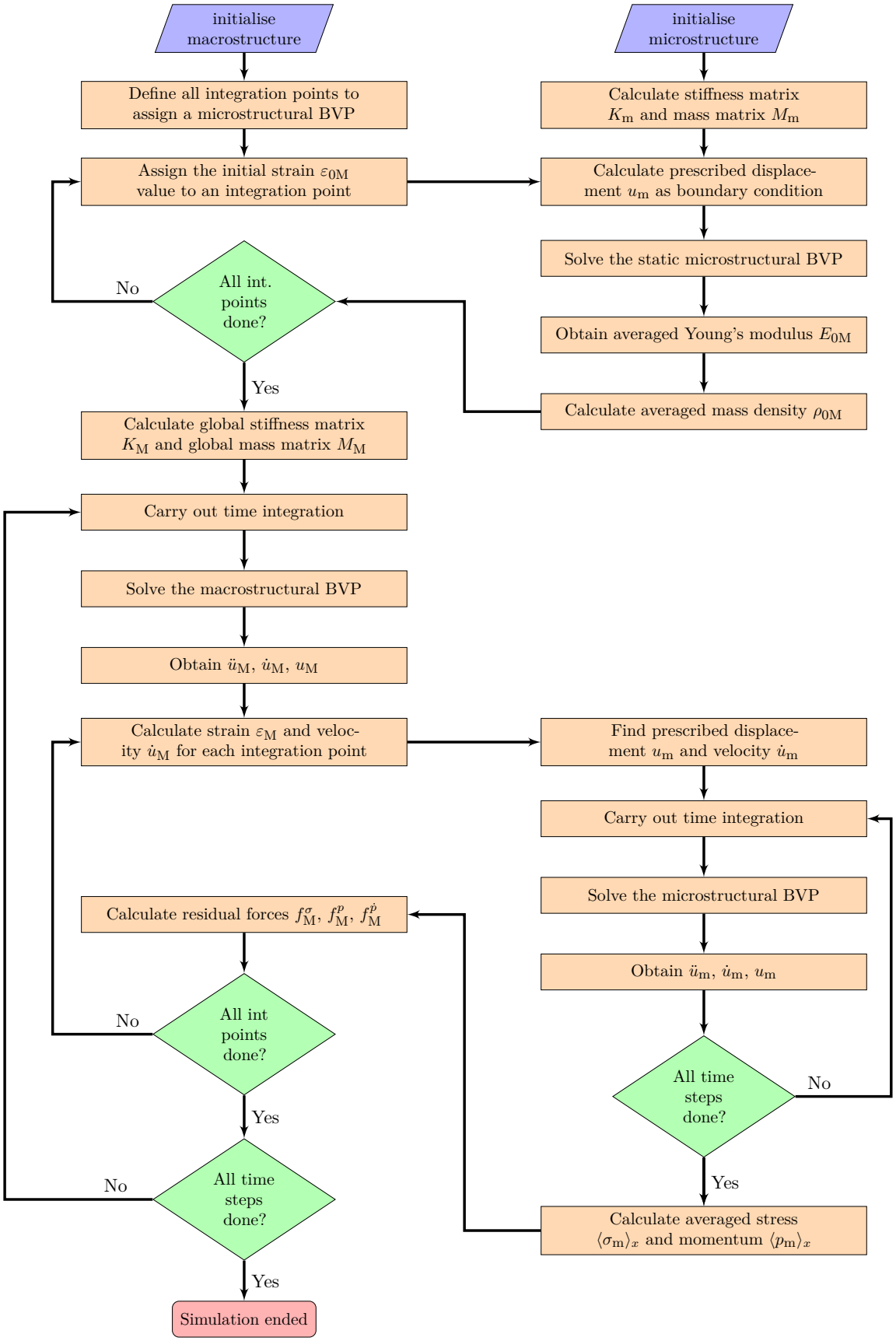

Fig. 4.5 Computational flowchart of dynamic computational homogenisation scheme

as well as accuracy. Furthermore, certainly, the separation of length and time scales is assumed for all analyses below. The results of the multiscale problem are compared with those obtained by direct numerical simulations (DNS) to verify the accuracy of the multiscale model. In direct numerical simulations, the one-dimensional laminate bar is only analysed on the heterogeneous microscale.

For all numerical examples, the error estimation formula is given by

$$\epsilon = \frac{|x_{\mathrm{CH}} - x_{\mathrm{DNS}}|}{|x_{\mathrm{DNS}}|} \cdot 100\% \tag{4.34}$$

where x_{CH} and x_{DNS} are values obtained from the results of computational homogenisation and direct numerical simulations, respectively. The comparison of macroscopic displacements and velocities against those obtained with DNS allows one to assess the accuracy of the local response of the multi-scale model. In order to compare the global response of the multi-scale model, averaged strain and kinetic energies containing microscopic stress and momentum can be formulated as follows

$$\mathcal{U} = \frac{1}{2} u_{\mathrm{M}}^{\mathrm{T}} K_{\mathrm{M}} u_{\mathrm{M}} = \frac{1}{2} \int \varepsilon_{\mathrm{M}}^{\mathrm{T}} \langle \sigma_{\mathrm{m}} \rangle_{\mathrm{x}}^{t} \, \mathrm{d}x \tag{4.35}$$

$$\mathcal{K} = \frac{1}{2} \dot{u}^{\mathrm{T}} M_{\mathrm{M}} \dot{u} = \frac{1}{2} \int \dot{u}^{\mathrm{T}} N^{\mathrm{T}} \langle p_{\mathrm{m}} \rangle_{\mathrm{x}}^{t} \, \mathrm{d}x \tag{4.36}$$

where $\mathcal{U}$ and $\mathcal{K}$ are strain and kinetic energies, respectively. $\langle \sigma_{\mathrm{m}} \rangle_{x}^{t}$ and $\langle p_{\mathrm{m}} \rangle_{x}^{t}$ are upscaling quantities comprising microscopic material constitutive relations.

4.8.1 The effect of $N_{\mathbf{uc}}$

As a first examination of the influence of N_{uc}, the strain and kinetic energies of a one-dimensional linear elastic laminated bar are investigated. Strain and kinetic energies are appropriate quantities to evaluate the impact of an increase in the number of unit cells on the global performance of the multi-scale model. In this analysis, the strain and kinetic energies obtained by the DNS are compared with those obtained by the dynamic computational homogenisation method. The numerical and physical parameters of this analysis are given in Table B.1.

As shown in Figure 4.6, an increase in the number of unit cells N_{uc} results in better estimation of the multi-scale strain energy, while the multi-scale kinetic energy does not show the same trend. The multi-scale acceleration and displacement values have good correlations with those obtained by the DNS with time at higher values of N_{uc}. On the other hand, the multiscale velocity values remain lower than the velocity values obtained by the DNS so that the momentum internal force $f_{\mathrm{M}}^{\mathrm{p}}$ causes a huge error in the multi-scale kinetic energy.

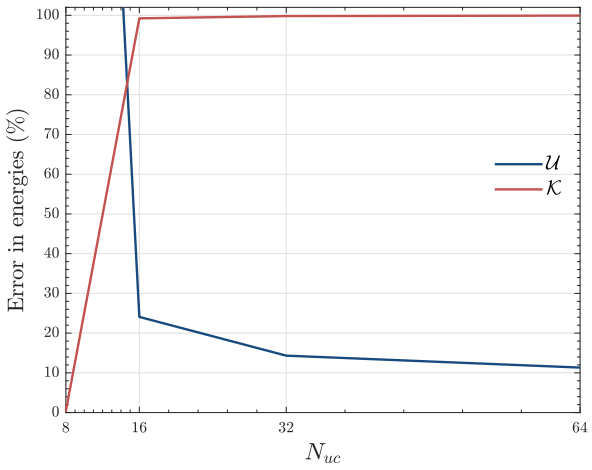

Fig. 4.6 Effect of the number of unit cells on strain and kinetic energies against the reference solution obtained by the DNS.

In addition to evaluating the effect of the number of unit cells on the dynamic response of 1D bar system, macroscopic displacements and velocities at the local scale are also assessed using the dynamic computational homogenisation method. As has been depicted in Figure 4.7, despite showing a consistent trend in both macroscopic results, a higher number of unit cells gives better estimations of the macroscopic displacement and velocity compared to those results obtained from the DNS. Particularly, when $N_{\text{uc}} = 8$ (green line), errors in macroscopic displacement and velocity at $t_{\text{m}} = 5$ s, are 5.44% and 13.41%, respectively.

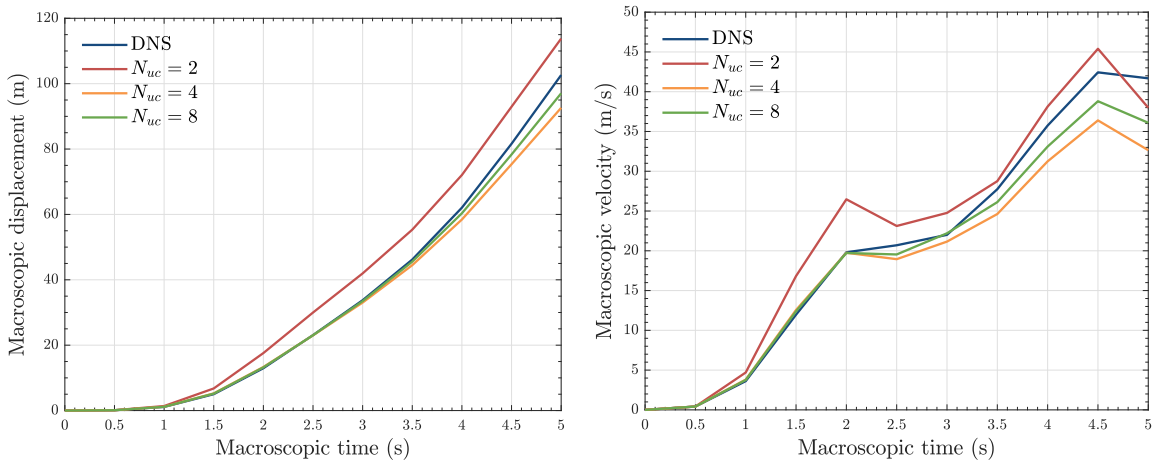

Fig. 4.7 Macroscopic displacement-time (left) and velocity-time (right) curves for $N_{\text{wp}} = 8$ and various N_{uc} together with the reference solution obtained by the DNS.

4.8.2 The effect of $N_{\mathbf{wp}}$

In contrast with N_{uc} analysis, the number of wave propagations (i.e. the number of times the wave front travels through the entire microscopic sample) is increased while eight unit cells are used throughout this analysis. For each number of wave propagations, indicated with N_{wp}, the results obtained from the dynamic computational homogenisation are compared with the results obtained by the DNS. At higher values of N_{wp}, the kinetic energy converges perfectly. Although the error in strain energy tend to decrease with an increase in N_{wp}, higher N_{uc} provides better results for strain energy. When N_{wp} increases, longer averaged stress profiles can be obtained on the micro-level. As a upscaling parameter, the averaged stress at the end of the micro simulation time is transferred to the macro-level. The micro simulation time is critical to be determined since a microscopic wave is required to reach at the end of the microscopic bar to contain all microscopic characteristics for multi-scale analyses. When the spatial and temporal links are performed between macro and microstructures, the results of macroscopic stress and momentum are not accurate. As long as the numerical parameters such as minimum wave propagation time and critical time step are satisfied, higher number of wave propagations gives better estimates for averaged stress and momentum. Therefore, this also proves the importance of N_{wp} on multi-scale results obtained by the dynamic computational homogenisation method.

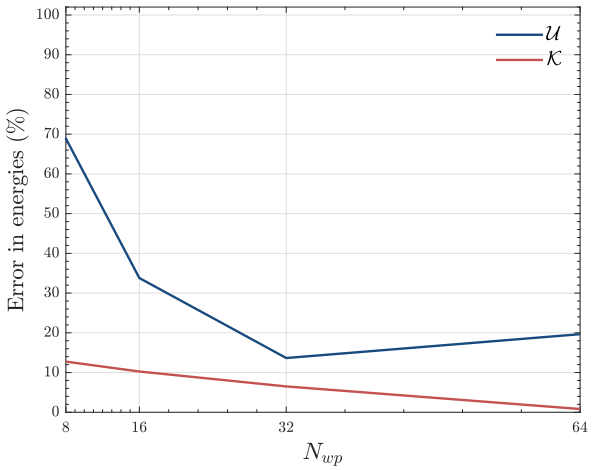

Fig. 4.8 Effect of the number of wave propagations on strain $\mathcal{U}$ and kinetic energies $\mathcal{K}$ against the reference solution obtained by the DNS.

The local responses of microscopic boundary value problem is also observed. In Figure 4.9, higher number of wave propagation results in a good approximation of macroscopic displacement and velocity compared to the DNS results. In particular, when $N_{\mathrm{wp}} = 8$ (green line), the errors in macroscopic displacement and velocity at $t_{\mathrm{m}} = 5$ s are 2.97% and 6.85%,

respectively. Additionally, a slight change in N_{uc} leads to a great amount of reduction in displacement and velocity errors, as shown in Figure 4.9.

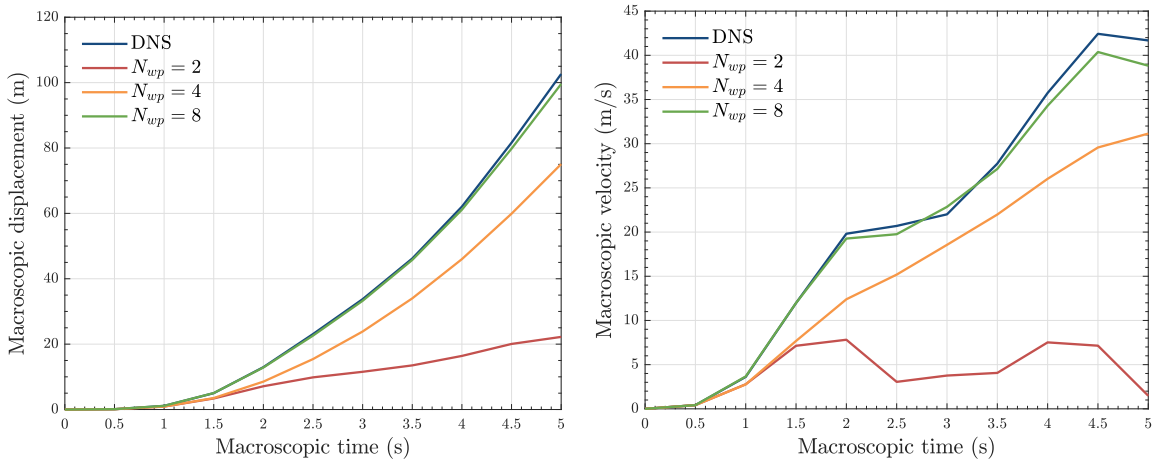

Fig. 4.9 Macroscopic displacement-time (left) and velocity-time (right) curves at the value of $N_{\text{uc}} = 8$ for various N_{wp} values with the reference solution obtained by the DNS.

4.8.3 The combination of N_{uc} and N_{wp}

Building upon the findings presented in Chapter 3, the advantages of N_{uc} for accurately calculating the strain energy and N_{wp} for accurately calculating the kinetic energy are combined. Therefore, to achieve the highest level of accuracy in both strain and kinetic energy calculations, the superior performance of an simultaneous increase in N_{uc} and N_{wp} is evaluated by comparing to their individual components. As demonstrated in Sections 4.8.1 and 4.8.2, the closest satisfactory results of the dynamic response of 1D bar are accomplished by applying eight unit cells and eight wave propagations, which are considered the minimum starting values for all analyses. As shown in Figure 4.10, for the strain and kinetic energy, the combination of $N_{\text{uc}} = 64$ and $N_{\text{wp}} = 64$ gives minimum error at 10.5% and 0.6%, respectively. For any point in Figure 4.10, the simultaneous increase of N_{uc} and N_{wp} results in higher accuracies than separate increases of either N_{uc} or N_{wp}.

4.8.4 Different impedance contrasts

The simultaneous increase of N_{uc} and N_{wp} presented in Section 4.8.3 is considered the best effective estimation tool for overall properties. Therefore, the effect of this combination on the contrast in mechanical impedance of materials is investigated in this section. The material properties of the microscopic structure such as Young's modulus E and mass density ρ are arranged in accordance with a user-defined impedance contrast factor $z = \sqrt{E\rho}$, yet the wave speeds of each material $c = \sqrt{E/\rho}$ are aimed to remain unchanged.

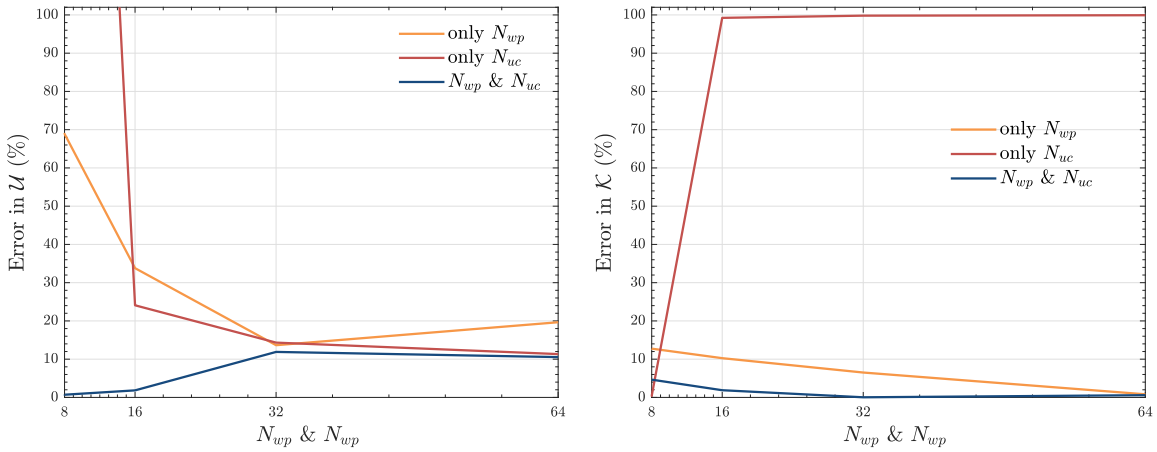

Fig. 4.10 Comparison of different N_{uc} and N_{wp} combinations with regards to strain energy (left) and kinetic energy (right).

To begin with, the local displacement responses at the mid-point of the bar are shown in Figure 4.11 for various impedance contrast factors from low to moderate contrasts. The simultaneous increase in N_{uc} and N_{wp} provides good estimations for all impedance contrast factors compared to the DNS solutions. In addition, there is a consistent trend for different impedance contrast factors and their error estimation. When the impedance contrast factor is low (e.g. $z_{\mathrm{m}} = 1.2$), the local error estimation reaches the lowest value of 0.5%. With the moderately high impedance contrast factor (e.g. $z_{\mathrm{m}} = 2$), the local error estimation is approximately 10.8%.

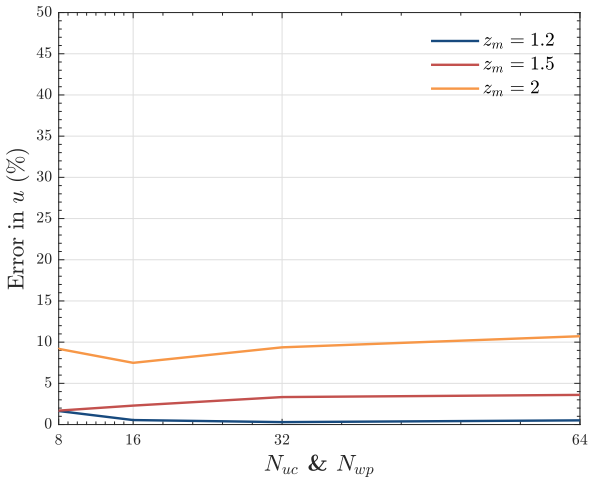

Fig. 4.11 Influence of N_{uc} and N_{wp} on macroscopic displacements at the mid-point of the bar for various impedance contrast factors. Error estimations in macroscopic displacements are computed based on the DNS solutions.

Moreover, the performance of simultaneous increase in N_{uc} and N_{wp} is also observed on the global response of the bar based on the strain and kinetic energies. As depicted in Figure

4.12, errors in the strain energy at $N_{\mathrm{uc}} = 64$ and $N_{\mathrm{wp}} = 64$ are concentrated around 6 - 10% for all impedance contrast factors. On the other hand, as expected, the prediction of this model becomes less accurate for higher impedance contrast values (e.g. $z_{\mathrm{m}} = 2$). While the error in kinetic energy for low impedance contrast (e.g. $z_{\mathrm{m}} = 1.2$) is 0.6%, the one for moderately high impedance contrast (e.g. $z_{\mathrm{m}} = 2$) is 29.7%.

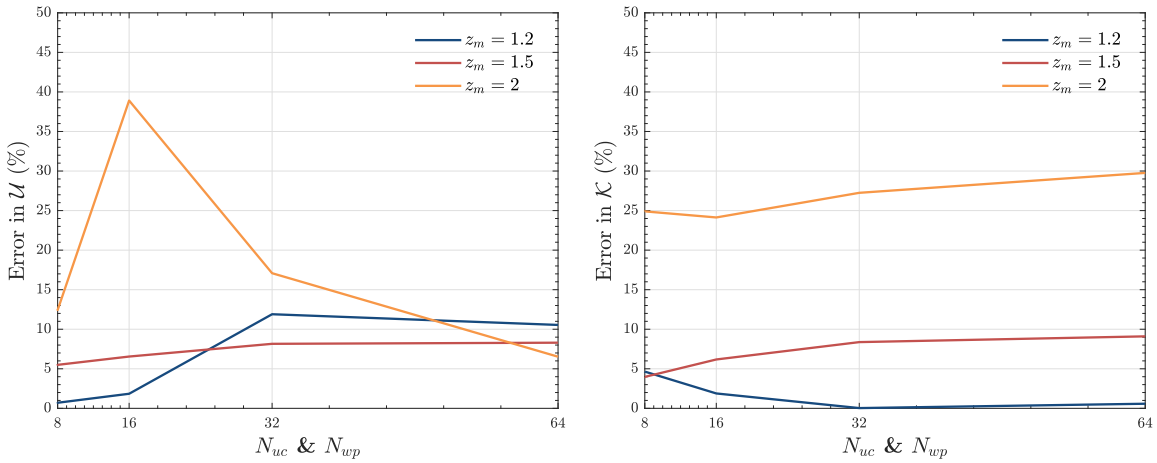

Fig. 4.12 Global influences of N_{uc} and N_{wp} on strain energy (left) and kinetic energy (right) for various impedance contrast factors. Error estimations in macroscopic displacements are computed based on the DNS solutions.

4.8.5 Explicit time integration on micro level

Instead of implicit time integration on the micro-level, explicit time integration can also be used for the microscopic boundary value problem. The central difference method, which is conditionally stable depending on the critical time step Δt_{crit}, is used to discretise the microstructural response in time. For reasons of stability, the microscopic time step Δt_{m} used in the developed algorithm is required to be not larger than the critical time step on the micro-level.

Firstly, the dynamic response of the bar in terms of macroscopic displacements is presented in Figure 4.13 to compare the effect of simultaneous increases in N_{uc} and N_{wp} on the central difference method for various impedance contrasts. The proposed combination represents satisfying estimations with the explicit time integration for several impedance contrasts against the DNS solutions. For the lowest impedance contrast (e.g. $z_{\mathrm{m}} = 1.2$, blue line), the error estimation of displacement at the mid-point of the bar reaches 0.6%, giving less error than implicit time integration shown in 4.11. On the contrary, for a moderately high impedance contrast (e.g. $z_{\mathrm{m}} = 2$, orange line), the error estimation of displacement at the mid-point of the bar in explicit time integration is around 14% and slightly higher than the

one predicted by the implicit time integration (10.8%).

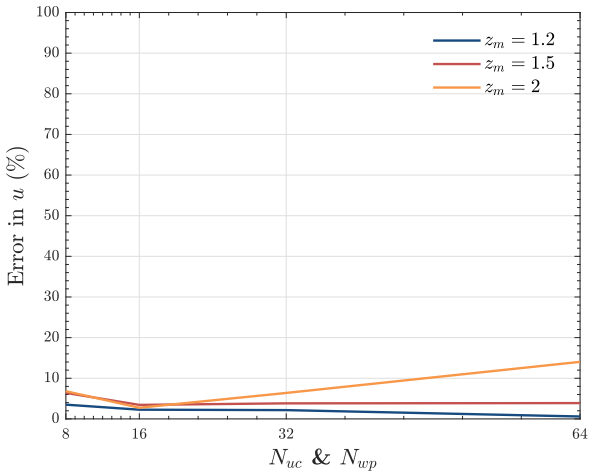

Fig. 4.13 Influences of N_{uc} and N_{wp} on macroscopic displacements at the mid-point of the bar for various impedance contrast factors. Error estimations in macroscopic displacements are computed based on the DNS solutions.

As presented in Figure 4.14, the errors in potential energy for different contrasts are between 12 - 34%, whereas those in kinetic energy are between 0.03 - 39%. For the global response of the bar, not surprisingly, higher impedance contrasts result in higher error estimations. Compared to the results of strain and kinetic energies in implicit time integration analyses, those obtained using the explicit time integration method for low impedance contrast provide better estimation. However, for high impedance contrasts, the global response obtained using the implicit time integration method has more satisfying performance.

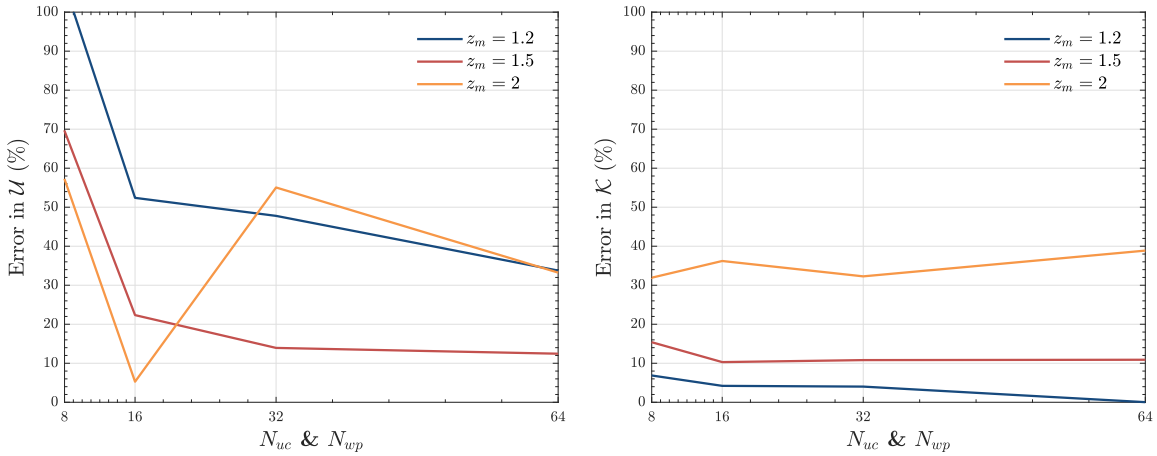

Fig. 4.14 Influence of N_{uc} and N_{wp} on strain energy (left) and kinetic energy (right) for various impedance contrast factors. Error estimations in macroscopic displacements are computed based on the DNS solutions.

4.9 Discussion

In this chapter, the separation of time scales in the dynamic computational homogenisation method is presented along with the separation of length scales. The proposed approach demonstrates the effects of increase in the number of unit cells as well as increase in the number of wave propagations at the microscale. In order to investigate the effectiveness of this proposed work, linear dynamic analyses is carried out for a one-dimensional laminate bar and verified by the DNS solutions. Firstly, it is found that an increase in the number of unit cells significantly reduces the error in strain energy results, while an increase in the number of wave propagations significantly reduces the error in kinetic energy results. To combine those advantages for microstructures, increases in the number of unit cells and wave propagations are simultaneously controlled to obtain better convergence of macroscopic response in dynamics. Additionally, the effect of these simultaneous increases is evaluated for various impedance contrasts of material properties at the microscale. Despite achieving considerable convergence of macroscopic response, the model becomes less accurate with high impedance contrasts in material properties.

In order to investigate the efficiency of this proposed work, the DNS solutions require a significant number of degrees of freedom, estimated to be around 10^6, due to the periodic repetition of the discretized RVE model and the need for mesh refinement. This is about 100 times more than the homogenized model, indicating a substantial reduction in computational cost.

The effect of the number of unit cells and the number of wave propagations is assessed in the numerical and computational homogenisation frameworks, which are outlined in Chapters 3 and 4, respectively. The former approach employs solely the upscaling procedure, with both space-time averaging, while the latter employs the up-and-downscaling procedure with only space averaging. Nevertheless, the results obtained from both frameworks indicate that a simultaneous increase in the number of unit cells and wave propagations leads to better convergence of the macroscopic response in both frameworks.

Chapter 5

Dynamic Gradient Elasticity Length Scales

This chapter explores a more efficient way to capture the dynamic behaviour of periodic laminates in gradient elasticity theories, drawing upon the knowledge gained in Chapter 3 and Chapter 4. The dynamic representative volume element (RVE) size obtained in Chapter 3 enables the quantification of the dynamic length scale parameter in the gradient elasticity method. The advancements in the accuracy of the macroscopic response achieved through the computational homogenisation framework presented in Chapter 4 stimulate to determine length scales for dynamic multiscale problems.

5.1 Introduction

Size effects express the changes in the mechanical properties and behaviour of a material such as its strength and stiffness at different scales, particularly at the microscale. When there is a strong interaction between structural dimensions and microstructural length scales in the mechanical response of the material, the material becomes size-dependent. Modelling size effects are of great interest to researchers as they enable tailoring the material properties at the microscale [101, 102]. Classical continuum theories focus on the response of a material point resulting from the first-order derivative of the displacement. Classical equations of continuum mechanics cannot describe the mechanics of size-dependent materials in composites such as fibre, woven, and lattice due to the absence of internal length scales underlying the mechanical and physical behaviour of microstructures. The size effects become significant when the size of a structure and its internal length are similar. Despite their limited usefulness in size-dependent composite problems, classical continuum theories can be expanded in their spatial and temporal response. In order to capture the spatial effect of heterogeneity on the material response at various scales (i.e. micro, meso and macro), classical continuum theories are extended into gradient elasticity theories containing higher-order derivatives of the displacement (i.e. strain gradients) [103]. A second advantage of gradient elasticity theories concerns the removal of nonphysical singularities. Classical continuum theories are incapable of removing singularities in stress and strain fields that emerge from re-entrant corners in the geometry, abrupt changes in boundary conditions, or concentrated loads. Higher-order derivatives of the displacement in gradient elasticity theories can be employed to smoothen singularities, thus leading to a more realistic response of the structure that lends itself better to interpretations on structural strength and structural integrity [104].

A third advantage of gradient theories is that they are able to describe deviations in the dynamic response of composites that emerge from their microstructure. When an elastic wave propagates through a composite material, reflection and refraction occur at the interface of composite components. The extent of these interactions depends on the wavelength and frequency of the harmonic components, and therefore harmonic waves of different wavelengths travel at different speeds so that the elastic wave propagation becomes dispersive. The prediction of wave dispersion cannot be captured by classical continuum theories unless all microstructural details are explicitly included, causing enormous computational effort and cost. As an alternative, gradient elasticity theories may include higher-order derivatives of the acceleration (i.e. inertia gradients) to cope with the deficiency of modelling wave dispersion [71].

Combining the capabilities of strain and inertia gradients enables obtaining dynamically consistent gradient models to overcome size-effect, singularity and wave dispersion problems [71]. Higher-order derivatives with respect to space and time are accompanied by associated

length scale parameters that build a link with the material behaviour of microstructure as additional constitutive constants. While the length scale parameter appearing with high-order strain is known as the static length scale parameter ℓ_s, the one appearing with inertia gradients is known as the dynamic length scale parameter ℓ_d. As length scale parameters determine the contribution of higher-order gradients, appropriate values of length scale parameters should be acquired for the accuracy of a gradient elasticity model.

Even though identification and quantification of length scale parameters are directly associated with the size of microstructures, selecting length scale parameters can still be challenging. As a representation of microstructure, a representative volume element (RVE) contributes to selecting the length scale parameters. The static length scale parameter can directly be linked to the size of the RVE, whereas the dynamic length scale parameter varies with the geometric and material properties of the RVE [2]. Accordingly, calculating the dynamic length scale parameter is more challenging compared to the static length scale parameter due to its nature. In Chapter 3, larger sizes of the RVE in dynamics by applying the separation of length scales provide better convergence in predicting the microstructure response. This chapter will present a procedure to select the dynamic length scale parameter connected to the size of RVE such that the response of a dynamically consistent gradient model is not affected by the dynamic length scale parameter. A one-dimensional periodically laminated bar is used with a series of numerical examples to demonstrate the effect of the

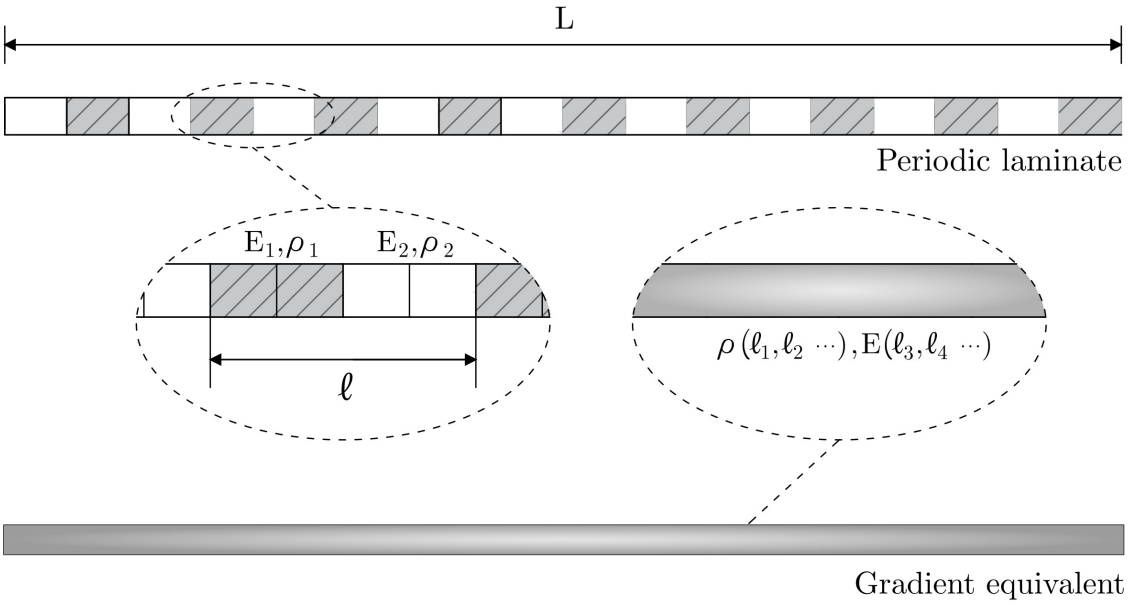

Fig. 5.1 One-dimensional periodic laminated bar (top) and its equivalent gradient elasticity model (bottom)

dynamic length scale parameter on the response of the material and quantify the dynamic length scale parameter.

5.2 Gradient elasticity model in dynamics

Gradient elasticity theories enhance the classical continuum with additional higher-order spatial and temporal derivatives to resolve static and dynamic inconsistencies, as detailed with examples in the previous section. This section presents a dynamically consistent gradient elasticity model with stable strain and inertia gradients accompanied by the static and dynamic length scale parameters. This gradient elasticity model is also decoupled by a developed operator split to avoid inconvenient continuity requirements due to higher-order derivations.

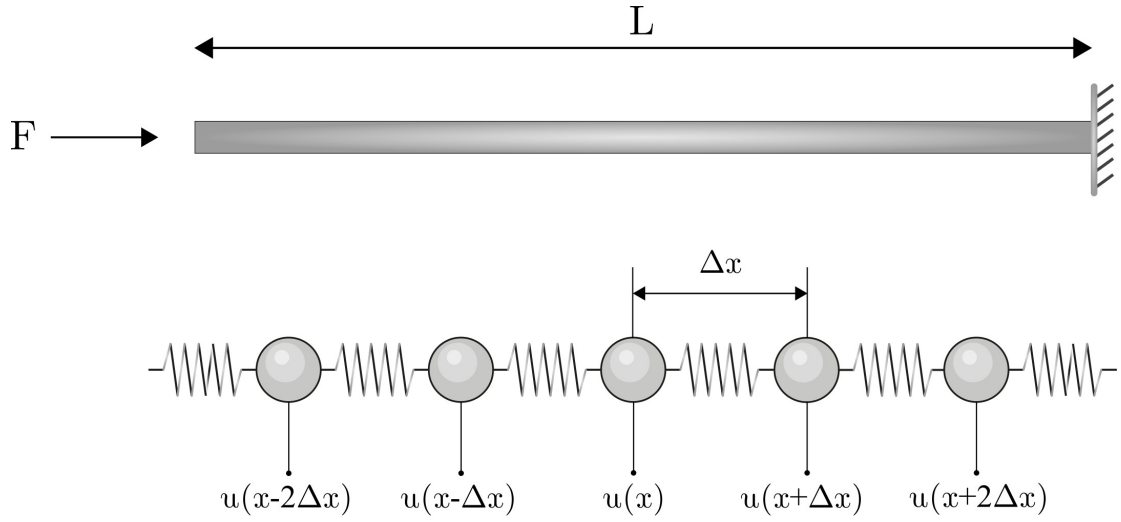

Fig. 5.2 One-dimensional gradient elasticity bar (top) and its discrete model comprising of masses linked by springs (bottom)

5.2.1 Formulation of the gradient elasticity model

Classical continuum mechanics focus on the macroscopic response of composite materials by neglecting the underlying microstructure. The mathematical model of the classical continuum can be formed by a discrete model comprising mass and spring elements depicted in Figure 5.2, which enables the material to be modelled analytically and numerically. In the classical continuum theory, the equation of motion for a one-dimensional linear elastic material is expressed as

$$\rho\,\ddot{u} - E\,\frac{\partial^2 u}{\partial x^2} = 0 \tag{5.1}$$

Gradient elasticity models consist of the mechanical behaviour of a material point and its neighbour interactions to describe microstructural effects in composite materials. In order to include neighbour interactions in the continuum model, Taylor expansion approximation is derived with respect to space and time to obtain displacement and acceleration. At a given time t, the displacement $u(x \pm \Delta x, t)$ and acceleration $\ddot{u}(x \pm \Delta x, t)$ of a material point x can be written as

$$u(x \pm n\Delta x, t) \approx u(x,t) \pm \Delta x \frac{\partial u(x,t)}{\partial x} + \frac{1}{2}\Delta x^2 \frac{\partial^2 u(x,t)}{\partial x^2} \pm \cdots + \mathcal{O}(\Delta x^{\mathrm{n}}) \tag{5.2}$$

$$\ddot{u}(x \pm n\Delta x, t) \approx \ddot{u}(x,t) \pm \Delta x \frac{\partial \ddot{u}(x,t)}{\partial x} + \frac{1}{2}\Delta x^2 \frac{\partial^2 \ddot{u}(x,t)}{\partial x^2} \pm \cdots + \mathcal{O}(\Delta x^{\mathrm{n}}) \tag{5.3}$$

where Δx is the distance between two neighbour materials and $\mathcal{O}$ is the truncation error with the nth degree of Taylor polynomial. When Expansions (5.2) and (5.3) are substituted into the potential energy density and the kinetic energy density, respectively, the formulation of a series of gradient elasticity models can be derived according to Mindlin's theory of elasticity [105]. Rewriting Eq. (5.1) with higher-order terms in the Expansions (5.2) and (5.3) to obtain the general form of the equation of motion in the gradient elasticity gives

$$\rho\left(\ddot{u} - \ell_1^2 \frac{\partial^2 \ddot{u}}{\partial x^2} + \ell_2^4 \frac{\partial^4 \ddot{u}}{\partial x^4} \pm \cdots\right) = E\left(\frac{\partial^2 u}{\partial x^2} - \ell_3^2 \frac{\partial^4 u}{\partial x^4} + \ell_4^4 \frac{\partial^6 u}{\partial x^6} \pm \cdots\right) \tag{5.4}$$

where ℓ_1, ℓ_2, ℓ_3 and ℓ_4 are length scales linking the material response to their underlying microstructure. The existence of ℓ_3 and ℓ_4 with strain gradients in Eq. (5.4) leads to avoiding singularities in the stress and strain fields [104]. When Eq. (5.4) is truncated after the second-order strain gradient term with $\ell_1 = \ell_2 = 0$ (i.e. the second-order gradient model), all waves propagates with unrealistic high velocities. On the other hand, when Eq. (5.4) is truncated after the fourth-order strain gradient term with $\ell_1 = \ell_2 = 0$ (i.e. the fourth-order gradient model), only waves with higher wave numbers causes unrealistic high velocities affecting the response of the material [104]. Thus the gradient models cannot capture wave dispersion completely. Moreover, the higher-order inertia gradients appearing with ℓ_1 and ℓ_2 achieves resolving dynamic inconsistencies in the both second and fourth-order gradient models. When the second-order inertia gradient appearing with ℓ_1 in Eq. (5.4) is accompanied by the second-order strain gradient with ℓ_3, the advantage of removing singularities in the strain field is combined with capturing realistic wave dispersion [71]. Although the fourth-order gradient model is improved by adding the fourth-order inertia gradient, the use of the fourth-order gradient model is restricted by continuity requirements [106]. For a dynamically consistent gradient elasticity model, the one-dimensional equation of motion with higher-order gradient terms is given by [72]

$$\rho\left(\ddot{u}-\ell_{\mathrm{d}}^{2}\frac{\partial^{2}\ddot{u}}{\partial x^{2}}\right)=E\left(\frac{\partial^{2}u}{\partial x^{2}}-\ell_{\mathrm{s}}^{2}\frac{\partial^{4}u}{\partial x^{4}}\right) \tag{5.5}$$

where ℓ_{s} and ℓ_{d} are the static and dynamic length scale parameters, respectively. The solution of Eq. (5.5) is challenging to obtain as the fourth-order spatial derivatives requires $\mathscr{C}^1$-continuity of the interpolation functions in numerical discretisation. For simplification, the discretisation strategy introduced by Askes *et al.* [72] transforms the dynamically consistent gradient elasticity equation of motion from $\mathscr{C}^1$-continuity with the fourth-order partial differential equation to $\mathscr{C}^0$-continuity with two second-order partial differential equations by using Ru-Aifantis theorem [70]. The equation of motion of the dynamically consistent gradient model Eq. (5.5) including fourth-order spatial derivations with the absence of body forces is separated by displacements u_{M} and u_{m} into fully coupled equations:

$$\rho\left(\ddot{u}_{\mathrm{M}}-\ell_{\mathrm{d}}^{2}\frac{\partial^{2}\ddot{u}_{\mathrm{M}}}{\partial x^{2}}\right)=E\,\frac{\partial^{2}u_{\mathrm{m}}}{\partial x^{2}} \tag{5.6}$$

with

$$u_{\mathrm{m}}=u_{\mathrm{M}}-\ell_{\mathrm{s}}^{2}\,\frac{\partial^{2}u_{\mathrm{M}}}{\partial x^{2}} \tag{5.7}$$

where subscripts m and M denote microscopic and macroscopic quantities, which are determined by the comparison of Mindlin's theory of elasticity [105] with the associated integral nonlocality of strain [107]. In Eq. (5.7) u_{M} at a certain position is obtained by a nonlocal averaging u_{m} over a certain volume at the microscale. Also, the volume of averaging u_{m} at the microscale is determined by an internal length which is similar concept with the length scale parameter in Eq. (5.7). These interpretation enable defining displacement quantities in Eqs. (5.6) and (5.7) as macroscopic and microscopic [2].

For the ease of implementation, rearranging Eq. (5.7) by taking second time derivative gives

$$\ddot{u}_{\mathrm{m}}=\ddot{u}_{\mathrm{M}}-\ell_{\mathrm{s}}^{2}\,\frac{\partial^{2}\ddot{u}_{\mathrm{M}}}{\partial x^{2}} \tag{5.8}$$

The term $\frac{\partial^2 \ddot{u}_{\mathrm{M}}}{\partial x^2}$ in Eq. (5.6) is replaced by Eq. (5.8) after multiplying with $\ell_{\mathrm{d}}^2/\ell_{\mathrm{s}}^2$. In addition, Eq. (5.8) is updated by multiplying with $\rho(1-\ell_{\mathrm{d}}^2/\ell_{\mathrm{s}}^2)$. Therefore, the new fully coupled sets of equations in dynamics are reformulated as

$$\rho\left(\frac{\ell_{\mathrm{d}}^{2}}{\ell_{\mathrm{s}}^{2}}\ddot{u}_{\mathrm{m}}-\frac{\ell_{\mathrm{d}}^{2}-\ell_{\mathrm{s}}^{2}}{\ell_{\mathrm{s}}^{2}}\ddot{u}_{\mathrm{M}}\right)=E\,\frac{\partial^{2}u_{\mathrm{m}}}{\partial x^{2}} \tag{5.9}$$

$$\rho\left(-\frac{\ell_{\mathrm{d}}^{2}-\ell_{\mathrm{s}}^{2}}{\ell_{\mathrm{s}}^{2}}\ddot{u}_{\mathrm{m}}+\frac{\ell_{\mathrm{d}}^{2}-\ell_{\mathrm{s}}^{2}}{\ell_{\mathrm{s}}^{2}}\ddot{u}_{\mathrm{M}}-\left(\ell_{\mathrm{d}}^{2}-\ell_{\mathrm{s}}^{2}\right)\frac{\partial^{2}\ddot{u}_{\mathrm{M}}}{\partial x^{2}}\right)=0 \tag{5.10}$$

The form of Eqs. (5.9) and (5.10) paves the way for determining the kinetic and strain energy densities of the dynamically consistent gradient model denoting by $\mathcal{K}_{\mathrm{g}}$ and $\mathcal{U}_{\mathrm{g}}$, respectively, that is

$$\mathcal{K}_{\mathrm{g}} = \frac{1}{2}\rho\left(\dot{u}_{\mathrm{m}}^2 + \frac{\ell_{\mathrm{d}}^2 - \ell_{\mathrm{s}}^2}{\ell_{\mathrm{s}}^2}(\dot{u}_{\mathrm{m}} - \dot{u}_{\mathrm{M}})^2 + (\ell_{\mathrm{d}}^2 - \ell_{\mathrm{s}}^2)\frac{\partial \dot{u}_{\mathrm{M}}}{\partial x}^2\right) \tag{5.11}$$

and

$$\mathcal{U}_{\mathrm{g}} = \frac{1}{2}\varepsilon_{\mathrm{m}} E \varepsilon_{\mathrm{m}} \tag{5.12}$$

where ε_{m} is the microscopic strain and the first-order derivative of u_{m}. According to the energy-based positive definiteness in physics, the dynamic length scale parameter ℓ_{d} should be larger than the static length scale parameter ℓ_{s} in Eq (5.11). As it happens, such a choice also leads to realistic dispersion characteristics in the gradient elasticity model [72].

5.3 Wave dispersion

The description of wave dispersion for a one-dimensional periodic laminate bar is briefly recapped in this section. The general solution form of a harmonic wave at a certain point x with a certain time t is written as

$$u = A\exp(ik(x - c_{\mathrm{p}}t)) \tag{5.13}$$

where A is the amplitude, i is the imaginary number defined by $i = \sqrt{-1}$, k is the wave number and c_{p} is the phase velocity. In order to simulate wave dispersion, the second-order derivatives of the displacement and the acceleration are employed in the gradient elasticity model. Substituting Eq. (5.13) into Eq. (5.5), the equation of motion of the dynamically consistent gradient model becomes

$$-\rho k^2 c_{\mathrm{p}}^2 - \rho \ell_{\mathrm{d}}^2 k^4 c_{\mathrm{p}}^2 = -Ek^2 - E\ell_{\mathrm{s}}^2 k^4 \tag{5.14}$$

Eq. (5.14) can be expressed for dispersion curves in the dimensionless form, namely

$$\frac{c_{\mathrm{p}}^2}{c_{\mathrm{e}}^2} = \frac{1 + \ell_{\mathrm{s}}^2 k^2}{1 + \ell_{\mathrm{d}}^2 k^2} \tag{5.15}$$

c_{e} is the wave speed of a one-dimensional elastic bar, defined as $c_{\mathrm{e}} = \sqrt{E/\rho}$. When the phase velocity c_{p} depends on the wave number k, wave propagation becomes dispersive [108]. Consequently, Eq. (5.15) expresses a dispersion relation. On the basis of the dispersion relation, when the length scale parameters are equal to each other, i.e. $\ell_{\mathrm{s}} = \ell_{\mathrm{d}}$, the characteristic of wave propagation becomes non-dispersive as demonstrated in Figure 5.3. In addition, the phase velocity of a wave is the ratio of frequency to wave number as $c_{\mathrm{p}} = \omega/k$.

The waves with higher wave numbers (i.e. short wavelengths) propagate faster than the waves with smaller wave numbers (i.e. long wavelengths). Accordingly, for physically realistic numerical simulations of dispersion, $\ell_{\mathrm{s}} < \ell_{\mathrm{d}}$ should be adopted. Higher wave numbers due to short wavelengths approaching the size of microstructures ℓ propagate with the wave speed controlled by both length scale parameters in order to simulate dispersive characteristics. As shown in Figure 5.3, several magnitudes of the dynamic length scale parameter lead to changes in the wave speed based on wave numbers. For high wave numbers, i.e. $k \to \infty$, the wave speed of strong dispersion (i.e. orange line) is almost two and three times higher than the wave speeds of the intermediate (i.e. red line) and weak (i.e. blue line) dispersion, respectively. Consequently, the ratio $\ell_{\mathrm{d}}/\ell_{\mathrm{s}}$ should be determined to capture wave dispersion accurately.

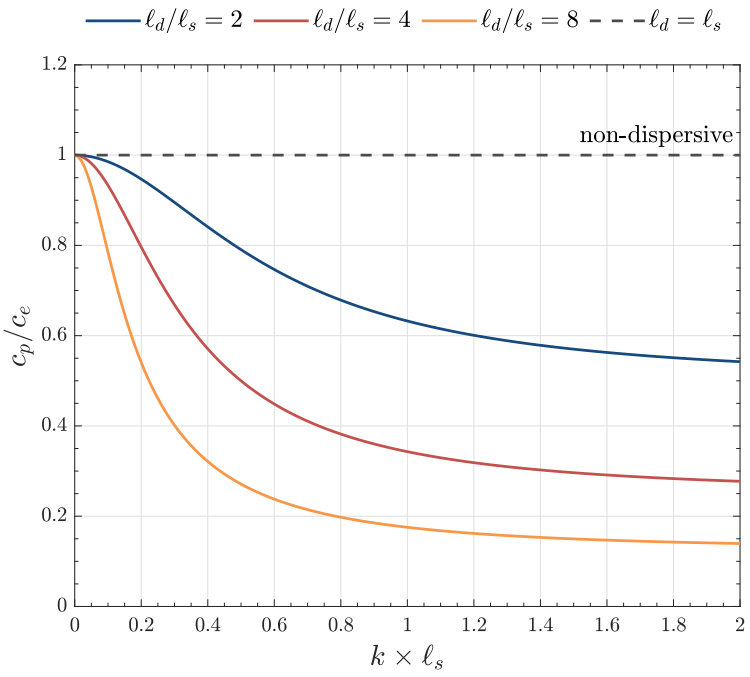

Fig. 5.3 Dispersion relations with the change of ℓ_{d} - normalised phase velocity versus normalised wave number for $\ell_{\mathrm{s}} = 1\mathrm{m}$

5.4 Gradient length scale parameters

Gradient length scales convey material properties of a mechanical model on multiple scales, commonly microstructures, incorporating enriched constitutive relations in the overall behaviour of composites. The selection of length scale parameters should be rigorous, resulting in small enough to embrace all microstructural properties, but in the meantime, large enough to maintain resolution. The quantification of length scales depends on stiffnesses and densities

of the material, volume fractions and contrasts in the material, and the size of the RVE [27, 82, 105]. As depicted in Eq. (5.5), the dynamically consistent gradient elasticity equation of motion contains two internal length scale parameters. The static length scale parameter emerges with higher-order derivatives of the displacement, whereas the dynamic length scale parameter emerges with higher-order derivatives of the acceleration. Whereas the static length scale parameter is directly connected to the static RVE size underlying the length of the microstructure, as explained in Appendix D, the dynamic length scale parameter is connected to the dynamic RVE size. Notably, for periodic laminates, the static length scale parameter is given by [31, 32]

$$\ell_{\mathrm{s}} = \frac{L_{\mathrm{m}}}{\sqrt{12}} \tag{5.16}$$

where L_{m} is the size of a representative volume element. For periodic laminates, L_{m} is set equal to the size of the microstructural unit cell. Furthermore, as has been depicted in Eq. (5.11), the dynamic length scale parameter must be greater than the static length scale parameter to predict realistic wave dispersion in the microstructure [72]:

$$\ell_{\mathrm{s}} < \ell_{\mathrm{d}} \tag{5.17}$$

On the ground that the dynamic length scale parameter is determined by the dynamic RVE size, geometric and material properties such as volume fractions and contrasts should be considered to determine the dynamic length scale parameter. Increases in the contrast of the material lead to the increase in the dynamic length scale parameter underlying the increase in the RVE size [27, 82]. An enlargement factor to obtain the dynamic length scale parameter with respect to the static length scale parameter is presented by Bennett *et al.* [2] as a result of the averaged material properties in Eqs. (3.17) and (3.18) embedded into the gradient elasticity equation of motion in Eq. (5.5), that is

$$\ell_{\mathrm{d}} = \ell_{\mathrm{s}}\sqrt{\gamma + 1} \tag{5.18}$$

with

$$\gamma = \left[\frac{\alpha(1-\alpha)(E_1\rho_1 - E_2\rho_2)}{\rho_{\mathrm{avr}}\big((1-\alpha)E_1 + \alpha E_2\big)}\right]^2 \tag{5.19}$$

where γ is the coefficient of the length scale parameter. Although the enlargement factor incorporates the contrast of the material in addition to the material properties, the dynamic length scale parameter calculated by Eq. (5.18) can be improved to capture a wider range of contrasts in the material. Consequently, an improved derivation of Eq. (5.18) enables better estimation of the dynamic length scale parameter for dynamic gradient elasticity problems. Apart from using the enlargement factor to quantify the dynamic length scale parameter,

in this work, the dynamic length scale parameter of periodic laminates is proposed to be calibrated by the curve fitting algorithm schematised in Figure 5.4.

The first step of the curve fitting algorithm is to initialise a gradient elasticity model since the geometric and material properties of periodic laminates are defined in this step. Then, the number of different magnitude wavelengths is selected to determine the distance considered in the curve fitting optimisation. The amplitudes of the displacement curves weakens with the intensity of heterogeneity in the material due to a reduction of wave speeds. Therefore, the distance is arranged to concentrate on the first peak involving more robust assessment of the dispersion behaviour.

As a starting point for finding provisional values of the dynamic length scale parameter, the coefficient γ containing contrast of the material is calculated in Eq. (5.19). After that, a length scale parameter increment $\Delta\ell$ is sensitively defined to provide the dynamic response of periodic laminates for a comprehensive range of geometric and material properties. The response of the dynamic gradient elasticity model is solved for each value of the dynamic length scale parameter. On the other hand, the associated heterogeneous model is also solved by the direct numerical simulation (DNS) to compare the response of the models. As a result, the displacement profiles are obtained from both the gradient elasticity model and the heterogeneous model.

The best fit in the displacement curves of the gradient elasticity model is selected by the error estimation obtained by a trapezoidal integration of the displacement curves between the gradient elasticity and heterogeneous model. The error estimation formula is given by

$$\epsilon_{\mathrm{A}}(\%) = \frac{\displaystyle\int_0^L f_{\mathrm{hete}}(x)\,\mathrm{d}x - \int_0^L f_{\mathrm{grad}}(x)\,\mathrm{d}x}{\displaystyle\int_0^L f_{\mathrm{hete}}(x)\,\mathrm{d}x} \cdot 100 = \frac{\displaystyle\sum_{n=1}^{N} \Big|\, f_{\mathrm{hete}}(x_{\mathrm{n}}) - f_{\mathrm{grad}}(x_{\mathrm{n}}) \,\Big|}{\displaystyle\sum_{n=1}^{N} \Big| f_{\mathrm{hete}}(x_{\mathrm{n}}) \Big|} \cdot 100 \tag{5.20}$$

where N is the total number of evenly spaced intervals. When the minimum error between the displacement curves is higher than 5%, the dynamic length scale parameter increment $\Delta\ell_{\mathrm{d}}$ is reduced to increase the sensitivity of the response of the gradient elasticity model. Once the minimum error is satisfied, the dynamic length scale parameter providing the minimum error is selected. Finally, the ratio of the dynamic length scale parameter to the static length scale parameter is presented.

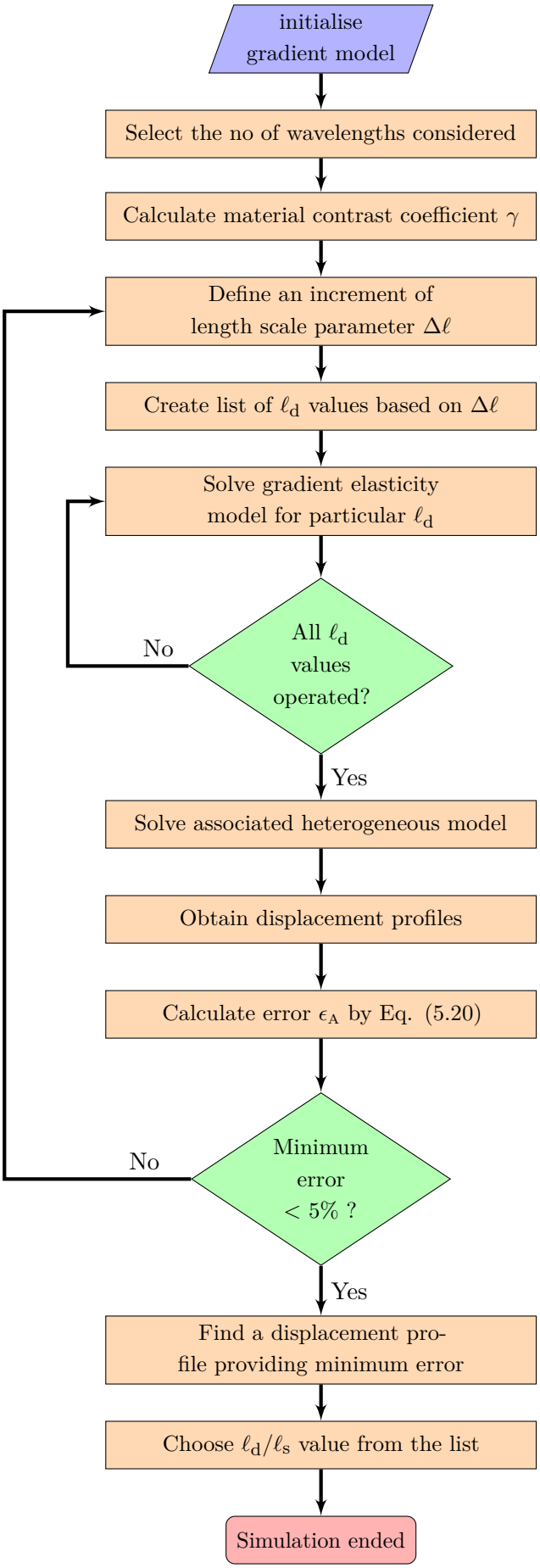

Fig. 5.4 Computational flowchart of selecting the dynamic length scale parameter ℓ_d

5.5 Numerical model implementation

The dynamically consistent gradient model presented for a one-dimensional laminated bar shown in Figure 5.2 is straightforwardly employed within the standard finite element method and the constant average acceleration time integration scheme. Eqs. (5.9) and (5.10), formed as a coupled system of equations, can be partitioned into updates of microscopic and macroscopic displacement with associated microscopic and macroscopic acceleration, respectively. In order to discretise the coupled system of equations with its variationally consistent boundary conditions, the weak form of Eq. (5.9) can be elaborated as

$$\int_0^L \delta u\, \rho \left(\frac{\ell_\mathrm{d}^2}{\ell_\mathrm{s}^2} \ddot{u}_\mathrm{m} - \frac{\ell_\mathrm{d}^2 - \ell_\mathrm{s}^2}{\ell_\mathrm{s}^2} \ddot{u}_\mathrm{M} \right) \mathrm{d}x - \int_0^L \delta u\, E \frac{\partial^2 u_\mathrm{m}}{\partial x^2}\, \mathrm{d}x = 0 \tag{5.21}$$

δu is a virtual displacement. Using integration by parts for the last term of Eq. (5.21) to bring derivative to δu gives

$$\int_0^L \delta u\, \rho \left(\frac{\ell_\mathrm{d}^2}{\ell_\mathrm{s}^2} \ddot{u}_\mathrm{m} - \frac{\ell_\mathrm{d}^2 - \ell_\mathrm{s}^2}{\ell_\mathrm{s}^2} \ddot{u}_\mathrm{M} \right) \mathrm{d}x + \int_0^L \delta\varepsilon\, E\, \varepsilon_\mathrm{m}\, \mathrm{d}x = \int_0^L \delta u\, t\, \mathrm{d}x \tag{5.22}$$

where t is the prescribed tractions associated with the stiffness traction in Eq. (5.7) according to the variationally consistent boundary condition [72]. Taking the weak form of Eq. (5.10) gives

$$\int_0^L \delta u\, \rho \left(-\frac{\ell_\mathrm{d}^2 - \ell_\mathrm{s}^2}{\ell_\mathrm{s}^2} \ddot{u}_\mathrm{m} + \frac{\ell_\mathrm{d}^2 - \ell_\mathrm{s}^2}{\ell_\mathrm{s}^2} \ddot{u}_\mathrm{M} - \left(\ell_\mathrm{d}^2 - \ell_\mathrm{s}^2\right) \frac{\partial^2 \ddot{u}_\mathrm{M}}{\partial x^2} \right) \mathrm{d}x = 0 \tag{5.23}$$

Integrating the last term of Eq. (5.23) by parts leads to the following equation:

$$\int_0^L \delta u\, \rho \left(-\frac{\ell_\mathrm{d}^2 - \ell_\mathrm{s}^2}{\ell_\mathrm{s}^2} \ddot{u}_\mathrm{m} + \frac{\ell_\mathrm{d}^2 - \ell_\mathrm{s}^2}{\ell_\mathrm{s}^2} \ddot{u}_\mathrm{M} \right) \mathrm{d}x + \int_0^L \frac{\partial \delta u}{\partial x} \rho \left(\ell_\mathrm{d}^2 - \ell_\mathrm{s}^2\right) \frac{\partial u_\mathrm{M}}{\partial x}\, \mathrm{d}x - \left[\delta u \rho \left(\ell_\mathrm{d}^2 - \ell_\mathrm{s}^2\right) \frac{\partial u_\mathrm{M}}{\partial x} \right]_0^\mathrm{L} = 0 \tag{5.24}$$

The boundary integral resulting from the integration by parts is cancelled out according to the variationally consistent boundary condition since the inertia traction in Eq. (5.8) is assumed as zero [72]. Eventually, Eqs. (5.22) and (5.24) can be rewritten in a matrix-vector form as

$$\begin{bmatrix} M_\mathrm{mm} & -M_\mathrm{mM} \\ -M_\mathrm{mM}^T & M_\mathrm{MM} \end{bmatrix} \begin{bmatrix} \ddot{u}_\mathrm{m} \\ \ddot{u}_\mathrm{M} \end{bmatrix} + \begin{bmatrix} K_\mathrm{mm} & 0 \\ 0 & 0 \end{bmatrix} \begin{bmatrix} u_\mathrm{m} \\ u_\mathrm{M} \end{bmatrix} = \begin{bmatrix} f_\mathrm{ext} \\ 0 \end{bmatrix} \tag{5.25}$$

Corresponding mass, stiffness and external body force matrices containing length scale parameters are listed below

$$M_{\mathrm{mm}} = \int_0^L N^T \rho \frac{\ell_{\mathrm{d}}^2}{\ell_{\mathrm{s}}^2} N \,\mathrm{d}x \tag{5.26}$$

$$M_{\mathrm{mM}} = \int_0^L N^T \rho \frac{\ell_{\mathrm{d}}^2 - \ell_{\mathrm{s}}^2}{\ell_{\mathrm{s}}^2} N \,\mathrm{d}x \tag{5.27}$$

$$M_{\mathrm{MM}} = \int_0^L N^T \rho \frac{\ell_{\mathrm{d}}^2 - \ell_{\mathrm{s}}^2}{l_{\mathrm{s}}^2} N \,\mathrm{d}x + \int_0^L \frac{\partial N^T}{\partial x} \rho \left(\ell_{\mathrm{d}}^2 - \ell_{\mathrm{s}}^2\right) \frac{\partial N}{\partial x} \,\mathrm{d}x \tag{5.28}$$

$$K_{\mathrm{mm}} = \int_0^L B^T E B \,\mathrm{d}x \tag{5.29}$$

$$f_{\mathrm{ext}} = \int_0^L N^T t \,\mathrm{d}x \tag{5.30}$$

The consistent element matrices for one-dimensional problems, which include length scale parameters, are provided as follows:

$$M_{\mathrm{mm}} = \rho h \frac{\ell_{\mathrm{d}}^2}{\ell_{\mathrm{s}}^2} \begin{bmatrix} \frac{1}{3} & \frac{1}{6} \\ \frac{1}{6} & \frac{1}{3} \end{bmatrix} \tag{5.31}$$

$$M_{\mathrm{mM}} = \rho h \frac{\ell_{\mathrm{d}}^2 - \ell_{\mathrm{s}}^2}{\ell_{\mathrm{s}}^2} \begin{bmatrix} \frac{1}{3} & \frac{1}{6} \\ \frac{1}{6} & \frac{1}{3} \end{bmatrix} \tag{5.32}$$

$$M_{\mathrm{MM}} = \rho h \frac{\ell_{\mathrm{d}}^2 - l_{\mathrm{s}}^2}{\ell_{\mathrm{s}}^2} \begin{bmatrix} \frac{1}{3} & \frac{1}{6} \\ \frac{1}{6} & \frac{1}{3} \end{bmatrix} + \rho \frac{\ell_{\mathrm{d}}^2 - \ell_{\mathrm{s}}^2}{h} \begin{bmatrix} 1 & -1 \\ -1 & 1 \end{bmatrix} \tag{5.33}$$

$$K_{\mathrm{mm}} = \frac{E}{h} \begin{bmatrix} 1 & -1 \\ -1 & 1 \end{bmatrix} \tag{5.34}$$

Typically, a lumped mass matrix is the favoured choice, especially for explicit time integration schemes. However, a consistent mass matrix is implemented for gradient analyses since a mass lumping process will result in cancelling the gradient effects.

5.6 Numerical results

The one-dimensional periodic laminate bar shown in Figure 5.2 is adopted to scrutinize the quantification of the dynamic length scale parameter for several numerical examples. The length of the one-dimensional periodic bar is $L = 300$ m with the unit cells of constant size $\ell = 1$ m and the cross-sectional area of $A = 1$ m^2. Each unit cell consists of two layers, where the first material is assigned Young's modulus E_1, mass density ρ_1 and elastic impedance $z_1 = \sqrt{E_1\rho_1}$, while corresponding material properties for the second are denoted as E_2, ρ_2 and $z_2 = \sqrt{E_2\rho_2}$. The material properties are chosen for various impedance contrasts z_1/z_2, the contrast levels of which are assigned as low $z_1/z_2 = 10$, intermediate $z_1/z_2 = 100$ and high $z_1/z_2 = 1000$. Constant volume fractions of the two materials are taken via $\alpha = 0.5$ along the bar, resulting in the equal size of the laminates $h_1 = h_2 = \frac{\ell}{2}$. The bar is constrained on the right end and subjected to a unit-pulse $f_0 = 1$ N on the left end at the beginning of analyses.

In the numerical examples, the one-dimensional periodic laminate bar is simulated by a homogeneous equivalent material with averaged (i.e. *effective*) material properties, a gradient elasticity model with length scales and a heterogeneous model by the DNS. The material properties of the homogeneous model are obtained from averaged Young's modulus E_{avr} and mass density ρ_{avr} in Eqs. (3.17) and (3.18). The constant average acceleration scheme is used with time step sizes of 0.05 s for the homogeneous and heterogeneous models as well as 0.2 s for the gradient elasticity model. In Appendix B, all physical and numerical parameters are listed.

5.6.1 Effect of ℓ_d on dispersion behaviour

Firstly, the effect of the dynamic length scale parameter ℓ_{d} on the dispersive behaviour of the periodic laminate bar is investigated. The dispersive characteristics are simulated by the gradient elasticity model for various dynamic length scale parameters such as $\ell_{\text{d}} = 2, 4, 6$. The static length scale parameter calculated using Eq. (5.16) remains the same for all analyses due to the regular unit cell size ℓ along the bar.

The displacement curves along the bar are presented for various ratios of the dynamic length scale parameter to the static length scale parameter in Figure 5.5. When the length scale parameters equal to $\ell_{\text{d}} = \ell_{\text{s}} = 0$, the wavefront becomes non-dispersive so that the angle of the wavefront approaches 90°. All wave numbers k in this non-dispersive homogeneous model travel with the same phase velocity c_{p}. Despite the absence of physical dispersion, a modest level of numerical dispersion can be detected in the homogeneous displacement curve due to spatial and temporal discretisation. On the other hand, when the dynamic and static length scale parameters appear in the gradient elasticity model, wave propagation becomes

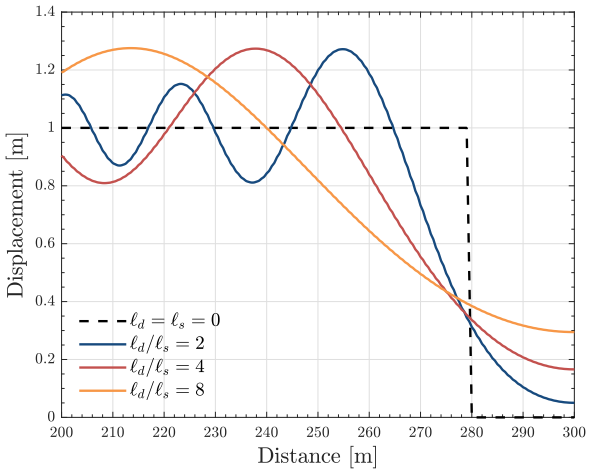

Fig. 5.5 Role of ℓ_{d} in dispersion behaviour simulated by the gradient elasticity theory - displacement curves for the periodic laminate bar at time $t = 280$s.

dispersive, arising from changes in the phase velocities based on their wavelengths. Increases in the ratio $\ell_{\mathrm{d}}/\ell_{\mathrm{s}}$ give rise to increases in its distance between successive peaks.

5.6.2 Effect of various impedance contrasts on ℓ_{d}

Length scale parameters tend to increase with increases in the material contrast between components of composite materials. Apart from the static length scale parameter related directly to the unit cell size, the quantification of the dynamic length scale parameter is investigated for the contrast in the mechanical impedance of materials in this section. The numerical simulations are implemented for the low, intermediate and high contrasts levels quantified as $z_1/z_2 = 10$, $z_1/z_2 = 100$ and $z_1/z_2 = 1000$, respectively. The selection of the dynamic length scale parameter is implemented according to the numerical scheme presented in Figure 5.4.

In Figure 5.6, displacement curves through the bar are shown for three impedance contrast levels in the material to determine the best value of the dynamic length scale parameter. As expected, the response of the periodic laminate by the equivalent homogeneous model provides non-dispersive wave profiles. In gradient elasticity simulations, the first peak of the displacement curves obtained with the analytical dynamic length scale parameter of Eq. (5.18) have relatively satisfying dispersion estimations. Nevertheless, the differences between the response received with the analytical dynamic length scale parameter and the heterogeneous model become more pronounced in successive peaks. The displacement curves of the intermediate and high impedance contrasts deviate from the heterogeneous solution by the DNS more than the low impedance contrast. On the other hand, the displacement curves obtained with the dynamic length scale parameter estimated by [3] provide dispersive wave

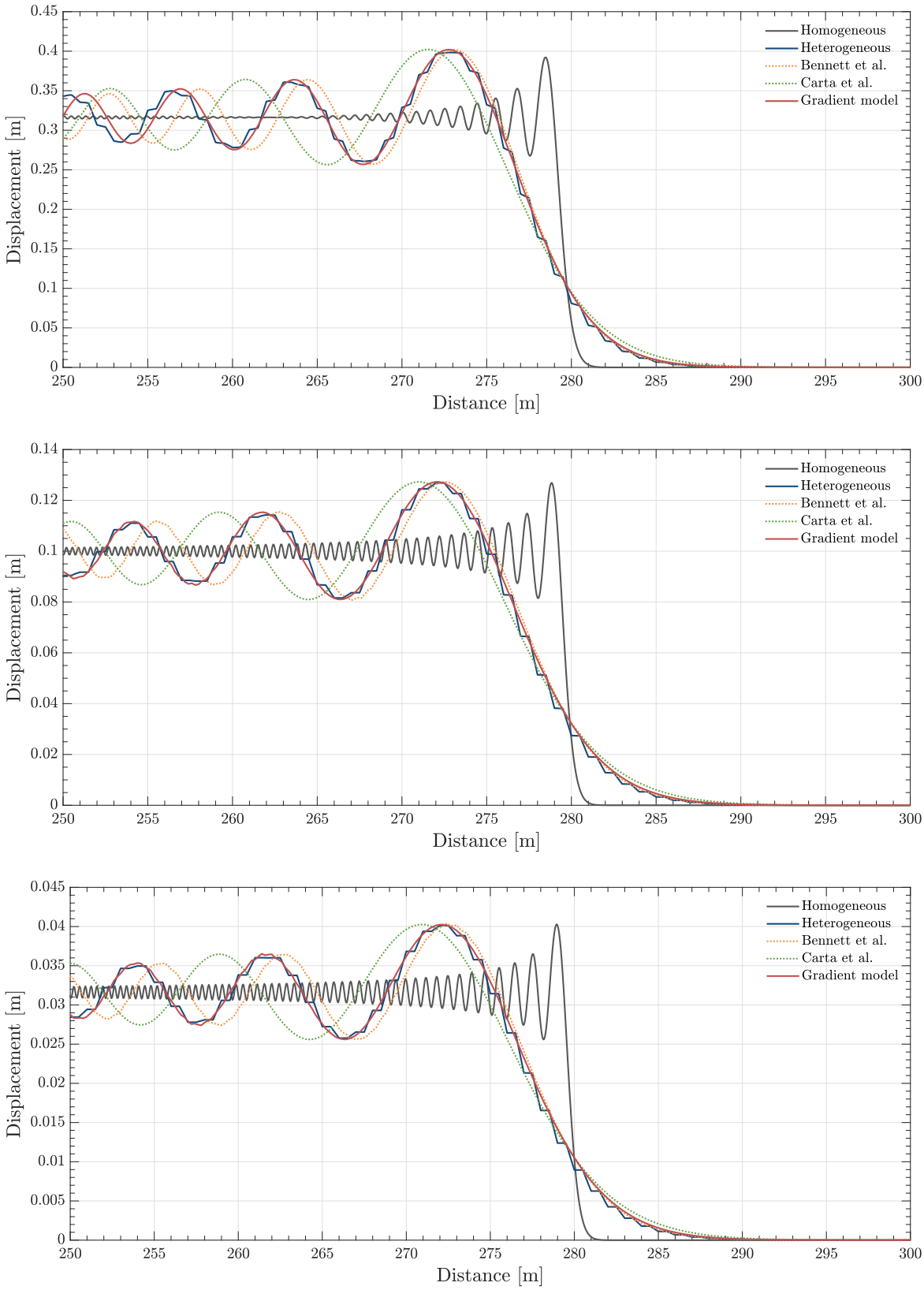

Fig. 5.6 Displacement profiles of the periodic laminate bar with low contrast $z_1/z_2 = 10$ (top), intermediate contrast $z_1/z_2 = 100$ (middle) and high contrast $z_1/z_2 = 1000$ (bottom) at the time $t = 280$ s. The bar simulated is with homogeneous (dark grey line), heterogeneous (blue line), gradient model with ℓ_d derived analytically [2] (dotted orange line), gradient model with ℓ_d estimated numerically [3] (dotted green line) and gradient model with the improved ℓ_d presented in Figure (5.4) (red line).

characteristics, yet the difference from the heterogeneous response is considerably higher than other gradient elasticity models.

As depicted in Figure 5.6, for all contrast levels in the material, the proposed dynamic length scale parameter is slightly higher than the analytical dynamic length scale parameter, while the proposed dynamic length scale parameter is considerably lower than the dynamic length scale parameter estimated by [3]. Moreover, the deviations from the response obtained with the analytical dynamic length scale parameter and the dynamic length scale parameter estimated by [3] slightly increase with increasing the impedance factor z. On the other hand, the numerical estimations of the proposed dynamic length scale parameter compared to the heterogeneous benchmark solutions have satisfying trends for all impedance contrast levels.

5.6.3 Comparison of $\ell_{\mathrm{d}}/\ell_{\mathrm{s}}$ with different methods

In the previous section, it is presented that quantifying the dynamic length scale parameter requires improvement to model the dispersive characteristics of periodic laminates based on material contrasts. Therefore, the effect of the contrast in mechanical impedance of materials on $\ell_{\mathrm{d}}/\ell_{\mathrm{s}}$ is examined to formulate the dynamic length scale parameter in this section. A series of gradient elasticity numerical simulations are conducted to determine the dynamic length scale parameters for a wide range of material contrast in the one-dimensional periodic laminate bar. The procedure of selecting the dynamic length scale parameter presented in Figure 5.4 is pursued in all simulations. After the convergence of $\ell_{\mathrm{d}}/\ell_{\mathrm{s}}$ against time, the ratio $\ell_{\mathrm{d}}/\ell_{\mathrm{s}}$ is determined based on displacement profiles at the mid-point of the bar.

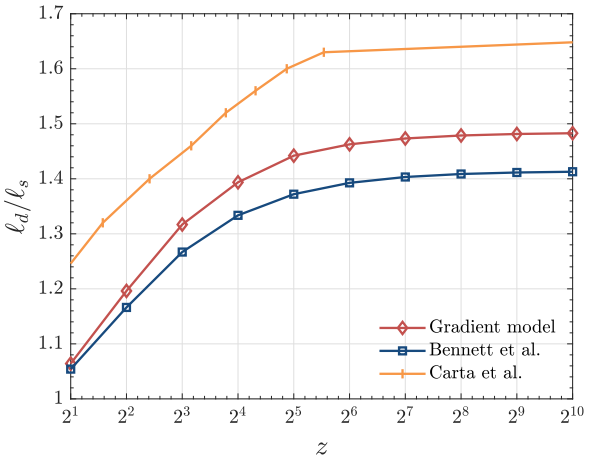

Fig. 5.7 The ratio $\ell_{\mathrm{d}}/\ell_{\mathrm{s}}$ versus a wide range of impedance contrast levels of the material in the periodic laminate bar, simulated by various gradient elasticity approximations.

The normalised dynamic length scale parameters obtained from various gradient elasticity approximations are demonstrated in Figure 5.7. The gradient elasticity approximations shown

in Figure 5.7 indicate a correlation between the dynamic length scale parameter and the impedance contrasts. Even though there is a remarkably similar trend for impedance contrasts among the approximations, the value of the proposed dynamic length scale parameters is larger than the value of the analytical dynamic length scale parameters and smaller than the value of the dynamic length scale parameters provided by Carta *et al.* [3]. The proposed numerical dynamic length scale parameter is formulated based on contrasts in periodic laminates according to the data represented in Figure 5.7, that gives

$$\frac{\ell_{\mathrm{d}}}{\ell_{\mathrm{s}}} = -0.72\left(\frac{z_1}{z_2}\right)^{-0.66} + 1.5 \tag{5.35}$$

5.7 Discussion

The quantification of the dynamic length scale parameter is examined in this chapter for one-dimensional periodic laminate problems simulated by a gradient elasticity theory. This requires curve fitting optimisation of displacement profiles obtained from the dynamically consistent gradient elasticity model. In order to provide a benchmark solution, the one-dimensional periodically laminated bar is simulated by direct numerical simulation. The procedure is applied to a wide range of contrasts in the material so that the dynamic length scale parameter is formulated as a result of the response of the gradient elasticity model.

The gradient elasticity model is numerically computed as a function of the dynamic length scale parameter for various material properties. As anticipated, the dynamic length scale parameter is larger than the static length scale parameter. The ratio of the dynamic length scale parameter to the static length scale parameter also increases with increase in contrasts in the material. It is detected that the optimum value of the dynamic length scale parameter lies between the values acquired by two earlier gradient elasticity approximations despite approaching the relatively same convergence characteristics. For high impedance contrast levels, the material response obtained from the numerical dynamic length scale parameter is more robust in ongoing wave propagation than the analytical dynamic length scale parameter.

There are some differences in the dynamic length scales obtained using the averaging technique outlined in Chapter 3 and the gradient elasticity method described in this Chapter. Particularly, the normalised dynamic RVE size is approximately 10 times larger than the ratio of the dynamic length scale parameter to the static length scale parameter. In Chapter 3, a microstructural boundary value problem is solved to obtain the macroscopic material properties, whereas in the gradient elasticity theory a macrostructural boundary value problem is solved with additional length scales. The gradient elasticity is based on Taylor expansion with truncation errors which can be reduced by increasing the number of

higher-order terms in Taylor expansion. In contrast, homogenisation techniques rely on the separation of length and time scales to loosen the restriction on coupling between macro and microscales, leading to a significant reduction in error.

Chapter 6

Conclusions and future perspectives

6.1 Conclusions

The focus of this thesis is to quantify dynamic length and time scales and establish their relations to facilitate the modelling of the material behaviour of periodic composites in dynamics for practical engineering applications. The conclusions of the thesis can be summarized concisely as the outcomes listed in the same order as the chapters:

1. As an extension of Hill-Mandel principle of macrohomogeneity, the time averaging has been derived in addition to the space averaging with the finite element method for dynamic micro-macro averaging. The macroscopic material properties have been normalised by the averaged analytical material properties, widely used in literature to validate the macroscopic material properties of 1D periodic composites. The results have demonstrated a significant improvement in the estimation of homogenized material properties when using the space-time averaging approach compared to the space averaging alone.

2. The effect of microscale boundary conditions on predicting macroscopic material properties within the micro-macro averaging relations has been evaluated. Similar to the findings in statics, the use of periodic boundary conditions outperforms Dirichlet boundary conditions, particularly in estimating macroscopic mass densities in a transient dynamic context.

3. The findings in this thesis confirms that the size of the representative volume element (RVE) in dynamics is larger than that in statics as previously reported in current literature. The quantification of the RVE size in dynamics was investigated by increasing the number of unit cells and wave propagations at the microscale. The simultaneous increase in the number of unit cells and the wave propagations resulted in a more effective convergence of macroscopic material properties than when each of these was individually increased.

4. The proposed space-time averaging approach was assessed for various material impedance contrasts and volume fractions to validate its effectiveness further for real-world engineering applications. The results showed that higher impedance contrasts and volume fractions in the material converged at larger RVE sizes as well as larger time windows.

5. The issue of requiring a sufficiently large RVE size and time window has also been addressed for dynamic computational homogenisation methods. The work in this thesis achieved by implementing the separation of time scales between macro and microstructures, along with the separation of length scales, within the dynamic computational homogenisation framework. The effectiveness of this approach has been verified by comparing the macroscopic results with the solutions of the direct numerical simulation for a one-dimensional periodically laminate bar.

6. The temporal decoupling of the homogenised macrostructure from its microstructure has enabled to extend the time window of microstructural analyses until the macroscopic response become independent from microscopic variations. This required the reformulation of scale transitions between macro and microstructures with new time integration parameters in this work.

7. The efficacy of the dynamic computational homogenisation model, incorporating both the separation of length and time scales, was evaluated on the dynamic response of the one-dimensional bar. Increasing the number of unit cells improved the estimation of multiscale strain energy, while increasing the number of wave propagations improved the estimation of multiscale kinetic energy. The simultaneous increase in the numbers of unit cells and wave propagations yielded the best results in predicting the macroscopic displacement.

8. The influence of the simultaneous increase in the number of unit cells and wave propagations has been examined on the contrast in mechanical impedance of materials. A consistent trend for the convergence of the macroscopic displacements and energies was observed at different contrast levels. However, the accuracy of the macroscopic response highly reduced at high contrast levels, as expected.

9. The microstructural boundary value problem was solved using both implicit and explicit time integration methods, and the performance of each method has been evaluated for different material impedance contrasts. The results indicated that the explicit time integration method shows better convergence with the direct numerical simulation results for low impedance contrast levels, while the implicit time integration method outperforms the explicit method for moderately high impedance contrast levels.

10. This thesis has addressed the challenge of quantifying the dynamic length scale parameter in gradient elasticity theories by leveraging advancements in dynamic RVE size within

homogenisation methods. The curve fitting optimization approach was proposed to calibrate the dynamic length scale parameter with the size of RVE in dynamics. The resulting displacement profiles have enabled a comparison with dynamic length scale parameters derived analytically and numerically in the literature.

11. The proposed curve fitting optimisation approach demonstrated a consistent trend across a wide range of material impedance contrasts. The equation of the dynamic length scale parameter was presented in relation to the material impedance contrast and the RVE size.

12. The findings of length scales in both dynamic homogenisation and gradient elasticity methods showed that length scales increased under dynamic excitation when compared with those in statics. The change in length scales resulted in a more significant reduction in error for homogenisation methods in comparison to gradient elasticity methods.

6.2 Future perspectives

Several promising potentials for future considerations have emerged throughout this work:

Further microstructural geometries The proposed approaches in multiscale methods were implemented on one-dimensional periodically laminated composites. In order to extend the feasibility of the developments presented in this thesis to engineering applications, it would be necessary to implement them on a range of different microstructural designs. This would facilitate a more comprehensive assessment of the effectiveness and practicality of the proposed methods. Firstly, the methodologies presented in this thesis for one-dimensional applications would expand to three-dimensional scenarios, following the mathematical formulation provided in the literature. On the other hand, the application of these developed methods in this thesis is not limited to periodic laminates; their potential extends to cutting-edge materials such as metamaterials. Incorporating metamaterials into the evaluation process can lead to groundbreaking advancements in various fields, including optics, acoustics, and electromagnetics.

Temporal averaging in computational homogenisation The upscaling in the computational homogenisation system is formed by spatially averaging results of microstructural boundary value problems according to the Hill-Mandel principle. The temporal averaging as an extension of the Hill-Mandel principle introduced in this thesis could be performed within the computational homogenisation framework. The space-time averaging would highly likely improve the macroscopic response obtained from the averaged results of microstructural boundary value problems.

Temporal scales in gradient elasticity The dynamically consistent gradient elasticity model for determining the dynamic length scale parameter is based on a Taylor expansion in space, which only involves length scales. However, Askes *et al.* [109] introduced a gradient elasticity model with time scales to improve the accuracy of predicting material behaviour in dynamic problems. Quantifying time scale parameters would be as significant as quantifying the length scale parameters, as it can affect the performance of the gradient elasticity model on the macroscopic response of the material.

Scale separations for frequency domain boundary value problems Recent attempts have been made to expand the use of frequency domain boundary value problems in multiscale problems, despite the limitation of their applicability to linear elastic materials [66, 110]. For instance, Sridhar *et al.* [66] have explored the improved separation of length scale approach at higher frequencies, where the classical scale separation fails. However, the classical scale separation method is no longer practical in higher frequency regimes. Due to the fact that energy consistency has not achieved between the scales in frequency domain, further research should be required. The separation of length and time scales presented in this thesis could contribute to frequency domain analyses for multiscale problems.

References

[1] W. D. C. Jr. and D. G. Rethwisch, *Materials Science and Engineering: An Introduction*, 10th ed. John Wiley & Sons, 1997.

[2] T. Bennett, I. M. Gitman, and H. Askes, "Elasticity theories with higher-order gradients of inertia and stiffness for the modelling of wave dispersion in laminates," *International Journal of Fracture*, vol. 148, pp. 185–193, 2007.

[3] G. Carta and M. Brun, "A Dispersive Homogenization Model Based on Lattice Approximation for the Prediction of Wave Motion in Laminates," *Journal of Applied Mechanics*, vol. 79, no. 2, 2012, 021019.

[4] K. Matouš, M. G. D. Geers, V. G. Kouznetsova, and A. Gillman, "A review of predictive nonlinear theories for multiscale modeling of heterogeneous materials," *Journal of Computational Physics*, vol. 330, pp. 192–220, 2017.

[5] R. W. Bruce, *Handbook of Lubrication and Tribology, Volume II: Theory and Design*, 2nd ed. CRC Press, 2012.

[6] A. Borbély, H. Biermann, and O. Hartmann, "FE investigation of the effect of particle distribution on the uniaxial stress–strain behaviour of particulate reinforced metal-matrix composites," *Materials Science and Engineering: A*, vol. 313, pp. 34–45, 2001.

[7] M. Stroeven, H. Askes, and L. J. Sluys, "Numerical determination of representative volumes for granular materials," *Computer Methods in Applied Mechanics and Engineering*, vol. 193, pp. 3221–3238, 2004, computational Failure Mechanics.

[8] N. Chawla, R. S. Sidhu, and V. V. Ganesh, "Three-dimensional visualization and microstructure-based modeling of deformation in particle-reinforced composites," *Acta Materialia*, vol. 54, pp. 1541–1548, 2006.

[9] G. Gantzounis, M. Serra-Garcia, K. Homma, J. M. Mendoza, and C. Daraio, "Granular metamaterials for vibration mitigation," *Journal of Applied Physics*, vol. 114, p. 093514, 2013.

[10] E. Kim, J. Yang, H. Hwang, and C. W. Shul, "Impact and blast mitigation using locally resonant woodpile metamaterials," *International Journal of Impact Engineering*, vol. 101, pp. 24–31, 2017.

[11] C. González and J. LLorca, "Multiscale modeling of fracture in fiber-reinforced composites," *Acta Materialia*, vol. 54, pp. 4171–4181, 2006.

[12] I. Giorgio, A. Ciallella, and D. Scerrato, "A study about the impact of the topological arrangement of fibers on fiber-reinforced composites: Some guidelines aiming at the development of new ultra-stiff and ultra-soft metamaterials," *International Journal of Solids and Structures*, vol. 203, pp. 73–83, 2020.

[13] D. Meng, T. Huang, Y. X. Zhang, and C. K. Lee, "Mechanical behaviour of a polyvinyl alcohol fibre reinforced engineered cementitious composite (pva-ecc) using local ingredients," *Construction and Building Materials*, vol. 141, pp. 259–270, 2017.

[14] A. O. Krushynska, A. Amendola, F. Bosia, C. Daraio, N. M. Pugno, and F. Fraternali, "Accordion-like metamaterials with tunable ultra-wide low-frequency band gaps," *New Journal of Physics*, vol. 20, no. 7, p. 073051, 2018.

[15] Y. Song, I. M. Gitman, W. J. Parnell, and H. Askes, "The influence of random microstructure on wave propagation through heterogeneous media," *International Journal of Fracture*, vol. 204, pp. 115–120, 2017.

[16] M. M. Ameen, R. H. J. Peerlings, and M. G. D. Geers, "A quantitative assessment of the scale separation limits of classical and higher-order asymptotic homogenization," *European Journal of Mechanics - A/Solids*, vol. 71, pp. 89–100, 2018.

[17] R. Car and M. Parrinello, "Unified approach for molecular dynamics and density-functional theory," *Physical Review Letters*, vol. 55, p. 2471 – 2474, 1985.

[18] E. B. Tadmor, M. Ortiz, and R. Phillips, "Quasicontinuum analysis of defects in solids," *Philosophical Magazine A: Physics of Condensed Matter, Structure, Defects and Mechanical Properties*, vol. 73, p. 1529 – 1563, 1996.

[19] E. Weinan and B. Engquist, "The heterogeneous multiscale methods," *Communications in Mathematical Sciences*, vol. 1, p. 87 – 132, 2003.

[20] I. G. Kevrekidis, C. W. Gear, J. M. Hyman, P. G. Kevrekidis, O. Runborg, and C. Theodoropoulos, "Equation-free, coarse-grained multiscale computation: Enabling microscopic simulators to perform system-level analysis*," *Communications in Mathematical Sciences*, vol. 1, p. 715 – 762, 2003.

[21] A. Bensoussan, J.-L. Lions, and G. Papanicolaou, *Asymptotic Analysis for Periodic Structures*. Amsterdam: North-Holland, 1978.

[22] A. Brandt, "Multi-level adaptive solutions to boundary-value problems," *Mathematics of Computation*, vol. 31, p. 333 – 390, 1977.

[23] E. Weinan, B. Engquist, X. Li, R. Weiqing, and E. Vanden-Eijnden, "Heterogeneous multiscale methods: A review," *Communications in Computational Physics*, vol. 2, no. 3, pp. 367–450, 2007.

[24] W. J. Drugan and J. R. Willis, "A micromechanics-based nonlocal constitutive equation and estimates of representative volume element size for elastic composites," *Journal of the Mechanics and Physics of Solids*, vol. 44, no. 4, pp. 497–524, 1996.

[25] R. Hill, "Elastic properties of reinforced solids: Some theoretical principles," *Journal of the Mechanics and Physics of Solids*, vol. 11, no. 5, pp. 357–372, 1963.

[26] M. Ostoja-Starzewski, "Microstructural Randomness Versus Representative Volume Element in Thermomechanics ," *Journal of Applied Mechanics*, vol. 69, no. 1, pp. 25–35, 2001.

[27] T. Kanit, S. Forest, I. Galliet, V. Mounoury, and D. Jeulin, "Determination of the size of the representative volume element for random composites: statistical and numerical approach," *International Journal of Solids and Structures*, vol. 40, no. 13, pp. 3647–3679, 2003.

[28] Y. Liu, F. P. van der Meer, and L. J. Sluys, "A dispersive homogenization model for composites and its RVE existence," *Computational Mechanics*, vol. 65, p. 79 – 98, 2020.

[29] V. P. Nguyen, O. Lloberas-Valls, M. Stroeven, and L. J. Sluys, "On the existence of representative volumes for softening quasi-brittle materials – A failure zone averaging scheme," *Computer Methods in Applied Mechanics and Engineering*, vol. 199, pp. 3028–3038, 2010.

[30] I. M. Gitman, H. Askes, and L. J. Sluys, "Representative volume: Existence and size determination," *Engineering Fracture Mechanics*, vol. 74, no. 16, pp. 2518–2534, 2007.

[31] I. M. Gitman, H. Askes, and E. C. Aifantis, "The representative volume size in static and dynamic micro-macro transitions," *International Journal of Fracture*, vol. 135, pp. 3–9, 2005.

[32] I. M. Gitman, H. Askes, and E. C. Aifantis, "Gradient elasticity with internal length and internal inertia based on the homogenisation of a representative volume element," *Journal of the Mechanical Behavior of Materials*, vol. 18, no. 1, pp. 1–16, 2007.

[33] I. M. Gitman, H. Askes, and L. J. Sluys, "Coupled-volume multi-scale modelling of quasi-brittle material," *European Journal of Mechanics, A/Solids*, vol. 27, p. 302 – 327, 2008.

[34] P. Suquet, "Elements of homogenization theory for inelastic solid mechanics," *Homogenization Techniques for Composite Media*, pp. 193–279, 1987.

[35] W. Voigt, "Ueber die beziehung zwischen den beiden elasticitätsconstanten isotroper körper," *Annalen der Physik*, vol. 274, pp. 573–587, 1889.

[36] A. Reuss, "Berechnung der fließgrenze von mischkristallen auf grund der plastizitätsbedingung für einkristalle ." *Zamm-zeitschrift Fur Angewandte Mathematik Und Mechanik*, vol. 9, pp. 49–58, 1929.

[37] J. D. Eshelby, "The determination of the elastic field of an ellipsoidal inclusion, and related problems," *Proceedings of the Royal Society of London. Series A, Mathematical and Physical Sciences*, vol. 241, no. 1226, pp. 376–396, 1957.

[38] Z. Hashin, "Analysis of Composite Materials—A Survey," *Journal of Applied Mechanics*, vol. 50, no. 3, pp. 481–505, 1983.

[39] Z. Hashin and S. Shtrikman, "A variational approach to the theory of the elastic behaviour of multiphase materials," *Journal of the Mechanics and Physics of Solids*, vol. 11, no. 2, pp. 127–140, 1963.

[40] R. Hill, "A self-consistent mechanics of composite materials," *Journal of the Mechanics and Physics of Solids*, vol. 13, no. 4, pp. 213–222, 1965.

[41] S. Nemat-Nasser and M. Taya, "On effective moduli of an elastic body containing periodically distributed voids," *Quarterly of Applied Mathematics*, vol. 39, no. 1, pp. 43–59, 1981.

[42] Y. Chen and C. A. Schuh, "Analytical homogenization method for periodic composite materials," *Phys. Rev. B*, vol. 79, p. 094104, 2009.

[43] W. Chen and J. Fish, "A Dispersive Model for Wave Propagation in Periodic Heterogeneous Media Based on Homogenization With Multiple Spatial and Temporal Scales ," *Journal of Applied Mechanics*, vol. 68, no. 2, pp. 153–161, 2000.

[44] O. van der Sluis, P. Schreurs, and H. Meijer, "Homogenisation of structured elastoviscoplastic solids at finite strains," *Mechanics of Materials*, vol. 33, no. 9, pp. 499–522, 2001.

[45] J. Hohe and W. Becker, "Effective mechanical behavior of hyperelastic honeycombs and two-dimensional model foams at finite strain," *International Journal of Mechanical Sciences*, vol. 45, no. 5, pp. 891–913, 2003.

[46] E. Andreassen and C. S. Andreasen, "How to determine composite material properties using numerical homogenization," *Computational Materials Science*, vol. 83, pp. 488–495, 2014.

[47] P. M. Suquet, "Local and global aspects in the mathematical theory of plasticity," *Plasticity Today*, pp. 279–309, 1985.

[48] V. G. Kouznetsova, "Computational homogenization for the multi-scale analysis of multi-phase materials," Ph.D. dissertation, Mechanical Engineering, 2002.

[49] M. G. D. Geers, V. G. Kouznetsova, T. J. Massart, I. Özdemir, E. W. C. Coenen, W. A. M. Brekelmans, and R. H. J. Peerlings, "Computational homogenization of structures and materials." Giens, France: CSMA, 2009.

[50] M. G. D. Geers, V. G. Kouznetsova, and W. A. M. Brekelmans, "Multi-scale computational homogenization: Trends and challenges," *Journal of Computational and Applied Mathematics*, vol. 234, no. 7, pp. 2175–2182, 2010.

[51] V. G. Kouznetsova, M. G. D. Geers, and W. A. M. Brekelmans, "Multi-scale second-order computational homogenization of multi-phase materials: a nested finite element solution strategy," *Computer Methods in Applied Mechanics and Engineering*, vol. 193, no. 48-51, pp. 5525–5550, 2004.

[52] F. Feyel and J.-L. Chaboche, "FE^2 multiscale approach for modelling the elastoviscoplastic behaviour of long fibre SiC/Ti composite materials," *Computer Methods in Applied Mechanics and Engineering*, vol. 183, no. 3, pp. 309–330, 2000.

[53] V. P. Nguyen, M. Stroeven, and L. J. Sluys, "Multiscale failure modeling of concrete: Micromechanical modeling, discontinuous homogenization and parallel computations," *Computer Methods in Applied Mechanics and Engineering*, vol. 201-204, pp. 139–156, 2012.

[54] A. Abdulle and A. Nonnenmacher, "A short and versatile finite element multiscale code for homogenization problems," *Computer Methods in Applied Mechanics and Engineering*, vol. 198, no. 37, pp. 2839–2859, 2009.

[55] A. Abdulle and M. J. Grote, "Finite element heterogeneous multiscale method for the wave equation," *Multiscale Modeling and Simulation*, vol. 9, p. 766 – 792, 2011.

[56] R. Cimrman, V. Lukeš, and E. Rohan, "Multiscale finite element calculations in Python using SfePy," *Advances in Computational Mathematics*, vol. 45, p. 1897 – 1921, 2019.

[57] C. Liu and C. R. Romo, "Discrete averaging relations for micro to macro transition," *Journal of Applied Mechanics, Transactions ASME*, vol. 83, 2016.

[58] C. Miehe, J. Schröder, and M. Becker, "Computational homogenization analysis in finite elasticity: Material and structural instabilities on the micro- and macro-scales of periodic composites and their interaction," *Computer Methods in Applied Mechanics and Engineering*, vol. 191, p. 4971 – 5005, 2002.

[59] K. Terada, M. Hori, T. Kyoya, and N. Kikuchi, "Simulation of the multi-scale convergence in computational homogenization approaches," *International Journal of Solids and Structures*, vol. 37, p. 2285 – 2311, 2000.

[60] C. Miehe, J. Schröder, and J. Schotte, "Computational homogenization analysis in finite plasticity simulation of texture development in polycrystalline materials," *Computer Methods in Applied Mechanics and Engineering*, vol. 171, pp. 387–418, 1999.

[61] F. Su, F. Larsson, and K. Runesson, "Computational homogenization of coupled consolidation problems in micro-heterogeneous porous media," *International Journal for Numerical Methods in Engineering*, vol. 88, p. 1198 – 1218, 2011.

[62] A. Iltchev, V. Marcadon, S. Kruch, and S. Forest, "Computational homogenisation of periodic cellular materials: Application to structural modelling," *International Journal of Mechanical Sciences*, vol. 93, p. 240 – 255, 2015.

[63] V. Kouznetsova, M. G. D. Geers, and W. A. M. Brekelmans, "Multi-scale constitutive modelling of heterogeneous materials with a gradient-enhanced computational homogenization scheme," *International Journal for Numerical Methods in Engineering*, vol. 54, pp. 1235–1260, 2002.

[64] K. Pham, V. G. Kouznetsova, and M. G. D. Geers, "Transient computational homogenization for heterogeneous materials under dynamic excitation," *Journal of the Mechanics and Physics of Solids*, vol. 61, no. 11, pp. 2125–2146, 2013.

[65] T. F. van Nuland, P. B. Silva, A. Sridhar, M. G. D. Geers, and V. G. Kouznetsova, "Transient analysis of nonlinear locally resonant metamaterials via computational homogenization," *Mathematics and Mechanics of Solids*, vol. 24, no. 10, pp. 3136–3155, 2019.

[66] A. Sridhar, V. G. Kouznetsova, and M. G. D. Geers, "Frequency domain boundary value problem analyses of acoustic metamaterials described by an emergent generalized continuum," *Computational Mechanics*, vol. 65, no. 3, p. 789–805, 2020.

[67] E. C. Aifantis, "On the role of gradients in the localization of deformation and fracture," *International Journal of Engineering Science*, vol. 30, no. 10, pp. 1279–1299, 1992.

[68] A. C. Eringen, "On differential equations of nonlocal elasticity and solutions of screw dislocation and surface waves," *Journal of Applied Physics*, vol. 54, no. 9, pp. 4703–4710, 1983.

[69] H. Askes and E. C. Aifantis, "Gradient elasticity in statics and dynamics: An overview of formulations, length scale identification procedures, finite element implementations and new results," *International Journal of Solids and Structures*, vol. 48, no. 13, pp. 1962–1990, 2011.

[70] C. Q. Ru and E. C. Aifantis, "A simple approach to solve boundary-value problems in gradient elasticity," *Acta Mechanica*, vol. 101, no. 11, pp. 59–68, 1993.

[71] A. V. Metrikine and H. Askes, "One-dimensional dynamically consistent gradient elasticity models derived from a discrete microstructure: Part 1: Generic formulation," *European Journal of Mechanics - A/Solids*, vol. 21, no. 4, pp. 555–572, 2002.

[72] H. Askes, T. Bennett, and E. Aifantis, "A new formulation and $\mathscr{C}^0$-implementation of dynamically consistent gradient elasticity," *International Journal for Numerical Methods in Engineering*, vol. 72, pp. 111 – 126, 2007.

[73] D. De Domenico, H. Askes, and E. C. Aifantis, "Gradient elasticity and dispersive wave propagation: Model motivation and length scale identification procedures in concrete and composite laminates," *International Journal of Solids and Structures*, vol. 158, p. 176 – 190, 2019.

[74] T. Bennett and H. Askes, "Finite element modelling of wave dispersion with dynamically consistent gradient elasticity," *Computational Mechanics*, vol. 43, pp. 815 – 825, 2009.

[75] D. De Domenico and H. Askes, "Computational aspects of a new multi-scale dispersive gradient elasticity model with micro-inertia," *International Journal for Numerical Methods in Engineering*, vol. 109, p. 52 – 72, 2017.

[76] V. G. Kouznetsova, M. G. D. Geers, and W. A. M. Brekelmans, "Size of a representative volume element in a second-order computational homogenization framework," *International Journal for Multiscale Computational Engineering*, vol. 2, pp. 575–598, 2004.

[77] I. M. Gitman, H. Askes, and L. J. Sluys, "Representative volume size as a macroscopic length scale parameter," *Fracture Mechanics for Concrete and Concrete Structures*, pp. 483–489, 2004.

[78] R. Hill, "On constitutive macro-variables for heterogeneous solids at finite strain," *Proceedings of the Royal Society of London. A. Mathematical and Physical Sciences*, vol. 326, no. 1565, pp. 131–147, 1972.

[79] J. R. Willis, "Variational and related methods for the overall properties of composites," vol. 21, pp. 1–78, 1981.

[80] Z. Hashin, "Analysis of Composite Materials — A Survey," *Journal of Applied Mechanics*, vol. 50, no. 3, pp. 481–505, 1983.

[81] S. Nemat-Nasser, "Averaging theorems in finite deformation plasticity," *Mechanics of Materials*, vol. 31, no. 8, pp. 493–523, 1999.

[82] I. M. Gitman, M. B. Gitman, and H. Askes, "Quantification of stochastically stable representative volumes for random heterogeneous materials," *Archive of Applied Mechanics*, vol. 75, pp. 79–92, 2006.

[83] P. Sheng and C. T. Chan, "Classical wave localization and spectral gap materials," *Zeitschrift für Kristallographie - Crystalline Materials*, vol. 220, no. 9-10, pp. 757–764, 2005.

[84] S. Nemat-Nasser and M. Hori, *Micromechanics: Overall Properties of Heterogeneous Materials*, J. D. Achenbach, Ed.

[85] Z.-P. Wang and C. Sun, "Modeling micro-inertia in heterogeneous materials under dynamic loading," *Wave Motion*, vol. 36, no. 4, pp. 473–485, 2002.

[86] H. Nassar, Q.-C. He, and N. Auffray, "Willis elastodynamic homogenization theory revisited for periodic media," *Journal of the Mechanics and Physics of Solids*, vol. 77, pp. 158–178, 2015.

[87] J. Fish, V. Filonova, and S. Kuznetsov, "Micro-inertia effects in nonlinear heterogeneous media," *International Journal for Numerical Methods in Engineering*, vol. 91, pp. 1406–1426, 2012.

[88] A. Srivastava and S. Nemat-Nasser, "On the limit and applicability of dynamic homogenization," *Wave Motion*, vol. 51, no. 7, pp. 1045–1054, 2014.

[89] A. Srivastava, "Elastic metamaterials and dynamic homogenization: a review," *International Journal of Smart and Nano Materials*, vol. 6, no. 1, pp. 41–60, 2015.

[90] A. Sridhar, V. G. Kouznetsova, and M. G. D. Geers, "A general multiscale framework for the emergent effective elastodynamics of metamaterials," *Journal of the Mechanics and Physics of Solids*, vol. 111, pp. 414–433, 2018.

[91] E. A. de Souza Neto, P. J. Blanco, P. J. Sánchez, and R. A. Feijóo, "An rve-based multiscale theory of solids with micro-scale inertia and body force effects," *Mechanics of Materials*, vol. 80, pp. 136–144, 2015.

[92] C. Bagni, I. M. Gitman, and H. Askes, "A micro-inertia gradient visco-elastic motivation for proportional damping," *Journal of Sound and Vibration*, vol. 347, pp. 115–125, 2015.

[93] C. Reina Romo, "Multiscale modeling and simulation of damage by void nucleation and growth," Ph.D. dissertation, California Institute of Technology, 2011.

[94] J. Fish and W. Chen, "Uniformly valid multiple spatial-temporal scale modeling for wave propagation in heterogeneous media," *Mechanics of Composite Materials and Structures*, vol. 8, no. 2, pp. 81–99, 2001.

[95] I. V. Andrianov, V. I. Bolshakov, V. V. Danishevs'kyy, and D. Weichert, "Higher order asymptotic homogenization and wave propagation in periodic composite materials," *Proceedings of the Royal Society A: Mathematical, Physical and Engineering Sciences*, vol. 464, pp. 1181–1201, 2008.

[96] O. Van Der Sluis, P. J. G. Schreurs, W. A. M. Brekelmans, and H. E. H. Meijer, "Overall behaviour of heterogeneous elastoviscoplastic materials: Effect of microstructural modelling," *Mechanics of Materials*, vol. 32, p. 449 – 462, 2000.

[97] H. Moulinec and P. M. Suquet, "A numerical method for computing the overall response of nonlinear composites with complex microstructure," *Computer Methods in Applied Mechanics and Engineering*, vol. 157, no. 1, pp. 69–94, 1998.

[98] V. G. Kouznetsova, W. A. M. Brekelmans, and F. P. T. Baaijens, "An approach to micro-macro modeling of heterogeneous materials," *Computational Mechanics*, vol. 27, pp. 37–48, 2001.

[99] C. Liu and C. R. Romo, "Variational coarse-graining procedure for dynamic homogenization," *Journal of the Mechanics and Physics of Solids*, vol. 104, pp. 187–206, 2017.

[100] D. Roca, O. Lloberas-Valls, J. Cante, and J. Oliver, "A computational multiscale homogenization framework accounting for inertial effects: Application to acoustic metamaterials modelling," *Computer Methods in Applied Mechanics and Engineering*, vol. 330, pp. 415–446, 2018.

[101] H. T. Zhu, H. M. Zbib, and E. C. Aifantis, "Strain gradients and continuum modeling of size effect in metal matrix composites," *Acta Mechanica*, vol. 121, pp. 165–176, 1997.

[102] B. L. Karihaloo and Q. Z. Xiao, "Size effect in the strength of concrete structures," *Sadhana*, vol. 27, pp. 449–459, 2002.

[103] E. C. Aifantis, "Strain gradient interpretation of size effects," *International Journal of Fracture*, vol. 95, no. 299, p. 299–314, 1999.

[104] H. Askes, A. S. J. Suiker, and L. J. Sluys, "A classification of higher-order strain-gradient models – linear analysis," *Archive of Applied Mechanics*, vol. 72, pp. 171 – 188, 2002.

[105] R. D. Mindlin, "Micro-structure in linear elasticity," *Archive for Rational Mechanics and Analysis*, vol. 16, pp. 51–78, 1964.

[106] H. Askes and A. V. Metrikine, "One-dimensional dynamically consistent gradient elasticity models derived from a discrete microstructure: Part 2: Static and dynamic response," *European Journal of Mechanics - A/Solids*, vol. 21, no. 4, pp. 573–588, 2002.

[107] R. R. Peerlings, D. R. Borst, W. M. Brekelmans, de Jhp Henk Vree, and I. Spee, "Some observations on localisation in non-local and gradient damage models," *European Journal of Mechanics A-solids*, vol. 15, pp. 937–953, 1996.

[108] G. B. Whitham, *Linear and Nonlinear Waves*. John Wiley & Sons, Ltd, 1999.

[109] H. Askes, A. V. Metrikine, A. V. Pichugin, and T. Bennett, "Four simplified gradient elasticity models for the simulation of dispersive wave propagation," *Philosophical Magazine*, vol. 88, pp. 3415–3443, 2008.

[110] A. Sridhar, V. G. Kouznetsova, and M. G. D. Geers, "Homogenization of locally resonant acoustic metamaterials towards an emergent enriched continuum," *Computational Mechanics*, vol. 57, p. 423 – 435, 2016.

[111] J. Hetherington, A. Rodríguez-Ferran, and H. Askes, "The bipenalty method for arbitrary multipoint constraints," *International Journal for Numerical Methods in Engineering*, vol. 93, p. 465 – 482, 2013.

[112] H. Askes, S. Piercy, and S. Ilanko, "Tyings in linear systems of equations modelled with positive and negative penalty functions," *Communications in Numerical Methods in Engineering*, vol. 24, p. 1163 – 1169, 2008.

Appendix A

Numerical Methods

Time integration methods

In order to solve the equation of motion, time discretisation is required in addition to space discretisation. Therefore, a time integration method should be adopted with the finite element method. The Newmark time integration is employed in this section to achieve a solution for each time step. The equation of motion reads

$$M\ddot{u} + Ku = f_{\text{ext}} \tag{A.1}$$

where f_{ext} is the external force applied to the system. The displacement and velocity equations of Newmark time integration at time $t + \Delta t$ gives

$$u^{t+\Delta t} = u^t + \dot{u}^t \Delta t + \Big(\frac{1}{2} - \beta\Big)\Delta t^2 \ddot{u}^t + \beta \Delta t^2 (\ddot{u}^t + \Delta \ddot{u}) \tag{A.2}$$

$$\dot{u}^{t+\Delta t} = \dot{u}^t + (1-\gamma)\Delta t\, \ddot{u}^t + \gamma \Delta t\, \ddot{u}^{t+\Delta t} \tag{A.3}$$

where u^t, $\dot{u}$, and $\ddot{u}$ are displacements, velocities and accelerations discretised in time, and Δt is the time step. Also, β and γ are Newmark parameters to determine the accuracy and stability of the time integration. When Newmark constant coefficients are $\beta = 0.25$ and $\gamma = 0.5$, the time integration method becomes unconditionally stable, which is the so-called constant average acceleration scheme. On the other hand, when Newmark constant coefficients are $\beta = 0$ and $\gamma = 0.5$, the time integration method becomes conditionally stable with the critical time step. This method is equivalent to the so-called central difference method.

The constant average acceleration scheme

Rewriting Eq. (A.2) and Eq. (A.3) with Newmark constants $\beta = 0.25$ and $\gamma = 0.5$ gives

$$u^{t+\Delta t} = u^t + \dot{u}^t \Delta t + \frac{1}{4}\Delta t^2 \ddot{u}^t + \frac{1}{4}\Delta t^2 \ddot{u}^{t+\Delta t} \tag{A.4}$$

$$\dot{u}^{t+\Delta t} = \dot{u} + \frac{1}{2}\,\Delta t\,\ddot{u}^t + \frac{1}{2}\,\Delta t\,\ddot{u}^{t+\Delta t} \tag{A.5}$$

The constant average acceleration scheme solves the equation of motion to obtain the state of the system at time $t + \Delta t$, leading to

$$M\ddot{u}^{t+\Delta t} + Ku^{t+\Delta t} = f_{\text{ext}}^{t+\Delta t} \tag{A.6}$$

As an alternative, the increment form of Eq. (A.6) incorporates the displacement and acceleration at previous time t to update the solution incrementally over each time step. Thus,

$$M(\ddot{u}^t + \Delta\ddot{u}) + K(u^t + \Delta u) = f_{\text{ext}}^{t+\Delta t} \tag{A.7}$$

When Eq. (A.4) is also written in accordance with Eq. (A.7), that gives

$$\Delta u = \dot{u}^t \Delta t + \frac{1}{4}\Delta t^2 \ddot{u}^t + \frac{1}{4}\Delta t^2 (\ddot{u}^t + \Delta\ddot{u}) \tag{A.8}$$

Apart from the displacement calculation at time $t + \Delta t$, accelerations are also calculated at time $t + \Delta t$; hence, reorganising Eq. (A.8) to obtain the acceleration increment results in

$$\Delta\ddot{u} = \frac{4}{\Delta t^2}(\Delta u - \dot{u}^t \Delta t - \frac{1}{2}\Delta t^2 \ddot{u}^t) \tag{A.9}$$

The central difference method

Rewriting Eq. (A.2) and Eq. (A.3) with Newmark constants $\beta = 0$ and $\gamma = 0.5$ and shifting the time evaluation instants to include half-time steps gives

$$\dot{u}_f^{t+\frac{1}{2}\Delta t} = \dot{u}_f^{t-\frac{1}{2}} + \ddot{u}_f^t \Delta t \tag{A.10}$$

$$u^{t+\Delta t} = u^t + \dot{u}^t \Delta t + \frac{1}{2}\Delta t^2 \ddot{u}^t \tag{A.11}$$

Different from the constant average acceleration scheme, the central difference method expresses the equation of motion at current time t, namely

$$\ddot{u}^t = M^{-1}(f_{\text{ext}}^t - Ku^t) \tag{A.12}$$

Periodic boundary conditions

In this section, the equations of the bipenaly method [111] are presented to impose periodic boundary conditions on a one-dimensional periodic laminate bar. In the bipenalty method, displacement constraints are imposed together with the associated acceleration constraints for greater accuracy (and avoidance of problems with stability). The matrix form of the equation of motion at the microscale Eq. (3.1) is given by

$$Mu + K\ddot{u} = 0 \tag{A.13}$$

where M and K are the mass matrix and stiffness matrix of the microstructure. In order to impose a tying between degrees of freedom with subscripts L and R, the equation of constraints for displacements [112] is written as

$$\overline{u} = u_{\mathrm{L}} - u_{\mathrm{R}} \tag{A.14}$$

where $\overline{u}$ is the prescribed displacements at the boundary of the microstructure the constraint matrix describing the connections between degrees of freedom for each constraint. The displacement constraint is differentiated with respect to time to obtain the associated velocity constraint as follows

$$\dot{\overline{u}} = \dot{u}_{\mathrm{L}} - \dot{u}_{\mathrm{R}} \tag{A.15}$$

where $\dot{\overline{u}}$ is the prescribed velocities tying degrees of freedom subscripts L and R. The contributions of Eqs. (A.14) and (A.15) in the potential $\mathcal{U}$ and kinetic energies $\mathcal{K}$ gives

$$\mathcal{U} = \frac{1}{2}u^{\mathrm{T}}Ku + \frac{\alpha_{\mathrm{s}}}{2}(u_{\mathrm{L}} - u_{\mathrm{R}} - \overline{u})^2 \tag{A.16}$$

$$\mathcal{K} = \frac{1}{2}\dot{u}^{\mathrm{T}}M\dot{u} + \frac{\alpha_{\mathrm{m}}}{2}(\dot{u}_{\mathrm{L}} - \dot{u}_{\mathrm{R}} - \dot{\overline{u}})^2 \tag{A.17}$$

where α_{s} and α_{m} are the stiffness and mass penalty parameters. Hence, the equation of motions can be derived in the following form

$$(M + M^{\mathrm{p}})\ddot{u} + (K + K^{\mathrm{p}})u = f^{\mathrm{p}} \tag{A.18}$$

where K^{p} is zero matrix except for the elements that imposing a tying between L and R, which are $K^{\mathrm{p}}_{\mathrm{LL}} = K^{\mathrm{p}}_{\mathrm{RR}} = \alpha_{\mathrm{s}}$ and $K^{\mathrm{p}}_{\mathrm{LR}} = K^{\mathrm{p}}_{\mathrm{RL}} = -\alpha_{\mathrm{s}}$. Similarly, $M^{\mathrm{p}}_{\mathrm{LL}} = M^{\mathrm{p}}_{\mathrm{RR}} = \alpha_{\mathrm{m}}$ and $M^{\mathrm{p}}_{\mathrm{LR}} = M^{\mathrm{p}}_{\mathrm{RL}} = -\alpha_{\mathrm{m}}$, whereas all other elements of M^{p} are zero. This leads to $f^{\mathrm{p}}_{\mathrm{L}} = -\alpha_{\mathrm{s}}\overline{u} - \alpha_{\mathrm{m}}\ddot{\overline{u}}$ and $f^{\mathrm{p}}_{\mathrm{R}} = \alpha_{\mathrm{s}}\overline{u} + \alpha_{\mathrm{m}}\ddot{\overline{u}}$, but all other elements of f^{p} are equal to zero.

Appendix B

Numerical and physical parameters

The analysis of $N_{\mathbf{uc}}$

Table B.1 Geometric and material properties for the analysis of N_{uc} on the macro- and micro-scale

		Symbol	Value	Unit
Macro Scale	Length	L	1	m
	Wave Speed	c_{M}	0.9959	m/s
	Applied Force	F	10	N
	Element Size	h_{M}	0.25	m
	No of element	Nel_{M}	4	
	Critical time step	Δt_{crit}	0.2510	s
	Wave duration	t_{M}^{λ}	1.0042	s
	Time step	Δt_{M}	1	s
	No of time steps	nt_{M}	10	
	Simulation Time	t_{M}^{f}	5	s
Micro Scale	Length	L_{m}	varies	m
	No of element in N_{uc}	nel_{m}	2	
	No of unit cell	N_{uc}	varies	
	Element size	h_{m}	0.0625	m
	Impedance factor	z_{m}	1.2	
	Critical time step	$\Delta t_{\mathrm{m}}^{\mathrm{crit}}$	0.0625	s
	Wave duration	t_{m}^{λ}	0.5	s
	Time step	Δt_{m}	1×10^{-3}	s
	No of wave propagation	N_{wp}	4	
	No of Time Steps	Nt_{m}	2000	
	Simulation Time	$t_{\mathrm{m}}^{\mathrm{f}}$	2	s

The analysis of $N_{\mathbf{wp}}$

Table B.2 Geometric and material properties for the analysis of N_{wp} on the macro- and micro-scale

		Symbol	Value	Unit
Macro Scale	Length	L	1	m
	Wave Speed	c_{M}	0.9959	m/s
	Applied Force	F	10	N
	Element Size	h_{M}	0.25	m
	No of element	Nel_{M}	4	
	Critical time step	Δt_{crit}	0.2510	s
	Wave duration	t_{M}^{λ}	1.0042	s
	Time step	Δt_{M}	1	s
	No of time steps	Nt_{M}	5	
	Simulation Time	$t_{\mathrm{M}}^{\mathrm{f}}$	2.5	s
Micro Scale	Length	L_{m}	1	m
	No of element in N_{uc}	nel_{m}	2	
	No of unit cell	N_{uc}	4	
	Element size	h_{m}	0.0625	m
	Impedance factor	z_{m}	1.2	
	Critical time step	Δt_{crit}	0.0625	s
	Wave duration	t_{m}^{λ}	1	s
	Time step	Δt_{m}	1×10^{-3}	s
	No of Time Steps	Nt_{m}	1000	
	No of wave propagation	N_{wp}	varies	
	Simulation Time	$t_{\mathrm{m}}^{\mathrm{f}}$	varies	s

The displacement curves in gradient elasticity analyses

Table B.3 Geometric and material properties for the gradient analyses

		Symbol	Value	Unit
Homogeneous	Length	L	300	m
	No of element	Nel	6000	
	Young's modulus	E	1.82,1.98,1.99	N/m
	Mass density	ρ	5.5,50.5,500.5	kg/m
	Applied force	F	unit pulse	N
	Time step	Δt	5×10^{-2}	s
	Simulation time	T	280	s
Heterogeneous	Length	L	300	m
	No of element	Nel	6000	
	Length of unit cell	ℓ	1	m
	Young's modulus	E	1	N/m
	Mass density	ρ	1	kg/m
	Impedance factor	z	10,100,1000	
	Volume fraction	α	0.5	
	Applied force	F	unit pulse	N
	Time step	Δt	5×10^{-2}	s
	Simulation time	T	280	s
Gradient	Length	L	300	m
	No of element	Nel	1500	
	Young's modulus	E	1.82,1.98,1.99	N/m
	Mass density	ρ	5.5,50.5,500.5	kg/m
	Applied force	F	unit pulse	N
	Time step	Δt	2×10^{-1}	s
	Simulation Time	T	280	s

Appendix C

Convergence of numerical analyses

The effect of periodic boundary conditions

This section investigates the influence of Dirichlet conditions and periodic boundary conditions, which are imposed on the microstructure, on accurately estimating the macroscopic material properties. Dirichlet conditions via the direct imposition method reduce the size of system equations, which correspond to the degrees of freedom at the boundary, to impose constraints. On the other hand, periodic boundary conditions via the bipenalty method impose a tying between degrees of freedom.

When Dirichlet conditions are employed to the system of equations obtained by Eq. (3.10), an anomaly occurs for the intermediate level of impedance contrast $z_1/z_2 = 100$, number of unit cells $N_{\mathrm{uc}} = 2^2$ and number of wave propagations $N_{\mathrm{wp}} = 2^4$. In Figures C.1a and C.1b, both the averaged momentum and averaged velocity happen to attain values very close to zero at time around t =70 s and 140 s. Using Eq. (3.16) to find the macroscopic mass density results in anomalies in accordance with the zero values of averaged momentum and averaged velocity at the times, as shown in Figure C.1c. On the other hand, periodic boundary conditions are imposed with displacement and velocity constraints with large stiffness and mass penalty parameters chosen as $\alpha_{\mathrm{s}} = 10^3$ and $\alpha_{\mathrm{m}} = 10^6$, respectively. Periodic boundary conditions via the bipenalty method provide better convergence than Dirichlet conditions via the direct imposition method as demonstrated in Figure C.1d.

The convergence of $\ell_{\mathbf{d}}/\ell_{\mathbf{s}}$

In order to compare the ratio between the dynamic length scale parameter ℓ_{d} and the static length scale parameter ℓ_{s} with the one obtained by other gradient models, the $\ell_{\mathrm{d}}/\ell_{\mathrm{s}}$ ratio is iteratively refined over time. For a given problem whose geometric and material properties outlined in Table B, the $\ell_{\mathrm{d}}/\ell_{\mathrm{s}}$ ratio is selected by analysing the displacement curves at the mid-point of the bar, where all impedance contrasts in material relatively converge.

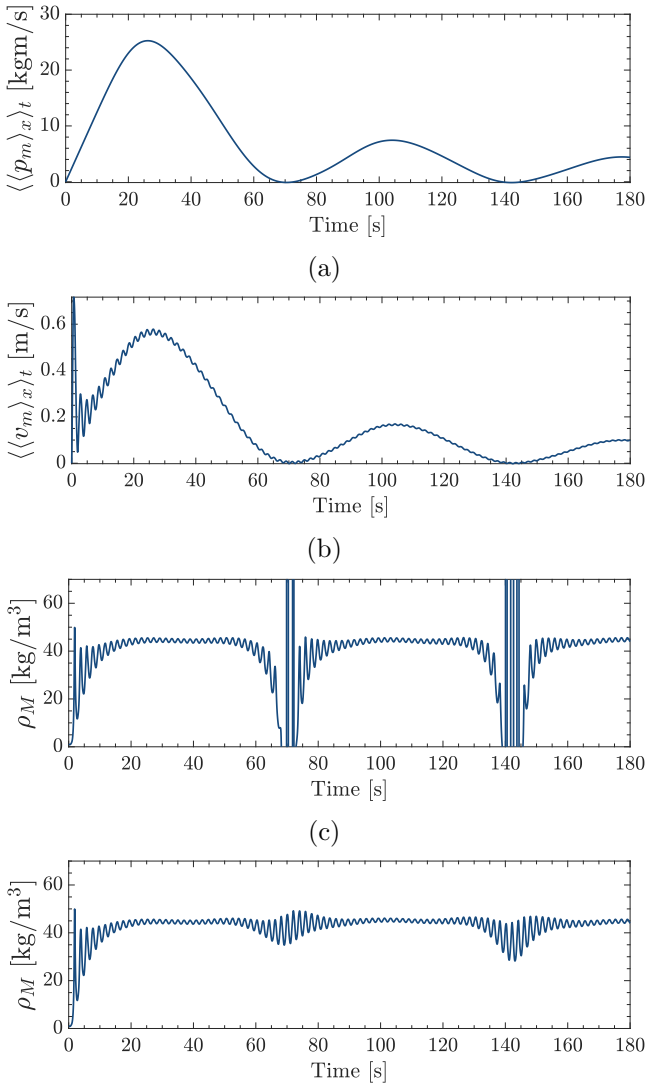

Fig. C.1 Space-time averaging results of the bar presented in Figure 3.2 over microscopic time: (a) averaged momentum, (b) averaged velocity, (c) averaged mass density with Dirichlet conditions, (d) averaged mass density with periodic boundary conditions.

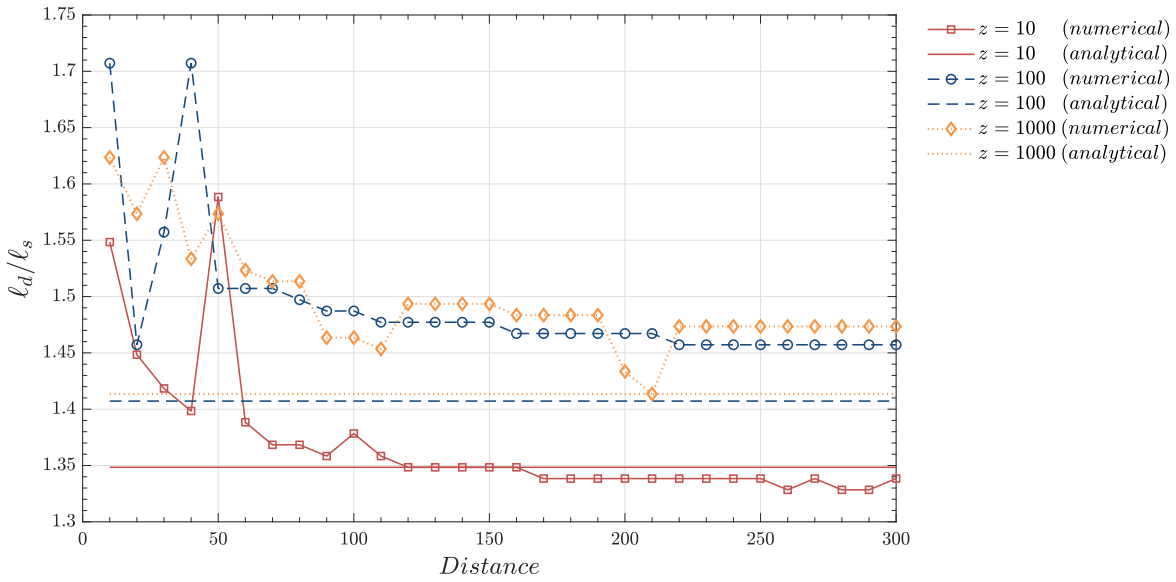

Fig. C.2 The ratio $\ell_\mathrm{d}/\ell_\mathrm{s}$ versus the length of the periodic laminate bar depicted in Figure 5.2 for low contrast $z_1/z_2 = 10$, intermediate contrast $z_1/z_2 = 100$ and high contrast $z_1/z_2 = 1000$, simulated by gradient model with ℓ_d derived analytically [2] and gradient model with the improved ℓ_d presented in Figure 5.4.

Appendix D

Relation between the RVE size and the static length scale

The first-order homogenisation method achieves micro-macro averaging over the RVE within a standard local continuum mechanics framework. In cases where classical continuum mechanics loses accuracy due to size effects, Kouznetsova *et al.* [51] have introduced the second-order homogenisation method to include gradients into the constitutive equations to reflect the underlying material microstructure. The procedure of micro-macro averaging relations within both first-order and second-order homogenisation frameworks is explained to provide a formulation of the RVE as the microstructural length scale. Moreover, the second-order homogenisation method includes the second-order terms in addition to the first-order terms in the Taylor expansion. When Eq. (5.3) is rewritten for the microscopic stiffness and strain as follows

$$E_{\mathrm{m}} = E_{\mathrm{M}} + \Delta x_o \frac{\partial E_{\mathrm{M}}}{\partial x_{\mathrm{o}}} \tag{D.1}$$

$$\varepsilon_{\mathrm{m}} = \varepsilon_{\mathrm{M}} + \Delta x_p \frac{\partial \varepsilon_{\mathrm{M}}}{\partial x_p} \tag{D.2}$$

Now Eq. (D.1) and Eq. (D.2) are embedded into the constitutive relation Eq. (3.4)

$$\sigma_{\mathrm{M}} = \frac{1}{V_{\mathrm{RVE}}} \int\limits_{V_{\mathrm{RVE}}} \left(E_{\mathrm{M}} + \Delta x_o \frac{\partial E_{\mathrm{M}}}{\partial x_o} \right) \left(\varepsilon_{\mathrm{M}} + \Delta x_p \frac{\partial \varepsilon_{\mathrm{M}}}{\partial x_p} \right) \mathrm{d}V \tag{D.3}$$

E_{M} and ε_{M} can be taken out of the integral since these values are at the center of the RVE and thus,

$$\begin{aligned}\sigma_{\mathrm{M}} = E_{\mathrm{M}}\varepsilon_{\mathrm{M}} + \frac{E_{\mathrm{M}}}{V_{\mathrm{RVE}}} \int\limits_{V_{\mathrm{RVE}}} \Delta x_p \, \frac{\partial \varepsilon_{\mathrm{M}}}{\partial x_p} \, \mathrm{d}V + \frac{\varepsilon_{\mathrm{M}}}{V_{\mathrm{RVE}}} \int\limits_{V_{\mathrm{RVE}}} \Delta x_o \, \frac{\partial E_{\mathrm{M}}}{\partial x_o} \, \mathrm{d}V \\ + \frac{1}{V_{\mathrm{RVE}}} \int\limits_{V_{\mathrm{RVE}}} \Delta x_o \, \frac{\partial E_{\mathrm{M}}}{\partial x_o} \Delta x_p \, \frac{\partial \varepsilon_{\mathrm{M}}}{\partial x_p} \, \mathrm{d}V\end{aligned} \tag{D.4}$$

The three remaining integrals in Eq. (D.4) are further detailed using integration by parts. Since Δx_p and Δx_o are scalar, so their derivatives are cancelled out as follows

$$\begin{aligned}\sigma_{\mathrm{M}} = & E_{\mathrm{M}}\varepsilon_{\mathrm{M}} + \frac{E_{\mathrm{M}}}{V_{\mathrm{RVE}}} \int\limits_{\Gamma_{\mathrm{RVE}}} \Delta x_p \, \varepsilon_{\mathrm{M}} \, \mathrm{d}\Gamma + \frac{\varepsilon_{\mathrm{M}}}{V_{\mathrm{RVE}}} \int\limits_{\Gamma_{\mathrm{RVE}}} \Delta x_o \, E_{\mathrm{M}} \, \mathrm{d}\Gamma + \\ & \frac{E_{\mathrm{M}}}{V_{\mathrm{RVE}}} \int\limits_{\Gamma_{\mathrm{RVE}}} \Delta x_o \, \Delta x_p \, \frac{\partial \varepsilon_{\mathrm{M}}}{\partial x_p} \, \mathrm{d}\Gamma - E_{\mathrm{M}} \frac{\partial^2 \varepsilon_{\mathrm{M}}}{\partial x_o \partial x_p} \int\limits_{V_{\mathrm{RVE}}} \Delta x_o \, \Delta x_p \, \mathrm{d}V\end{aligned} \tag{D.5}$$

Under the assumption of periodic boundary conditions, the boundary integrals vanish due to the integration over a symmetric domain and the final term in Eq. (D.5)

$$\int\limits_{V_{\mathrm{RVE}}} \Delta x_o \, \Delta x_p \, \mathrm{d}V = \int\limits_{\frac{-L}{2}}^{\frac{L}{2}} \int\limits_{\frac{-L}{2}}^{\frac{L}{2}} \int\limits_{\frac{-L}{2}}^{\frac{L}{2}} \Delta x_o \, \Delta x_p \, \mathrm{d}x\mathrm{d}x\mathrm{d}x = \frac{1}{12} L_{\mathrm{RVE}}^5 \Delta_{op} \tag{D.6}$$

where Δ_{op} is the Kronecker delta, and $V_{\mathrm{RVE}} = L_{\mathrm{RVE}}^3$ where L_{RVE} is the size of the RVE. With the elaborations, Eq. (D.3) becomes

$$\sigma_{\mathrm{M}} = E_{\mathrm{M}} \left(\varepsilon_{\mathrm{M}} - \frac{1}{12} L_{\mathrm{RVE}}^2 \, \frac{\partial^2 \varepsilon_{\mathrm{M}}}{\partial x_o \partial x_p} \right) \tag{D.7}$$

When comparing the constitutive equations in the gradient elasticity and second-order homogenisation frameworks, Eq. (2.9) bears a noticeable resemblance to Eq. (D.7). Consequently, their dependencies ℓ_{s} and L_{RVE}, respectively, can be connected by considering a coefficient that precedes the L_{RVE} [31].